Osmotic Reflection Coefficient

by

Gaurav Bhalla

B. Tech., Chemical Engineering
Indian Institute of Technology- Delhi, 1999

Submitted to the Department of Chemical Engineering
in partial fulfillment of the requirements for the degree of

DOCTOR OF PHILOSOPHY IN CHEMICAL ENGINEERING

at the

MASSACHUSETTS INSTITUE OF TECHNOLOGY

[JUNE]
May 2009

ARCHIVES

Signature of Author: _____

Department of Chemical Engineering
May, 2009

Certified by: _____

William M. Deen
Professor of Chemical Engineering
Thesis Supervisor

Accepted by: _____

William M. Deen
Professor of Chemical Engineering
Chairman, Committee for Graduate Students

Osmotic Reflection Coefficient
by
Gaurav Bhalla

Submitted to the department of Chemical Engineering on May, 2009
in partial fulfillment of the requirements for the degree of
Doctor of Philosophy in Chemical Engineering

ABSTRACT

The presence of a discriminating barrier separating two solutions differing in concentration generates a net volume flux called osmotic flow. The simple case is of the ideal semi-permeable membrane which completely excludes the solute. The flow through such a membrane is directly proportional to the thermodynamic pressure drop less the osmotic pressure drop. For membranes which partially exclude the solute the osmotic contribution to flow is less than that of the semi-permeable membrane, and the reduction is given by the osmotic reflection coefficient σ_o. This work was motivated by understanding the mechanistic aspects of osmotic flow through such membranes, in order to predict σ_o. One of the main goals of the research was to develop computational models to predict σ_o for charged porous membranes and charged fibrous membranes.

The effects of molecular shape on σ_o for rigid macromolecules in porous membranes were analyzed using a hydrodynamic model. In this type of model, employed first by Anderson and Malone, steric exclusion of the solute from the periphery of the pore induces a concentration-dependent drop in pressure near the pore wall, which in turn causes the osmotic flow (Anderson and Malone 1974). Results were obtained for prolate spheroids (axial ratio, $\gamma > 1$) and oblate spheroids ($\gamma < 1$) in cylindrical and slit pores. Two methods, one of which is novel, were used to compute the transverse pressure variation. Although conceptually different, they yielded very similar results; the merits of each are discussed. For a given value of a/R, where a is the prolate minor semiaxis or oblate major semiaxis and R is the pore radius, σ_o increased monotonically with increasing γ. When expressed as a function of a_{SE}/R, where a_{SE} is the Stokes-Einstein radius, the effects of molecular shape were less pronounced, but still significant. The trends for slits were qualitatively similar to those for cylindrical pores. When σ_o was plotted as a function of the equilibrium partition coefficient, the results for all axial ratios fell on a single curve for a given pore shape, although the curve for cylindrical pores differed from that for slits. For spheres ($\gamma = 1$) in either pore shape, σ_o was found to be only slightly smaller than the reflection coefficient for filtration (σ_f). That suggests that σ_o can be used to estimate σ_f for spheroids, where results are currently lacking.

A computational model was developed to predict the effects of solute and pore charge on σ_o of spherical macromolecules in cylindrical pores. Results were obtained for particles and pores of like charge and fixed surface charge densities, using a theory that combined low Reynolds number hydrodynamics with a continuum, point-charge description of the electrical double layers. In this formulation steric and/or electrostatic exclusion of macromolecules from the vicinity of the pore wall creates radial variations in osmotic pressure. These, in turn, lead to the axial pressure gradient that drives the osmotic flow. Due to the stronger exclusion that results from repulsive electrostatic interactions, σ_o with charge effects always exceeded that for an uncharged system with the same solute and pore size. The effects of charge stemmed almost entirely from particle positions within a pore being energetically unfavorable. It was found that the required potential energy could be computed with sufficient accuracy using the linearized Poisson-Boltzmann equation, high charge densities notwithstanding. In principle, another factor that might influence σ_o in charged pores is the electrical body force due to the streaming potential. However, the streaming potential was shown to have little effect on σ_o, even when it markedly reduced the apparent hydraulic permeability.

A model based on continuum hydrodynamics and electrostatics was developed to predict the combined effects of molecular charge and size on the σ_o of a macromolecule in a fibrous membrane, such as a biological hydrogel. The macromolecule was represented as a sphere with a constant surface charge density, and the membrane was assumed to consist of an array of parallel fibers of like charge, also with a constant surface charge density. The flow was assumed to be parallel to the fiber axes. The effects of charge were incorporated into the model by computing the electrostatic free energy for a sphere interacting with an array of fibers. It was shown that this energy could be approximated using a pairwise additivity assumption. Results for σ_o were obtained for two types of negatively charged fibers, one with properties like those of glycosaminoglycan chains, and the other for thicker fibers having a range of charge densities. Using physiologically reasonable fiber spacings and charge densities, σ_o for BSA in either type of fiber array was shown to be much larger than (often double) that for an uncharged system. Given the close correspondence between σ_o and the σ_f, the results suggest that the negative charge of structures such as the endothelial surface glycocalyx is important in minimizing albumin loss from the circulation.

Thesis Supervisor: William M. Deen
Title: Carbon P. Dubbs Professor of Chemical Engineering

ACKNOWLEDGEMENTS

MIT was a fabulous place; it truly was "drinking from a hose pipe" as they say. I had the opportunity to meet some really remarkable people. Many of them helped me evolve as a person and were instrumental in helping me reach this milestone.

First and foremost, I am grateful to my advisor Professor William M. Deen. His scientific insight was invaluable, I am more thankful to him for his understanding and the amount of freedom he gave me to pursue interests apart from research. I would like to thank the group for their friendly support : Kristin Mattern, Panadda Dechadilok, Brian Skinn, Melanie Chin, Chang Hoon Lim and Ian Zacharia. They all played a role in making 66-463 a great place to work. I would also like to thank my committee, Professor T.A Hatton and Professor P.S. Doyle for their insightful comments over the course of the work.

I have been fortunate enough to have made some close friends during my stay at MIT. I would especially like to thank Madhusudhan Nikku, a PhD candidate in the Physics department at MIT, for his selfless help and support. The "Goofy group at Ashdown": Amy Tang, Sohan Dharmaraja and Siddarth Kumar made my stay here a fun filled one.

Last but certainly not the least, I would not have been able to achieve this goal without the unconditional love and support of my parents back in India. My Dad taught me the true meaning of persistence, my Mom taught me the true meaning of integrity. I owe everything to them. Thanks Mom and Dad!

Table of Contents

List of Figures

LIST OF FIGURES

List of Tables

Chapter 1. BACKGROUND

When liquid solutions of differing concentration are separated by a solvent-permeable membrane, there tends to be osmotic flow toward the more concentrated solution. The magnitude of the flow depends in part on how "tight" or "leaky" the membrane is to the solute(s). The relevant measure of tightness or leakiness is the osmotic reflection coefficient (σ_o), introduced by Staverman (Staverman 1951). For a binary solution, the relationship between the volume flux (J_V), hydraulic permeability (L_P), actual pressure difference (ΔP), and osmotic pressure difference ($\Delta \Pi$) is

$$J_V = L_P\left(\Delta P - \sigma_o \Delta \Pi\right) \tag{1.1}$$

If $J_V > 0$ for flow from left to right, then ΔP and $\Delta \Pi$ are the respective pressures in the left-hand solution minus those on the right. For an ideal semipermeable membrane (no solute passage), $\sigma_o = 1$ and the osmotic flow for a given L_P and $\Delta \Pi$ is maximized. Equation (1.1) with $\sigma_o = 1$ was used by Starling in his pioneering analysis of microvascular fluid exchange, the solute being total plasma protein (Starling 1896). At

the other extreme is an unselective membrane (no discrimination between solute and solvent), where $\sigma_0 = 0$ and there is no osmosis, only pressure-driven flow. In general, one expects intermediate behavior, such that $0 < \sigma_0 < 1$. Values of σ_0 for various solutes have been measured for cell membranes (Hill 1995, Goldstein and Solomon 1960), capillary walls (Curry et al. 1976, Michel 1980), and synthetic membranes (Opong and Zydney 1992, Friedman and Meyer 1981, Schultz et al. 1979) to cite a few examples.

From a thermodynamic viewpoint, osmosis is due to an imbalance in the chemical potential of the solvent. The presence of any solute dilutes the solvent, thereby lowering its chemical potential. Thus, in the absence of a pressure difference, solvent tends to move toward the compartment with the higher solute concentration (lower solvent chemical potential). However, an increase in pressure can compensate for solvent dilution, the pressure increase being expressed by Π. Although sometimes confused with an actual pressure, $\Delta\Pi$ is just the concentration-dependent part of the difference in solvent chemical potential, expressed as an equivalent pressure. For an ideal semipermeable membrane, it equals the transmembrane pressure that would result in equilibrium (i.e., $\Delta P = \Delta\Pi$ for $J_V = 0$ if $\sigma_o = 1$). For a dilute, ideal solution, van't Hoff's law gives $\Pi = kTC$, where k is Boltzmann's constant and C is solute concentration expressed as number of molecules per unit volume.

1.1. Experimental determination of the osmotic reflection coefficient

The ideas of osmotic flow and osmotic equilibrium date back to Starling (Starling 1896). By conducting infusion experiments on dog hind limbs, Starling was able to arrive at the conflicting nature of the hydrostatic and osmotic pressure forces across capillaries as described by the equation (1.1) above. Michel gives a review of these experiments (Michel 1984).

Vargas and Johnson developed the osmotic weight transient method to estimate the osmotic reflection coefficients for solutes inside rabbit heart capillaries (Vargas and Johnson 1964). The starting point for their analysis was the equation (1.2) relating the flux to the pressure drop. The equation can be modified for the case when multiple solutes are present in the system as (Kedem and Katchalsky 1961)

$$J_V = L_p[\Delta P - RT\sum_i \sigma \Delta C_i] \tag{1.2}$$

The basic idea is then to introduce a test solute inside the system while all other concentrations and pressures are held steady and measure the rate of water loss through the organ which would in turn be a direct estimate of the osmotic reflection coefficient for that solute. To ensure that the measurement is made at invariant hydrostatic pressure the measurement is made just after introducing the test solute in the system. This can take care of unwanted changes in the hydrostatic pressure due to the introduction of the test solute.

Measurements of the solute osmotic reflection coefficients for solutes in skeletal and cardiac muscles have been made by many investigators. Due the differences in the experimental set up used in these investigations a direct comparison among the results is difficult but some trends can be discerned. The reflection coefficient increases as a

function of solute size and approaches 1.0 for large solutes like Albumin. The reflection coefficient is non zero even for very small solutes like NaCl. The results are summarized in Figure 1.1 (Kellen 1999).

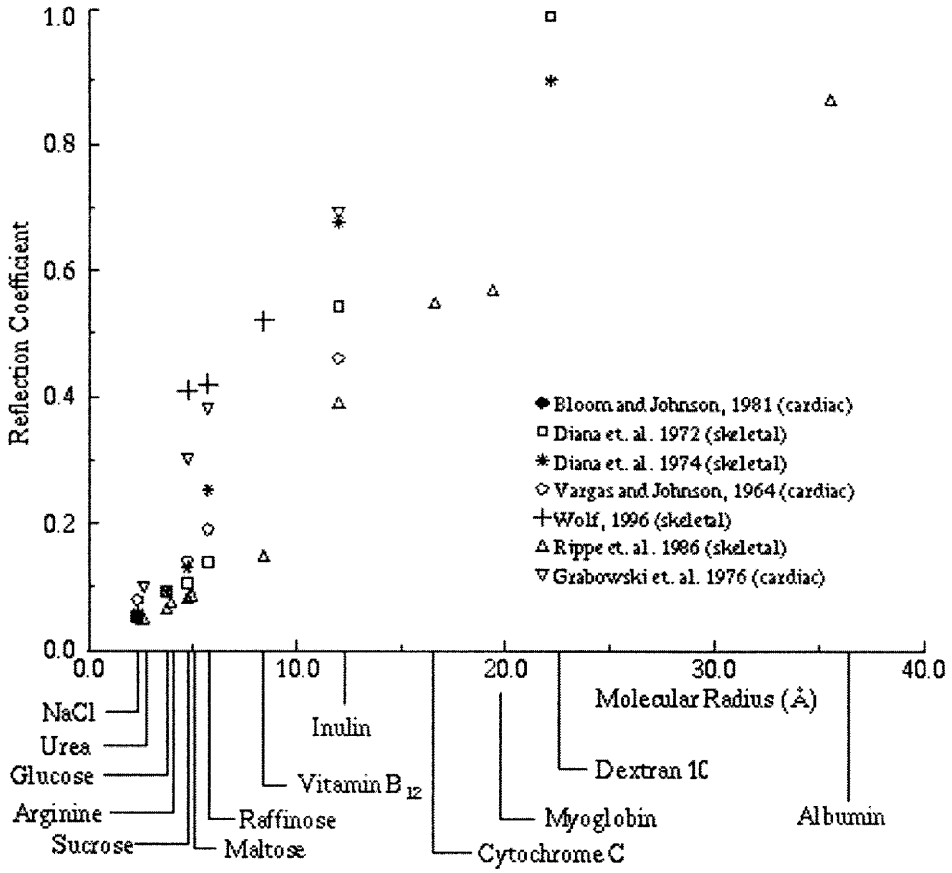

Figure 1.1 Summary of the experimental osmotic reflection coefficients made by some authors (Kellen 1999).

Curry and Michel have made osmotic reflection coefficient measurements for urea, NaCl, sucrose and cyanocobalamin in frog mesenteric capillaries (Curry and Michel 1984). The results are plotted as a function of the solute radius. Furthermore, the authors extrapolate the results for the implied value of the osmotic reflection coefficient for a

solute of the size of water. This value is given to be 0.08 which suggests that there are channels in capillary walls which are available exclusively to water

Experimental studies and data on osmotic reflection coefficient for macromolecular solutes in synthetic membranes are limited. Schultz et al have measured osmotic reflection coefficients for bovine serum albumin (BSA), bovine immunoglobulin (IgG) and dextrans in track-etched nucleopore membranes (Schultz et al. 1979). The measurement of osmotic reflection coefficient for the solutes was effected by the equation (1.2) above written as

$$J_V = L_p[\Delta P - \sigma_0 \Delta \Pi] = L_p[(P_1 - P_2) - \sigma_0(\Pi_1 - \Pi_2)] \tag{1.3}$$

The subscripts refer to the external solutions on the adjacent sides of the membrane. The flow rate was plotted against the applied hydrostatic head and in accordance with the equation above, the osmotic reflection coefficient was given by

$$\sigma_0 = \left(\frac{\Delta P}{\Delta \Pi}\right)_{J_V=0} \tag{1.4}$$

The pressure drop ΔP was read off as an intercept on the pressure axis at zero flow, whereas $\Delta \Pi$ was obtained from the bulk solutions concentrations across the membrane. The flow measurements were made at steady state.

Schultz et al observed a reduced membrane hydraulic permeability in the presence of the solute, which was attributed to solute adsorption within the porous matrix (Schultz et al. 1979). Osmotic reflection coefficient data has been plotted against the non-dimensional radius of the solute. An increasing trend can be discerned, despite the scatter in the data.

Osmotic reflection coefficient measurements for BSA in polyethersulfone membranes have been performed by Zydney et al. in 1992 (Zydney et al. 1992). The apparatus used was similar to that of Schultz et al. The diffusional cell consisted of two plexiglass chambers with the membrane mounted at the interface. An impeller fixed a small distance away from the membrane was used to stir the solutions. The hydrostatic head was controlled by means of a feed reservoir connected to the upstream side as in the earlier apparatus. The osmotic reflection coefficient was given by equation (1.4) above. The pressure drop at zero flux was determined from a linear fit between the flux and the applied hydrostatic head. The authors investigated concentration effects by measuring the reflection coefficient at varying solute concentrations. The resulting osmotic reflection coefficient data was shown to have much greater concentration dependence than the theory proposed by Anderson and Adamski in 1983 (Anderson and Adamski 1983). This was attributed to the ellipsoidal shape of the solute molecules and/or the presence of long range forces. The osmotic reflection coefficient data when extrapolated to zero concentration gave the infinite dilution osmotic reflection coefficient. These values were then plotted against the non-dimensional solute radius in order to compare with the theoretical predictions given by Anderson and Malone 1974 (Anderson and Malone 1974).

1.2 Osmotic reflection coefficient – The non-equilibrium thermodynamic approach

The non-equilibrium thermodynamic approach proposed by Kedem and Katchalsky in 1958 was a theoretical formulation of osmotic flow through porous

membranes (Kedem and Katchalsky 1958). The approach had its merit in that force-flux relationships were written in terms of macroscopic differences in the species chemical potentials. There was not given any explicit consideration to point-wise potential gradients in the membrane. Onsager's reciprocity was in-built in the formulation in that the matrix of phenomenological coefficients was assumed to be symmetric (Onsager 1931). The following is a brief outline of the prominent ideas.

The fluxes were written in terms of the trans-membrane potential differences

$$\begin{aligned} J_s &= L_{ss}\Delta\mu_s + L_{sw}\Delta\mu_w \\ J_w &= L_{ws}\Delta\mu_s + L_{ww}\Delta\mu_w \\ L_{sw} &= L_{ws} \end{aligned} \tag{1.5}$$

The L's are the proportionality coefficients and the subscripts *s* and *w* refer to solute and the solvent. The trans-membrane differences in chemical potential were expressed in terms of the hydrostatic and osmotic pressure drops across the membrane as

$$\begin{aligned} \Delta\mu_w &= \overline{V_w}(\Delta P - \Delta\Pi) \\ \Delta\mu_s &= \overline{V_s}\Delta P + RT\Delta \ln X_s \end{aligned} \tag{1.6}$$

where $\overline{V_w}$ and $\overline{V_s}$ refer to the partial molar volume and X is the mole fraction.

These were substituted in the flux expressions and a volumetric flux was defined as

$$J_V = L_P\Delta P + L_{PD}\Delta\Pi \tag{1.7}$$

where

$$J_V = J_w\overline{V_w} + J_s\overline{V_s} \tag{1.8}$$

J_w and J_s refer to the solvent and the solute fluxes. The above equation was then written in the form of equation (1.1) above and osmotic reflection coefficient was given by

$$\sigma_0 = -L_{PD} / L_P \tag{1.9}$$

The fact that the approach does not take into account point-wise potential gradients limits its scope and applicability in that it would fail to describe these microscopic mechanistic aspects. Another limitation stems from the fact that the phenomenological coefficients as defined in equation (1.5) above are in general concentration dependent. This then introduces a practical problem in their determination just by means of a single experimental run for a particular set of conditions. There is therefore a need to develop models wherein the mechanistic significance of the phenomenological coefficients can be realized. The frictional models which were a step in this direction are described next. Within such a framework, the non-equilibrium thermodynamic approach can be a useful guide for expressing interrelationships among the mechanistic coefficients on the basis of the theorem of reciprocity (Ogston and Michel 1978).

1.3 Osmotic reflection coefficient – frictional models

The idea that the diffusional, convective and electrostatic forces acting on the solutes were balanced in equilibrium with the frictional forces was proposed first by Spiegler (Spiegler 1958). Perl formulated the osmotic flow through porous membranes using ideas very similar to those proposed by Spiegler (Perl 1973). The drag force on the solute and the solvent (written here as s and w respectively) represented as the negative

gradient of the respective chemical potential was balanced by the hydrodynamic friction forces as

$$\begin{aligned} -\overline{V}_s \frac{dp}{dx} - RT \frac{d \ln X_s}{dx} &= f_{sw}(C)(v_s - v_w) + f_{sm}(C)v_s \\ -\overline{V}_w \frac{dp}{dx} - RT \frac{d \ln X_w}{dx} &= f_{ws}(C)(v_w - v_s) + f_{wm}(C)v_w \end{aligned} \tag{1.10}$$

with the *f's* representing the frictional interactions between the solute, solvent and the membrane pore wall. Here *v* refers to the velocity and the subscript *m* denotes the membrane.

The elimination of concentration gradients by means of adding the equations gave for the pressure gradient

$$-\frac{dp}{dx} = f_{sm}(C)J_s + f_{wm}(C)J_w \tag{1.11}$$

This equation on substitution gives for the concentration gradient for the solute (on assuming a dilute solution inside the pore

$$-RT\frac{dC}{dx} = -[f_{sw}(C) + f_{sm}(C)]J_s + [f_{sw}(C) + \frac{\overline{V}_s}{\overline{V}_w} f_{wm}(C)]CJ_v \tag{1.12}$$

The filtration reflection coefficient was then defined by

$$1 - \sigma_f = [J_s / C_1 J_v]_{C_1 = C_2} \tag{1.13}$$

where C_1 and C_2 refer to the concentrations that prevail in the bathing liquids. These concentrations were related to the concentrations inside the pore by means of partition coefficient Φ.

This gave for the filtration reflection coefficient

$$1-\sigma_f=\Phi\frac{f_{sw}+\frac{\overline{V_s}}{\overline{V_w}}f_{wm}}{f_{sw}+f_{sm}} \tag{1.14}$$

also for the osmotic reflection coefficient we have

$$1-\sigma_0=\frac{1}{RT}[(P_1-P_2)/(C_1-C_2)]_{J_v=0} \tag{1.15}$$

where p_0 and p_1 are the pressures that prevail in the bathing liquids. Using the above formulation one obtains for the osmotic reflection coefficient

$$1-\sigma_0=\Phi\frac{f_{sw}+\frac{\overline{V_s}}{\overline{V_w}}f_{wm}}{f_{sw}+f_{sm}} \tag{1.16}$$

which is equal to the solvent drag reflection coefficient. These results were also obtained by Dainty and Ginzburg in 1963 (Dainty and Ginzburg 1963). A similar formulation of the frictional model is also given by Lightfoot et al . in 1976 (Lightfoot et al. 1976).

The frictional models gave a mechanistic significance to the non-equilibrium thermodynamic approach presented above. The point-wise force description is an added improvement over the former. The equality of solvent drag reflection coefficient and the osmotic reflection coefficient lends consistency to the approach given the assumption of Onsager's reciprocity (Onsager 1931). The frictional coefficients are in general functions of concentration which in turn depends on the axial and the radial coordinate. However, they are treated to be constants in the integration of the flux-force relationships which is a practical limitation of the approach.

Bean and Curry have obtained expressions for the osmotic reflection coefficient using general friction model framework (Bean 1972, Curry 1974). The Brenner and

Happel result is used to describe the force acting on a spherical solute molecule translating in a cylinder (Brenner and Happel 1973). This is given by

$$F_{drag} = \frac{6\pi\mu a}{F(\lambda,r)}[v_S - v_{w,\max} G(\lambda,r)] \tag{1.17}$$

where v_s refers to the solute velocity and $v_{w,max}$ refers to the maximum solvent velocity and λ is the dimensionless solute radius. The gradient of the solute chemical potential can then be equated to this drag force. Bean neglects the radial variation the lag coefficient G in the formulation whereas Curry uses a modified form of the lag coefficient G taking into account radial variations (Bean 1972, Curry 1974). The approach seems to be the first within the general friction model framework wherein the variation of the lag coefficient is taken into account. The radial variations in F are disregarded and the centerline value is taken as a constant in the development. The expression for the osmotic reflection coefficient is given by

$$1-\sigma_0 = \frac{16\lambda^2}{9}(1-\lambda)^2 F(\lambda,0) + (1-\lambda)^2(1+2\lambda-\frac{7}{5}\lambda^2) \tag{1.18}$$

1.4 Mechanics of osmotic flow through capillary pores

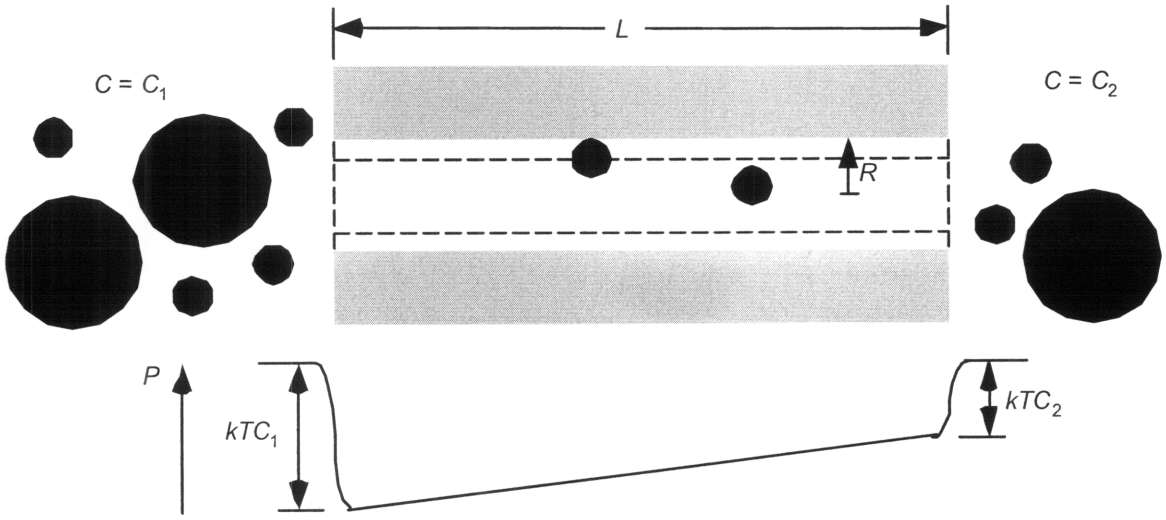

Figure 1.2 Exclusion of spherical solutes from a pore of radius R and length L. Large and small molecules are shown, the external concentration of either being C_1 on the left and C_2 on the right. The centers of the large molecules must remain outside the surfaces denoted approximately by the vertical dashed lines. If only large molecules were present, the axial pressure profile inside the pore, for equal external pressures and $C_1 > C_2$, would be as shown at the bottom. The smaller molecules can enter the pore, but their centers cannot get closer to the pore wall than the surface indicated by horizontal dashed lines. The result then is a combination of axial and radial pressure variations (not shown).

The mechanical view of Osmotic flow was first given by Mauro and Ray (Mauro 1957, Ray 1960). By invoking viscous flow in semi-permeable pores, the equivalence between hydraulic and osmotic flows was explained. This is described now in the context of spherical solutes of radius a and membranes with cylindrical pores of radius R and length L. For ideal semipermeable membranes, osmotic near-equilibria will exist locally

at each end of a long pore. Because in this case the spherical solutes are large enough to be fully excluded ($a > R$), the pore ends act as ideal barriers. Applying the equillibrium condition of $\Delta P = \Delta \Pi$ or (equivalently) $P - \Pi =$ constant, the drop in solute concentration upon entering a pore requires a fall in pressure, the larger the external concentration, the larger the pressure drop. In this way, the external concentration (or osmotic pressure) difference is translated into a mechanical pressure gradient within the pore, which drives a Poiseuille flow. As shown in Figure 1.2, in which the external pressures are assumed to be equal, having a greater solute concentration on the left will create an internal pressure gradient that drives flow from right to left, consistent with the thermodynamic analysis described above.

The special feature of long pores ($L >> R$) is that the flow rate is controlled by the hydrodynamic resistance in the bulk of the pore. With negligible resistances at the pore ends, one can assume a close approach to osmotic equilibrium at the pore entrance and exit. Steric considerations imply that the concentration drop upon entering a pore is complete within a distance of order R, so that for long pores this transition distance can be neglected when computing the internal pressure gradient.

Anderson and Malone extended the idea of local osmotic equilibria to "leaky" pores (Anderson and Malone 1974), which is described next.

1.5 Osmotic flow through "leaky" capillary pores - Anderson approach

The prediction of the osmotic reflection coefficient for membranes composed of "leaky" pores or those that are large enough for the solute to enter requires a better understanding of the flow mechanics in such a system. The presence of the pore wall hinders the solute macromolecule in that it cannot sample all the orientation space as in an unbounded solution. This can also be thought of as a potential field existing between the solute and the pore wall. The force on the solute can be described by the gradient of this potential. The potential could be a short range hard particle - hard wall steric potential, a force potential like the Van der Waals or an electrostatic potential for charged solutes.

Anderson and Malone extended the idea of local osmotic equilibria to "leaky" pores (Anderson and Malone 1974). Whereas spherical solutes with $a < R$ can enter a pore, their centers are still excluded from a region of thickness a next to the pore wall. It was reasoned that this radial concentration decrease (which could be influenced also by long-range solute-wall interactions), would create a radial pressure drop. The radial pressure variation would be proportional to the solute concentration at the pore centerline, which is a function of axial position. Thus, the effect of steric or other solute exclusion by the pore wall would be to create an axial pressure gradient (at least near the wall), resulting in flow. Relating the volume flow rate per pore to the external concentration difference led to predictions for the value of σ_0.

The model begins by considering a long cylindrical pore of radius R and length L with $L/R \rightarrow \infty$. The total transport resistance was assumed to be in the pore itself and a state of thermodynamic equilibrium was assumed between the pore and the bulk fluid at

the pore ends. Further a solute potential field ψ (r) which controls the radial distribution of the solute within the pore was assumed. The solution strategy then was to assume zero solute flux in the radial direction to solve for the solute to solve the concentration problem. The concentration profiles were then used to work out the radial pressure profile. Finally that pressure profile was used to solve lubrication like flow problem and finally compute the osmotic reflection coefficient.

It was assumed in the development of the model that the solvent dimensions are much smaller than the pore radius. This assumption justified the use of the continuum hypothesis and the use of potential energy field that applied only to the solute implying that the solvent pore wall interactions were absent. A constant viscosity was assumed in the derivation which means that the solute volume fraction in the pore must be small. The Anderson and Malone analysis would be now described in more detail (Anderson and Malone 1974).

The Gibbs - Duhem equation was used to relate the pressure and the potential gradient assuming radial mechanical equilibrium as pointed out above.

$$\frac{\partial P}{\partial r} + C\frac{\partial \psi}{\partial r} = 0 \tag{1.19}$$

The solute concentration C as a function of r and z was given by the Boltzmann equation as

$$C(r,z) = C_0(z)\exp(-(\psi - \psi_0)) \tag{1.20}$$

The subscript zero designates the pore centerline, this equation on substitution above gave for the pressure

$$P(r,z) = P_0(z) - \Pi_0(z)[1 - e^{-(\psi - \psi_0)}] \tag{1.21}$$

where $\Pi_0(z)$ is the osmotic pressure $R_g T C_0(z)$.

The Stokes equation then was simplified by employing the lubrication approximation due to the narrowness of the pore.

$$0 = -\frac{\partial P}{\partial z} + \frac{\mu}{r}\frac{\partial}{\partial r} r\left(\frac{\partial u}{\partial r}\right) \tag{1.22}$$

The pressure profile was used to solve the Stokes equation along with the "no-slip" boundary condition to give for the axial velocity profile

$$u = -\frac{(R^2 - r^2)}{4\mu} P_0'(z) + \frac{\Pi_0'(z)}{\mu} \int_r^R \frac{dy}{y} \int_0^y x[1 - e^{-(\psi - \psi_0)}]dx \tag{1.23}$$

The equation was then averaged over the pore cross section to determine the average velocity and hence the flux which was then compared to equation (1.2) to formulate the expression for the osmotic reflection coefficient as

$$\sigma_0 = 1 - \frac{8}{R^4} \int_0^R 2r dr \int_r^R \frac{dy}{y} \int_0^y x \exp(-\psi) dx \tag{1.24}$$

Osmotic reflection coefficients were worked out for spherical molecules of a given radius. The solute pore walls were defined to be infinite potential barriers located one projected length dimension away from the physical boundary. For a spherical molecule of a radius *a* this potential was given by

$$\begin{aligned} \psi(r) &= 0 \quad 0 < r < R - a \\ \psi(r) &\to \infty \quad r > R - a \end{aligned} \tag{1.25}$$

The expression (1.24) is suited to develop an expression for the osmotic reflection coefficient for a continuous potential field. For the special case of a discontinuous steric potential one works by separating the flow problem instead to arrive at

$$\sigma_0 = (1-(1-\lambda)^2)^2 \tag{1.26}$$

where λ is the dimensionless solute radius with the pore radius as the basis.

The case of a spherical molecule in a slit pore is a logical fall out of the above methodology and the osmotic reflection coefficient was found out to be

$$\sigma_0 = \frac{\lambda^2}{2}(3-\lambda) \tag{1.27}$$

Anderson extended these results to study the configurational effect on the reflection coefficient for rigid solutes in capillary pores (Anderson 1981). Analytical results were derived for spherical solutes in pores of rectangular cross section. Further, results were derived for non-spherical solutes in circular pores and in slit pores. The basic methodology remained the same in all these extensions however a few interesting observations were made.

Reed's derivation was used to work out the osmotic reflection coefficients instead of the less amenable equation (1.24) (Reed 1978). Using equations (1.21) and (1.22) Reed derived a simplified expression for the osmotic reflection coefficient that was used for the extensions above. This expression was given by

$$\sigma_0 = 1 - \frac{\left\langle u^* \frac{1}{4\pi} \iint \exp(-\psi) d\mathbf{e} \right\rangle}{\langle u^* \rangle} \tag{1.28}$$

where u^* was the velocity field generated by the solute concentration difference if the solute were completely excluded from the pore, a result relatively easy to obtain and **e** referred to the orientation of the solute.

Hill critically challenges the above methodology. The argument is that thermodynamic equilibrium in the transverse direction would predict zero pressure

gradients, something that would be inconsistent within the above framework (Hill 1989, 1995). However, the argument fails to take into account the augmented chemical potential due to the wall-solute interaction in the pore. Once this is recognized, pressure gradients in the transverse direction can be explained. The analysis did not take into account the effect of the solute concentration on the osmotic reflection coefficient. Anderson and Adamski developed a theory to predict the effect of solute-solute interactions on the osmotic reflection coefficient, though the analysis is not directly relevant to this work (Anderson and Adamski 1983). Further this work was limited to narrow pore geometries where use could be made of the lubrication approximation. Pore entrance and exit effects have also been examined for spherical solutes (Yan at el. 1986).

Another argument has been raised by Levitt who has proved the equivalence of osmotic and filtration (solvent drag) reflection coefficients, something which Anderson's model fails to accomplish (Levitt 1975). The approach seems plausible for the special case of dilute solutions wherein the solute flux can be neglected in comparison to the solvent flux.

1.6 Osmotic reflection coefficient for flow through fibrous membranes

Curry and Michel propose to extend the Anderson and Malone's result of 1974 to predict the osmotic reflection coefficient through network of fibers written in terms of Φ, the solute partition coefficient (Curry and Michel 1980).

$$\sigma_0 = (1-\Phi)^2 \tag{1.29}$$

Zhang et al. develop a mechanistic model to calculate σ_0 for neutral spheres in membranes consisting of regular arrays of neutral fibers along the lines of the Anderson

and Malone model (Zhang et al. 2006). The flow was assumed parallel to the fiber axis, and the geometry was simplified to an annulus by replacing the hexagonal boundary by a circle. The radius of the circle or the "flow radius" R, was chosen to maintain the same open area per fiber. The approach very closely follows the Anderson and Malone model and gives for σ_0

$$\sigma_0 = \frac{\frac{\alpha^2}{4} + \frac{\alpha^3\beta}{2} + \frac{\alpha^4}{8} + \frac{\alpha^2\beta^2}{2} + \frac{\alpha\beta}{2} - \frac{(\alpha+\beta)^2}{2}\ln\left(1+\frac{\alpha}{\beta}\right)}{\frac{3}{8} + \frac{\beta^4}{8} + \frac{1}{2}\ln(\beta) - \frac{\beta^2}{2}} \tag{1.30}$$

where $\alpha = a/R$ and $\beta = b/R$, a and b being the solute and the fiber radius respectively.

1.7 Filtration reflection coefficient and the test for reciprocity

The rates of diffusion or convection in porous and fibrous media tend to be lower than in the bulk solution. This phenomenon called as hindered transport is explained in large part by the combination of steric and hydrodynamic interactions between the permeating molecule and the medium (Deen 1987). The flux of the solute through such a medium is given by

$$N = -K^{-1}D_\infty \frac{\partial C}{\partial z} + GVC \tag{1.31}$$

where D_∞ is the diffusion coefficient in an unbounded fluid and V is the velocity of the unperturbed fluid far upstream and downstream from the particle. The coefficients K and G are the hydrodynamic coefficients that describe hindered diffusion and convection respectively.

Using the form of the concentration field as given by equation (1.20) one can write for the flux averaged over the pore cross section as

$$\langle N \rangle = -K_d D_\infty \frac{d\langle C \rangle}{dz} + K_c \langle V \rangle \langle C \rangle \tag{1.32}$$

where the angle brackets denote the average quantities, and K_d and K_c are averaged hydrodynamic diffusion and convective coefficients. $\langle N \rangle$ and $\langle V \rangle$ also refer to J_s and J_v in Section 1.3. This equation can be integrated for the average flux in terms of concentration that prevail in the adjacent external solutions to give

$$\begin{aligned}
\langle N \rangle &= W \langle V \rangle C_1 \frac{[1-(C_2/C_1)e^{-Pe}]}{[1-e^{-Pe}]} \\
Pe &= \frac{W\langle V \rangle L}{HD_\infty} \\
H &= \Phi K_d = 2\int_0^{1-\lambda} K^{-1} e^{-\psi(\beta)} \beta d\beta \\
W &= \Phi K_c = 4\int_0^{1-\lambda} G(1-\beta^2) e^{-\psi(\beta)} \beta d\beta \\
\Phi &= (1-\lambda)^2
\end{aligned} \tag{1.33}$$

The limiting forms for the flux are given by

$$\begin{aligned}
\langle N \rangle &= \frac{HD_\infty}{L}(C_1 - C_2) \qquad (Pe << 1) \\
\langle N \rangle &= W \langle V \rangle C_1 \qquad (Pe >> 1)
\end{aligned} \tag{1.34}$$

The solute transport is dominated by convection when *Pe>>1*. The reflection coefficient for filtration for convective transport of solute is defined by

$$\sigma_f = 1 - W \tag{1.34}$$

and can be interpreted as the fraction of the solute rejected when convection is dominant (Deen 1987).

An important conclusion of this research is to determine if the filtration reflection coefficient is equal to the osmotic reflection coefficient or the test of reciprocity. As pointed out above the Anderson and Malone model predicts that the two coefficients are not identical (Anderson and Malone 1974). The hydrodynamic theory of sieving enables one to relate the filtration reflection coefficient to the hydrodynamic coefficients as shown in equation (1.32) above. Results for these coefficients are available for a wide range of values of the parameter λ and for axisymmetric and non axisymmetric cases (Deen 1987, Dechadilok and Deen 2006). This would enable a test of reciprocity for the case of porous membranes.

1.8 Thesis overview

The ultimate goal of this research was to extend the theories of osmotic flow for charged fibrous membranes. Fibrous materials occur in both physiological and non-physiological systems for eg. connective tissue and basement membranes. The fibers could be charged and could be multichain polymeric aggregates. Zhang et al. have extended the Anderson and Malone model to calculate σ_0 for neutral spheres in membranes consisting of regular arrays of neutral fibers (Zhang et al. 2006). As far as we know, no one has worked out corresponding results for charged spheres in a charged fiber array.

The work begins by investigating the Anderson and Malone model in a greater detail (Anderson and Malone 1974). The underlying conceptual difficulty in the Anderson and Malone model is the ambiguity that can arise when defining concentrations of finite sized molecules. An obvious choice for describing the concentration is the solute

centroid, however once could choose a different basis for the same. This in turn leads to differing pressure profiles in the Anderson and Malone framework. This is discussed in Chapter 2 and a conceptually different model to calculate osmotic reflection coefficient in porous membranes is presented. The quantitative differences in σ_o between the two methods was not found to be appreciable. Also an important objective of the study is to extend theoretical predicitons for σ_0 to a wider variety of molecular shapes. Results were obtained for prolate and oblate spheroids of varying axial ratios, for both cylindrical and slit pores. This work was published (Bhalla and Deen 2007).

The development of a model to predict osmotic reflection coefficient in charged porous membranes is the topic of Chapter 3. There are few results in the literature for charged solutes. Sasidhar and Ruckenstein used a diffuse double-layer model to examine osmotic flow due to differences in electrolyte concentration, but steric exclusion was not considered (Sasidhar and Ruckenstein 1981). This work was published (Bhalla and Deen 2008).

Finally in Chapter 4, a computational model to predict the effects of solute and fiber charge density on osmotic reflection coefficient (σ_0) of spherical macromolecules in charged fiber arrays is presented. This work has been submitted for publication.

Chapter 2. EFFECTS OF MOLECULAR SHAPE ON OSMOTIC REFLECTION COEFFICIENTS

2.1 INTRODUCTION

The objective of the present work was to extend theoretical predicitons for σ_0 to a wider variety of molecular shapes. Results were obtained for prolate and oblate spheroids of varying axial ratios, for both cylindrical and slit pores. The theoretical effects of molecular shape on reflection coefficients are of interest, for example, in interpreting data on the ultrafiltration of globular proteins, which are often modeled as spheroids (Tanford 1961). As will be discussed, σ_o is expected to provide a good approximation to the reflection coefficient for filtration, so that the results offer insight into filtration processes as well as osmotic flow. In extending the available results, the approach used previously by others to evaluate intrapore pressure gradients was reexamined. An alternative strategy is proposed which is conceptually different, although it yields similar results.

2.2 THEORY

2.2.1 Assumptions

The solutes are viewed as uncharged, rigid, Brownian particles and the solvent is modeled as a continuum. Thus, the characteristic linear dimension of a solute molecule is assumed to greatly exceed that of the solvent. Of primary interest are solute sizes that are comparable to the cross-sectional dimension of a pore (R or H), which will lead to intermediate values for σ_o. The pores are assumed to be long enough to neglect hydrodynamic end effects and to apply equilibrium conditions at the ends. At the low Reynolds numbers that pertain to flow through pores of macromolecular dimensions (Re $<<$ 1), hydrodynamic entrance lengths in channels are on the order of R or H. This is also the length scale for the concentration transitions at the pore ends, so that $L/R >> 1$ or $L/H >> 1$ is sufficient for both purposes. It is assumed further that the solutes have ample time to sample all radial positions while passing through a pore. For that it is sufficient that Pe $<<$ 1, where Pe is a Peclet number based on the mean fluid velocity and either R or H. Under these conditions, radial variations in solute concentration will closely resemble those at equilibrium, despite the axial variations caused by differing external concentrations (Brenner and Gaydos 1977). Finally, the solutions are assumed to be dilute enough to employ van't Hoff's law and to equate the solution viscosity with that of the solvent.

2.2.2 Fluid dynamic problem

The combination of low Re and large length-to-width ratio justifies use of the lubrication approximation, as detailed previously (Anderson and Malone 1974). For the cylindrical geometry, the z and r components of the simplified momentum conservation equation are written as

$$0 = -\frac{\partial P}{\partial z} + \frac{\mu}{r}\frac{\partial}{\partial r}\left(r\frac{\partial u}{\partial r}\right) \tag{2.1}$$

$$0 = \frac{\partial}{\partial r}(P - \Pi) \tag{2.2}$$

where $u(r,z)$ is the axial component of the fluid velocity, $P(r,z)$ is the pressure, and μ is the viscosity. This formulation supposes that the sole effect of the solute particles is to create a local osmotic pressure, $\Pi(r,z)$, which is proportional to solute concentration. By "concentration" we mean the relative probability of finding a solute molecule in a pore, times an external concentration that is chosen as a reference. Implicit in the model is that the process or observation time is long enough to make the intrapore probability density a continuous function. In other words, equations (2.1) and (2.2) are time-averaged expressions that are intended to encompass all possible particle configurations (positions and orientations). The "snapshot" in Figure 1.2 depicts a single configuration for spheres.

For point-sized molecules there is no ambiguity in the meaning of local concentration. However, a solute whose size is finite relative to the system (pore) dimensions spans many points, and one must select a "locator point" to define its position. The locator point can be anywhere in the solute particle, provided it is used consistently. For a symmetric particle the geometric center is usually most convenient,

but any other point is equally valid. (As with a center of volume or center of mass, the locator point need not reside inside the solid if the particle is not convex.) A particle of arbitrary shape requires three angles to specify its orientaion. When an axis of symmetry is used to define orientations, as for capsules (Anderson 1981) and for the spheroids considered here, only two angles are needed: θ is the polar angle describing the tilt of the particle axis relative to a line that is perpendicular to the pore axis ($0 \leq \theta \leq \pi$), and ϕ is the azimuthal angle describing rotations about that reference line ($0 \leq \phi \leq 2\pi$).

If $\partial \Pi / \partial r$ can be evaluated independently (and analytically), the solution procedure for the fluid dynamic problem is straightforward. That is, equation (2.2) can be integrated to find $P(r,z)$, the result used to evaluate $\partial P / \partial z$, and equation (2.1) integrated twice to find $u(r,z)$, which is subject to the usual symmetry and no-slip conditions. Thus, it is the evaluation of $\Pi(r,z)$ that is crucial for finding the fluid velocity and, ultimately, σ_o. Two approaches for calculating Π are discussed next.

2.2.3 Osmotic pressure from concentration of particle centers

The first approach is equivalent to what was done in previous analyses (Anderson and Malone 1974, Anderson 1981, Zhang et al. 2006). In this method it is supposed that van't Hoff's law can be used to relate Π to the concentration of solute centers, $C(r,z)$. That is, C is defined by choosing the center of volume of a particle as its locator point, and it is assumed that

$$\Pi(r,z) = kTC(r,z) \tag{2.3}$$

Using this approach, what remains to be specified is the effect of the pore wall on the solute concentration profile.

To allow for the possibility of both steric and long-range interactions, the solute-wall force is expressed in terms of a dimensionless potential ψ (potential energy relative to kT), as in Anderson (Anderson 1981). This potential depends on the radial position and orientation of a particle, but not its axial position, and $\psi = 0$ in the external bulk solutions. Given the assumption of radial equilibrium of the solute, the concentration field in the pore will be of the form

$$C(r,z) = f(z)\{\exp(-\psi)\} \tag{2.4}$$

where the curved brackets denote an average over all solute orientations. The probability of a particle having a given radial postion and orientation is proportional to a Boltzmann factor, exp ($-\psi$), that involves the corresponding energy. The orientation-averaged Boltzmann factor for a solute centered at position r is

$$\{\exp(-\psi)\} \equiv \frac{1}{4\pi}\iint \exp[-\psi(r,\theta,\phi)]\sin\theta\, d\theta\, d\phi \tag{2.5}$$

Thus, the solute concentration at a point encompasses all possible orientations. The function $f(z)$ in equation (2.4) is related to the centerline concentration (C_0) and centerline potential (ψ_0). At any given axial position, $f(z) = C_0(z)/\exp\{-\psi_0\}$; at the pore ends, $f(z)$ equals the external concentration.

Combining equations (2.2)-(2.4), the pressure distribution is found to be

$$\begin{aligned} P(r,z) &= P_0(z) + \Pi(r,z) - \Pi_0(z) \\ &= P_0(z) + kTf(z)\{\exp(-\psi) - \exp(-\psi_0)\} \end{aligned} \tag{2.6}$$

where P_0 is the pressure at the centerline. Although obtained somewhat differently, this is the same as equation (8) in Anderson (Anderson 1981). The calculation of σ_o can be completed by using equation 8 to evaluate the pressure gradient in equation 3, and then

integrating over r and z (Anderson 1981). Although straightforward in principle, that procedure is tedious and at times impractical, depending on the functional form of the potential. A shortcut for evaluating σ_o is described later.

A sphere that experiences only steric (hard-sphere-hard-wall) interactions is an important special case, in which $\psi = \infty$ for sphere-wall overlaps but $\psi = 0$ otherwise. Noting that $\psi_0 = 0$ and $f(z) = C_0(z)$ in this situation, it follows from equations (2.4) and (2.6) that

$$C(r,z) = \begin{cases} C_0(z) & \text{for } 0 \le r < R-a \\ 0 & \text{for } r > R-a \end{cases} \tag{2.7}$$

$$P(r,z) = \begin{cases} P_0(z) & \text{for } 0 \le r < R-a \\ P_0(z) - kTC_0(z) & \text{for } r > R-a \end{cases} \tag{2.8}$$

Thus, the step change in the concentration of particle centers at $r = R - a$, together with the use of the concentration of centers to evaluate Π, implies a radial step change in pressure.

2.2.4 Osmotic pressure from particle volume fraction

An alternative approach is to relate the osmotic pressure to the solute volume fraction (φ). Noting that $\varphi = CV$, where V is the molecular volume of the solute, van't Hoff's law rearranges to

$$\Pi(r,z) = \frac{kT}{V}\varphi(r,z) \tag{2.9}$$

which in this approach replaces equation (2.3). What is needed in using equation (2.9) to find σ_o is the radial dependence of φ. This was determined for three solute-pore combinations, assuming steric interactions only: spheres in cylindrical pores, spheres in

slits, and spheroids in slits. As shown in the Appendix A, this involved averaging the solid volume due to a single particle over all particle positions and orientations, analytically or numerically. Reasons for preferring this approach over that based on equation (2.3) are discussed later.

2.2.5 Calculation of reflection coefficient

Using the first approach for evaluating the intrapore osmotic pressure (based on particle centers), Anderson (Anderson 1981) showed that the osmotic reflection coefficient can be calculated as

$$\sigma_o = 1 - \frac{\left\langle u^* \left\{ \exp(-\psi) \right\} \right\rangle}{\left\langle u^* \right\rangle} \tag{2.10}$$

where u^* is the axial velocity profile for ordinary Poiseuille flow in the pore shape of interest, and the angle brackets denote averages over the pore cross-section. (The present definition of u^* differs by a prop ortionality constant from that in (Anderson 1981), but the constants cancel in equation (2.10)) This expression, which was derived using a reciprocal theorem due to Reed (Reed 1978), allows σ_o to be found without solving the flow problem outlined above. For example, for a hard sphere in a cylindrical pore, the potential is given by

$$\psi(r) = \begin{cases} 0 & \text{for } 0 \le r < R - a \\ \infty & \text{for } r > R - a \end{cases} \tag{2.11}$$

Equation (1.26) is obtained simply by using equation (2.11) and the usual parabolic velocity profile in equation (2.10). The analogous result for a sphere in a slit pore (equaton (1.27)) is found in the same way. For nonspherical particles, orientation-

averaging of the Boltzmann factor is required before integration over the pore cross-section. In general, numerical integration is required for both averaging steps.

The second approach for evaluating the osmotic pressure (based on volume fraction) does not employ a solute-wall potential to describe steric interactions. However, formal consistency between equations (2.6) and (2.9) can be maintained by replacing the orientation-averaged Boltzmann factor by φ/φ_∞, where φ_∞ is the volume fraction that would exist in a bulk solution in equilibrium with the pore. With this substitution, equation (2.10) becomes

$$\sigma_o = 1 - \frac{\left\langle u^* \varphi / \varphi_\infty \right\rangle}{\left\langle u^* \right\rangle} \quad . \tag{2.12}$$

Thus, the simplification that results from use of the Reed reciprocal theorem can be exploited using either approach.

2.2.6 Prolate and oblate spheroids

Spheroids are ellipsoids in which two axes are equal. The three semi-axes are denoted here as (a, a, b) and the axial ratio is $\gamma = b/a$. Prolate (elongated) and oblate (flattened) spheroids are defined by $\gamma > 1$ and $\gamma < 1$, respectively. The definitions of a and b are depicted in Figure 2.1

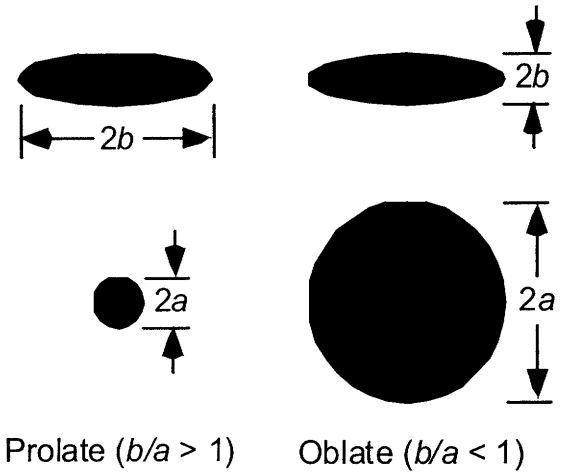

Figure 2.1 Definitions for prolate and oblate spheroids. Two views are shown for each particle shape.

The most accessible measure of molecular size experimentally is often the Stokes-Einstein radius (a_{SE}), which is the radius of a sphere that would have the same diffusivity. The Stokes-Einstein radii of the spheroids are given by (Brenner 1974)

$$\frac{a_{SE}}{a} = \frac{\gamma p}{\ln\left[\gamma\left(1+p\right)\right]}, \quad p = \sqrt{1-\gamma^{-2}} \qquad \text{(prolate)} \qquad (2.13)$$

$$\frac{a_{SE}}{a} = \frac{\gamma q}{\tan^{-1} q}, \quad q = \sqrt{\gamma^{-2}-1} \qquad \text{(oblate)} \qquad (2.14)$$

The results to be presented will use either a or a_{SE} as the measure of molecular size. Of course, for a sphere, $a = a_{SE}$ and $\gamma = 1$.

2.3 RESULTS

Figure 2.2 shows transverse pressure variations for spheres in slits that were calculated using three methods, with $a/H = 0.5$ in each case. Two of the methods are those described above, using either the concentration of particle centers (equation (2.3)) or the particle volume fraction (equation (2.9)) to evaluate the osmotic pressure. The third method is a variant of the first, in which calculations were done using a point on the

sphere surface as the locator. In that case the concentration in equation (2.3) was redefined as the number density of the surface points (instead of the number density of sphere centers). Given the eccentric position of this particular locator, orientation-averaging was required to evaluate the concentration as a function of radial position. As seen in Figure 2.2, the three methods yielded very different pressure profiles, mirroring the different concentration or volume fraction profiles. As already mentioned, a center locator implies a step decrease in concentration upon contact with the wall, so there is a step decrease in P. A surface locator turns out to give a linear decrease in concentration for $a/H = 0.5$ and therefore a linear decrease in P. The difference in these two pressure profiles shows that equation (2.3) leads to different results, depending on how the locator point is defined. Basing the osmotic pressure on the solute volume fraction yielded a sigmoidal pressure profile, as shown.

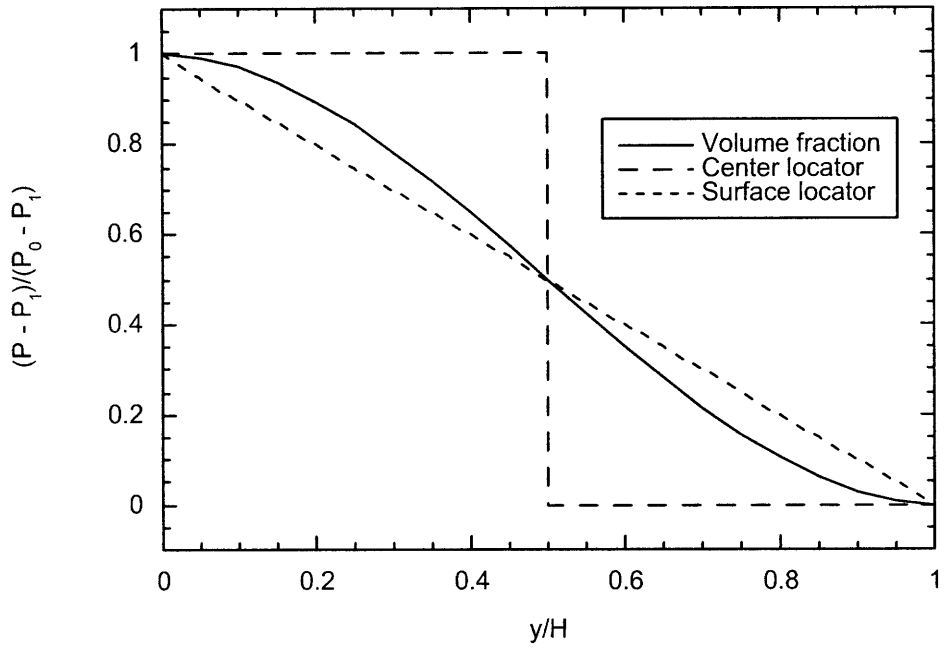

Figure 2.2 Pressure profiles for a sphere in a slit, with $a/H = 0.5$. Pressures at the pore midplane ($y = 0$) and pore wall ($y/H = 1$) are denoted as P_0 and P_1, respectively. The curves correspond to three methods for calculating the intrapore osmotic pressure, using the sphere volume fraction (equation (2.9)), the concentration of sphere centers (equation (2.3)), or the concentration of sphere surface points (equation (2.3) with corresponding redefinition of C).

Osmotic reflection coefficients for spheres in slit pores are shown in Figure 2.3 Values of σ_o are given as a function of relative solute size (a/H) for each of the three methods for evaluating pressures just discussed. In each case, σ_o increased smoothly from 0 to 1 as a/H was increased over that range. The highest values of σ_o were obtained for the surface locator and the lowest for the center locator, with the volume fraction yielding intermediate results. The curve for the center locator corresponds to equation (1.27), and the result based on the volume fraction is

$$\sigma_o = \frac{9}{5}\lambda^2 - \frac{4}{5}\lambda^3 \tag{2.15}$$

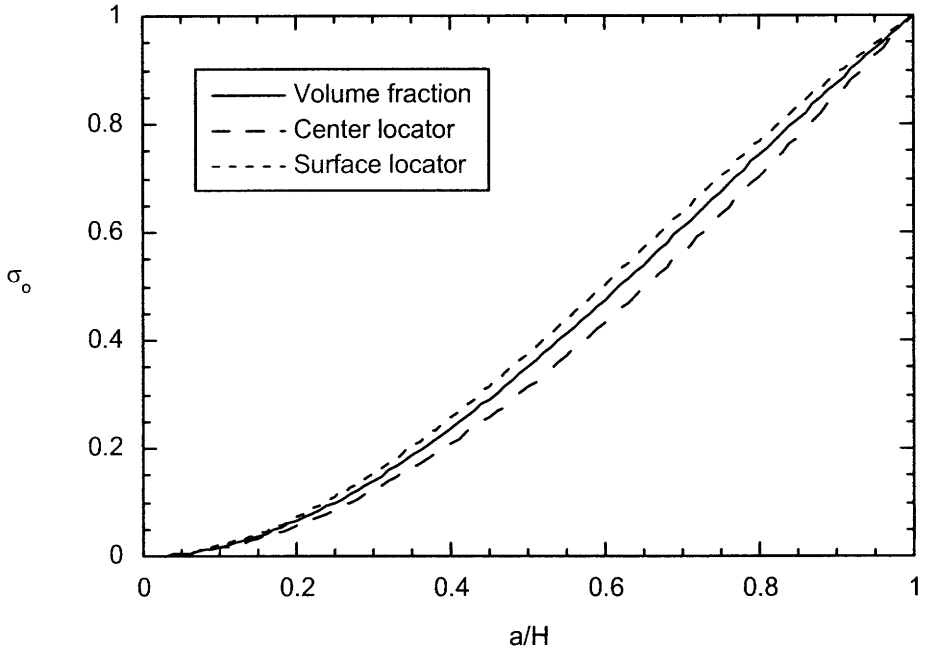

Figure 2.3 Osmotic reflection coefficients for spheres in slits, based on the three methods for calculating pressures identified in Figure 2.2

As shown in Figure 2.4, the trends for spheres in cylindrical pores were similar to those for spheres in slits. Again, the volume fraction method gave somewhat higher values than the center locator approach (which corresponds to equation (1.26)). For the volume fraction method, a least-squares fit to the numerical results gave

$$\sigma_o = 4.80\lambda^2 - 5.60\lambda^3 + 1.80\lambda^4 \ . \tag{2.16}$$

Calculations based on a surface locator were not done for cylindrical pores.

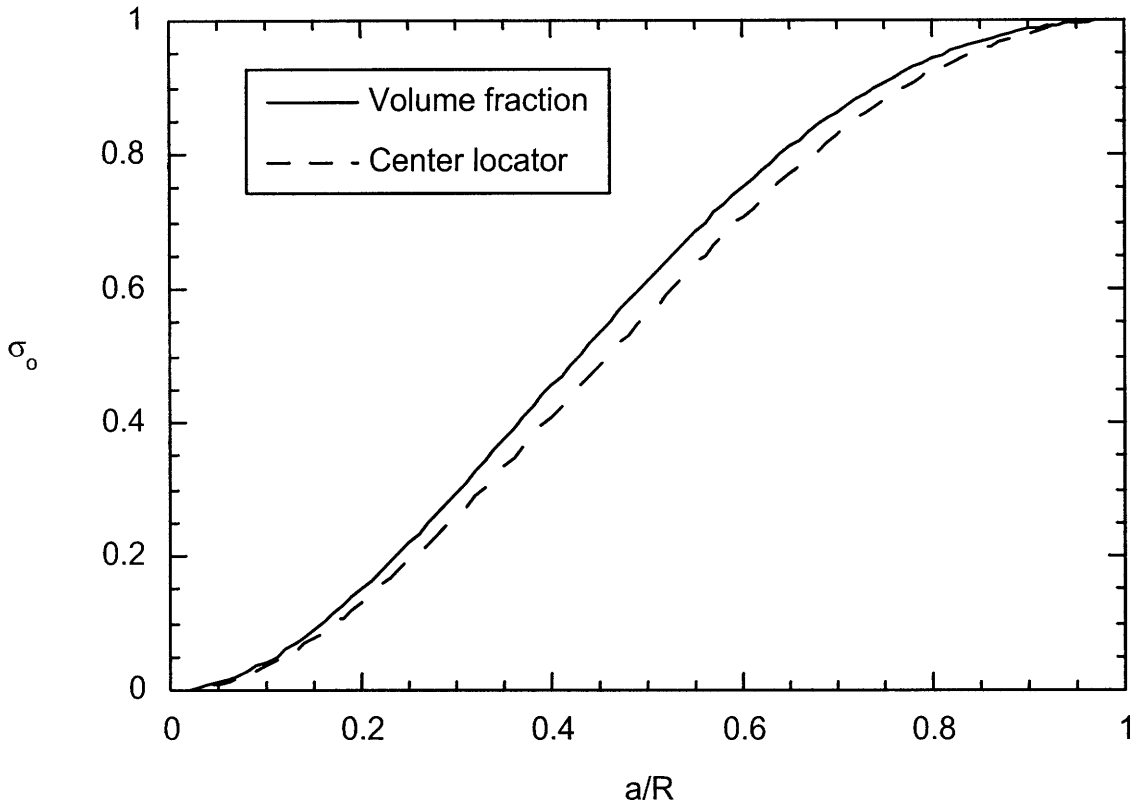

Figure 2.4 Osmotic reflection coefficients for spheres in cylindrical pores, using either the sphere volume fraction (equation (2.9)) or the concentration of sphere centers (equation (2.3)) to evaluate pressures.

Results for prolate spheroids in slits are plotted in Figure 2.5. For a given value of a/H (minor semi-axis relative to slit half-width), σ_o was found to increase monotonically with increasing elongation of the solute (increasing b/a). Once again, the values obtained using the volume fraction method were consistently higher than those using the center locator approach, although the differences were small. A peculiar aspect of the parallel-plate geometry is that the results for oblate and prolate spheroids are identical if a and b are interchanged. That is true for either method for evaluating

pressures. Thus, results for oblate spheroids in slits can also be obtained from Figure 2.5, interchanging a and b.

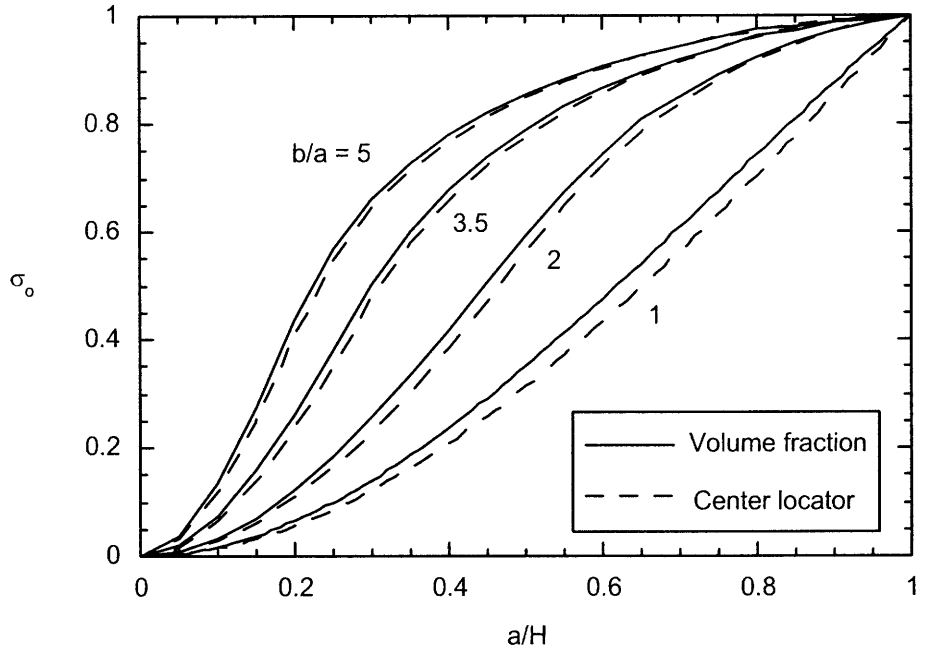

Figure 2.5 Osmotic reflection coefficients for prolate spheroids in slits, with the minor semi-axis (a) taken as the measure of molecular size. Results based on two methods for calculating pressures (volume fraction, equation (2.9); center locator, equation (2.3)) are shown for each of four axial ratios (b/a). As a reference, results for spheres (a/b = 1) are repeated from Figure 2.3. Results for oblate spheroids in slits may be found from this plot by interchanging a and b.

Figure 2.6 shows osmotic reflection coefficients for prolate and oblate spheroids in cylindrical pores, with a/R as the abscissa. What makes a/R a natural choice is that all the spheroids are close fits for a/R = 1, independent of the axial ratio. In that limit only one orientation is allowed for either a prolate or an oblate particle, the one that

completely occludes the pore. It is seen that, for a given a/R, there was a monotonic increase in σ_o with increasing b/a. When plotted in this manner, the results are very sensitive to particle shape. For example, at $a/R = 0.2$, the values of σ_o ranged from 0.05 at $b/a = 0.2$ to 0.80 at $b/a = 5$. Because of the difficulty in calculating configuration-averaged volume fractions for this geometry, all of these calculations were based on the center locator method.

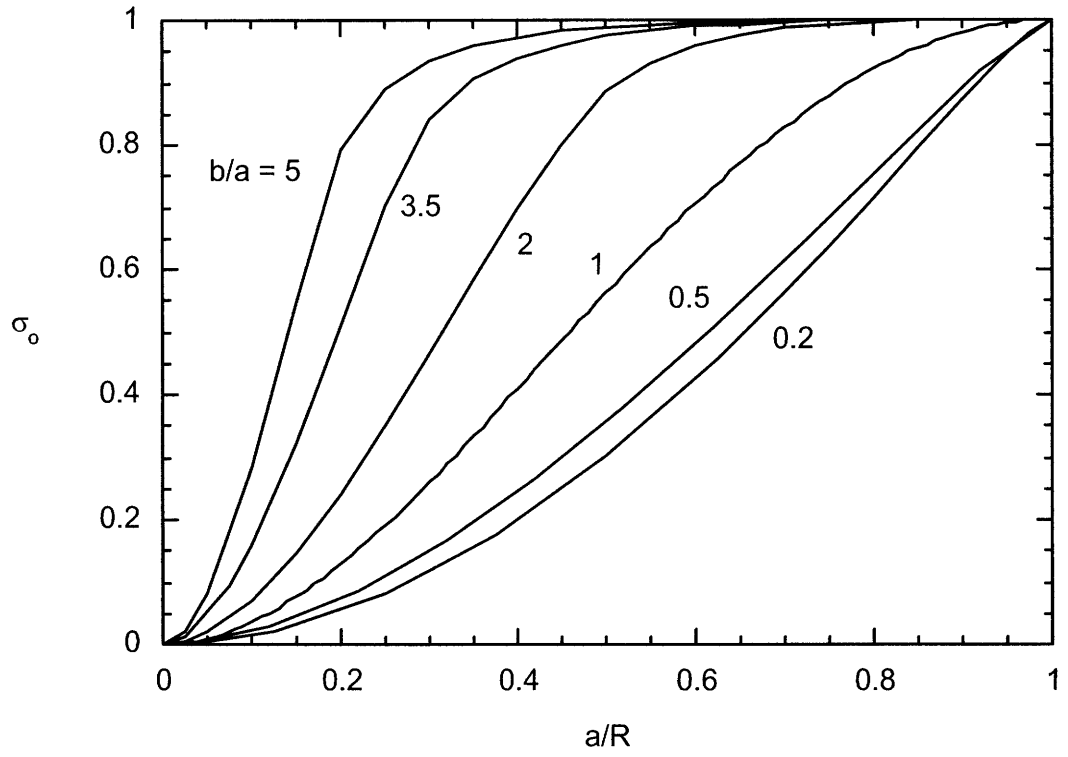

Figure 2.6 Osmotic reflection coefficients for spheroids in cylindrical pores, with the semi-axis a taken as the measure of molecular size. Included are results for prolate spheroids ($b/a > 1$), spheres ($b/a = 1$), and oblate spheroids ($b/a < 1$). All of these results were calculated using center locators (equation (2.3)).

The results for cylindrical pores are replotted in Figure 2.7, with a_{SE}/R as the abscissa. The motivation for this plot is that a_{SE} is the linear dimension that is most likely

to be known for a given molecule (from diffusivity data). When displayed in this manner, the results for the various particle shapes are brought closer together. There is an inversion in the curves for the oblate spheroids, the results for $b/a = 0.2$ now falling above those for $b/a = 0.5$. The oblate curves now intersect those for spheres and prolate particles, and terminate at $a_{SE}/R < 1$. The early termination is a consequence of the small a_{SE}/a values of oblate spheroids (from equation (2.14)); as their size is increased, they reach a condition of complete steric exclusion before a_{SE} equals that for a close-fitting sphere. Although less evident on the scale of Figure 2.7, the opposite occurs for prolate spheroids. That is, the large values of a_{SE}/a (equation (2.13)) delay the termination of the prolate curves until $a_{SE}/R > 1$. Because in this case the inversion of the curves is restricted to large values of σ_o (> 0.95), it is less obvious visually and also less likely to be detected experimentally. The plot for slit pores using a_{SE}/H was qualitatively similar to Figure 2.7 and is shown in Figure 2.8. That is, the curves for spheroids of differing shape were brought closer together and some of the trends from Figure 2.6 were inverted.

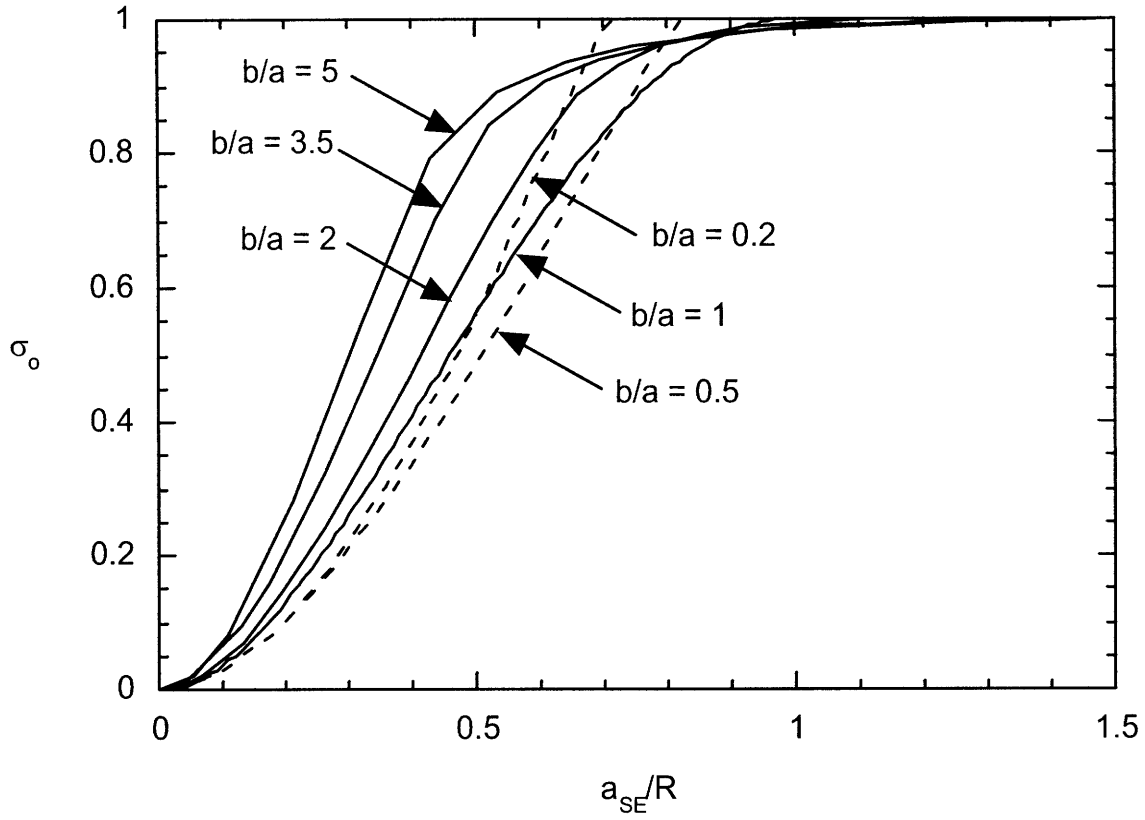

Figure 2.7 Osmotic reflection coefficients for spheroids in cylindrical pores, with the Stokes radius a_{SE} taken as the measure of molecular size. Included are results for prolate spheroids ($b/a > 1$), spheres ($b/a = 1$), and oblate spheroids ($b/a < 1$), all calculated using center locators (equation (2.3)).

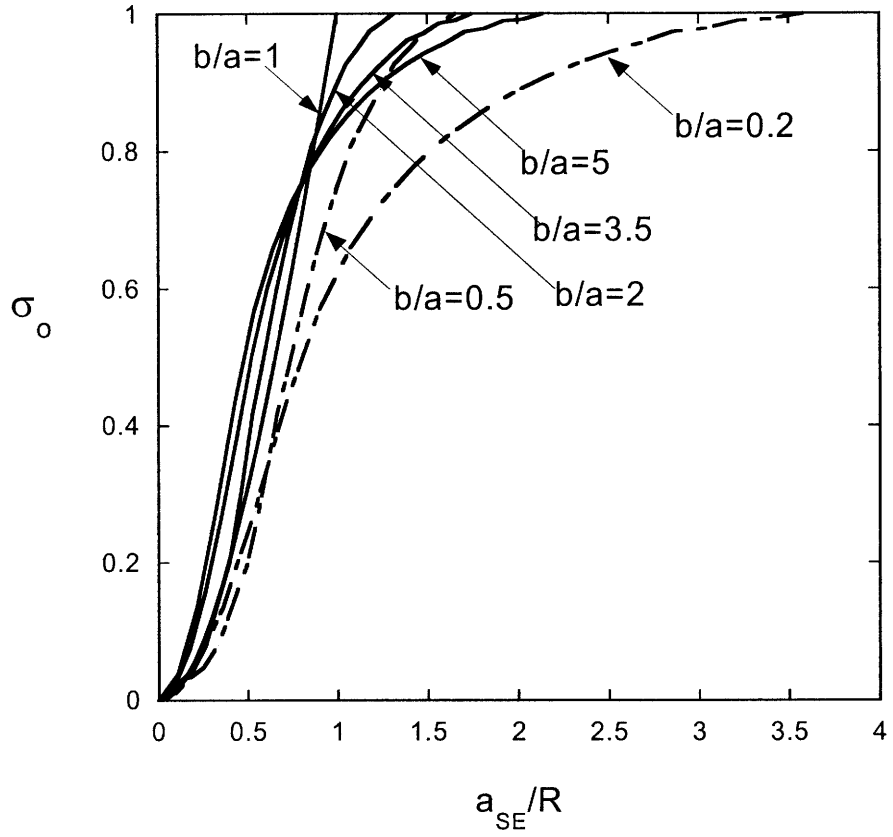

Figure 2.8 Osmotic reflection coefficients for spheroids in slit pores, with the Stokes radius a_{SE} taken as the measure of molecular size. Included are results for prolate spheroids ($b/a > 1$), spheres ($b/a = 1$), and oblate spheroids ($b/a < 1$), all calculated using center locators (equation (2.3)).

2.4 DISCUSSION

Two principal methods were presented for predicting osmotic reflection coefficients, differing only in the way the osmotic pressure profile is evaluated inside a pore. The underlying conceptual difficulty is the ambiguity that can arise in defining solute concentrations when the molecules have finite dimensions. Equation (2.3), which

is equivalent to what has been used previously by others (Anderson and Malone 1974, Anderson 1981, Zhang et al. 2006), relates the local osmotic pressure to the concentration of particle centers. The center of volume of a particle is certainly a valid locator point for defining concentrations, and is intuitively attractive, but it is not more correct than any other reference point that might be chosen. Indeed, a locator point is only a label, and physically meaningful results must be label-independent. For example, in calculating the equilibrium partition coefficient for a rod-like molecule between a pore and bulk solution, the center and one end of the molecule are equally valid locator points, and if positions and orientations are described in a self-consistent manner, the final result (mean internal concentration divided by external concentration) is independent of which was chosen. The problem with equation (2.3) is that the evaluation of Π depends on the choice of locator point for the particle (Figure 2.2), and the osmotic pressure profile in turn affects the value of σ_o that is found (Figure 2.3). Thus, equation (2.3) fails to provide label-independent results. Not as fundamentally objectionable, but still difficult to accept, are the radial step changes in pressure that are implied when the particle center is chosen (Figure 2.2).

The alternative method, based on equation (2.9), uses configuration-averaged volume fractions to evaluate osmotic pressures. Such averaging makes the volume fraction and osmotic pressure profiles independent of the solute locator point, and thus yields label-independent results. Also, because at least some part of any convex particle that enters a pore can access all radial positions, up to contact with the pore wall, the configuration-averaged volume fraction falls to zero only at the wall. Because $\varphi(r,z)$ in a

cylindrical pore is a continuous function of r, equation (2.9) does not imply step changes in pressure. Thus, both objections to the first approach are avoided.

The label-dependence inherent in the use of any point concentration in equation (2.3) indicates that the corresponding values of σ_o must be at least slightly erroneous. Accordingly, it seems likely that using volume fractions (equation (2.9)) will yield more accurate results. However, in none of the geometries considered were the differences in σ_o between the two methods appreciable. That was true for spheres in slits (Figure 2.3, spheres in cylindrical pores (Figure 2.4), and spheroids in slits (Figure 2.5). In each case it is very unlikely that the two predictions could be distinguished experimentally. Because the use of solute centers is much easier computationally, and seems to result in only small errors, it offers the best opportunity for extending the available results for σ_o to other solute and pore geometries. Thus, equation (2.3) was employed in all of our calculations for spheroids in cylindrical pores.

Closely related to σ_o is the reflection coefficient for filtration, σ_f. At membrane Peclet numbers high enough to make transmembrane diffusion negligible, $\sigma_f = 1 - \Theta$, where Θ is the membrane sieving coefficient (filtrate concentration divided by concentration at upstream membrane surface). Both reflection coefficients approach unity for "tight" membranes and zero for "leaky" ones, and for intermediate situations it has been argued from continuum mechanical models that they are either identical (Levitt 1975) or approximately equal (Anderson 1981). A recent update of hindered transport theory (Dechadilok and Deen 2006) provides improved predictions of σ_f for neutral spheres in cylindrical pores or slits, which are compared in Figure 2.8 with the present results for σ_o. The results for each geometry support the conclusion that the two

reflection coefficients are nearly equal. Just as σ_o (using the volume fraction method) is slightly higher than previous results, so is the updated σ_f. Thus, the comparison for cylindrical pores in Figure 2.9 looks much like Figure 1.3 of Anderson (Anderson 1981). A practical consequence of the near-equality of σ_o and σ_f is that the former, which is much easier to calculate, can be used to estimate the latter. For prolate or oblate spheroids in either pore geometry, there appear to be no results in the literature for σ_f that correspond to the present ones for σ_o.

A quantity which is closely related to the reflection coefficients is the partition coefficient, Φ, which is the average intrapore concentration divided by that in bulk solution, at equilibrium. For rigid particles in pores of uniform cross-section, it is given by

$$\Phi = \left\{\exp\left(-\psi\right)\right\} \quad . \tag{2.17}$$

For spheres in cylindrical pores and slits, $\Phi = (1- \lambda)^2$ and $(1- \lambda)$, respectively. Thus, equation (1.26) and (1.27) may be rewritten as

$$\sigma_o = \left(1 - \Phi\right)^2 \qquad \text{(cylindrical pores)} \tag{2.18a}$$

$$\sigma_o = 1 - \frac{3}{2}\Phi + \frac{1}{2}\Phi^3 \qquad \text{(slits)} \tag{2.18b}$$

as pointed out previously (Anderson and Malone 1974, Anderson 1981). For $\Phi = 0.4$, the value of σ_o for spheres in slits is predicted to be 18% larger than that for spheres in cylindrical pores (0.42 vs. 0.36). The values of σ_o for spheres in the two pore geometries are much closer when compared in this manner than they are when compared at a given λ (Figure 2.10).

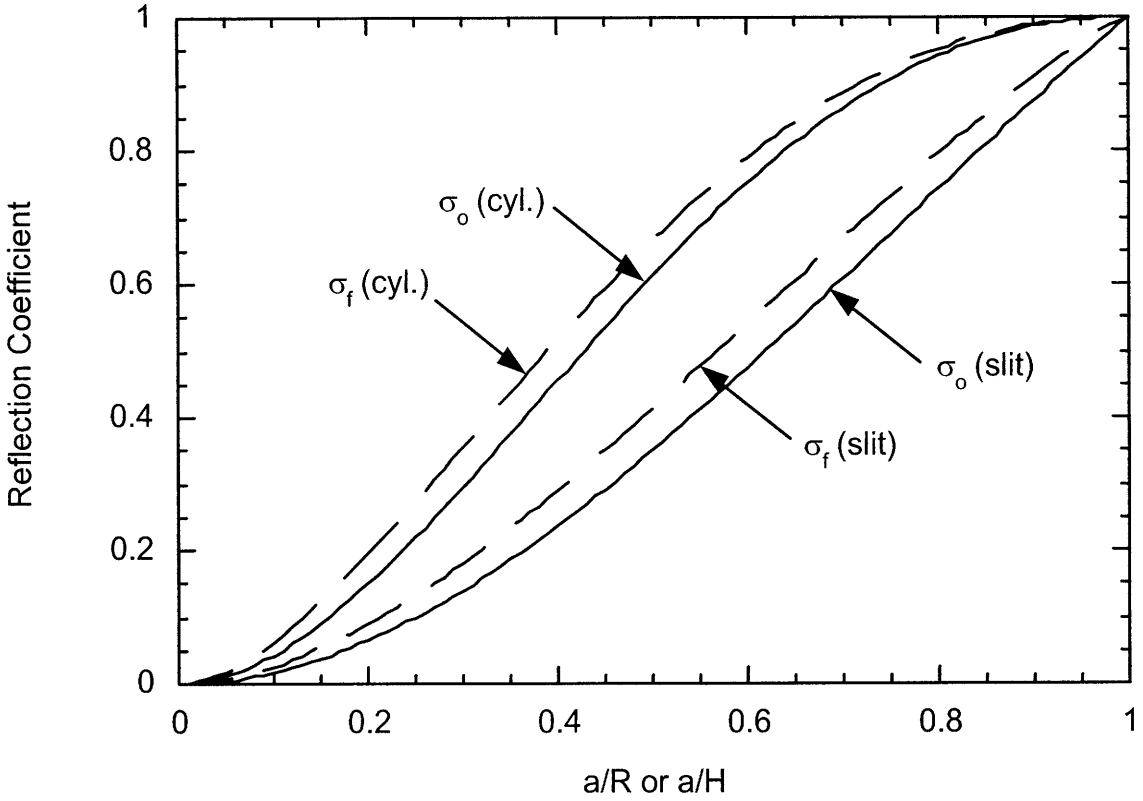

Figure 2.9 Comparison of osmotic and filtration reflection coefficients for spheres. Osmotic reflection coefficients (σ_o) for both pore shapes are based on the volume fraction method for evaluating pressures (equation (2.9)). Filtration reflection coefficients (σ_f) are based on recent results from hindered transport theory that include off-axis hydrodynamic data (Dechadilok and Deen 2006); in the notation of that paper, $\sigma_f = 1 - W$.

To test how universal might be the correlations between σ_o and Φ, results for spheroids of all axial ratios are plotted in Figure 2.10. For consistency, all of the σ_o calculations used here were based on equation (2.3). The range of axial ratios considered for each pore shape was the same as that in Figure 2.6. It is seen in Figure 2.10 that all results for cylindrical pores closely follow equation (2.18a), whereas those for slit pores adhere to equation (2.18b). Thus, when examined in this way, the effects of molecular

shape are less important than the effects of pore shape. Although interesting, the correlations between σ_o and Φ for various particle shapes appear to be of little practical value. In particular, finding Φ does not provide a shortcut for estimating σ_o, because nearly the same computational effort is required to obtain either quantity.

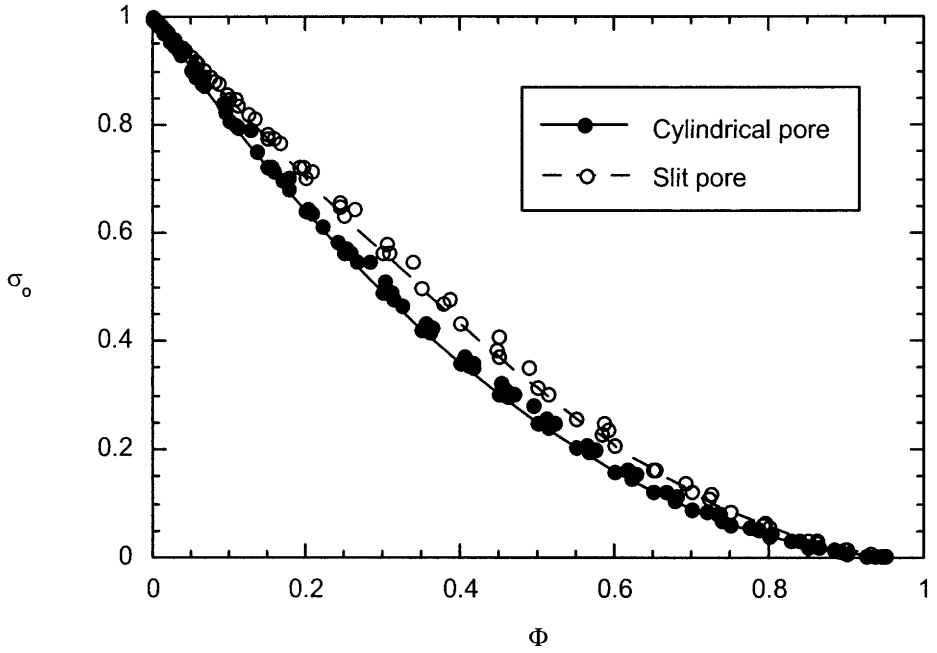

Figure 2.10 Relationship between osmotic reflection coefficient (σ_o) and equilibrium partition coefficient (Φ) for spheroids in cylindrical or slit pores. Included are results for all axial ratios shown in Figures 2.6 and 1.8, using center locator points. The solid and dashed curves correspond to equations (2.18a) and (2.18b), respectively.

The methodology employed here could be used to predict osmotic reflection coefficients for more complex pore shapes and/or for solutes that experience long-range interactions with the pore walls.

As shown in the chapter, for uncharged macromolecules, σ_0 has been evaluated for a variety of situations. There are few results in the literature for charged solutes. Sasidhar and Ruckenstein used a diffuse double-layer model to examine osmotic flow due to differences in electrolyte concentration (Sasidhar and Ruckenstein 1981). Numerical solutions of the Poisson-Boltzmann, species continuity, and momentum equations for specified differences in external salt concentration yielded values for σ_0. Steric exclusion was not considered (i.e., the ions were assumed to be point-sized).Given that soluble proteins typically carry a net charge, and that synthetic and biological membrane materials also tend to have a surface charge, a valuable direction for future extensions of the theory would be to include electrostatic forces for finite sized molecules. This is the topic of the next Chapter.

Chapter 3. EFFECT OF CHARGE ON OSMOTIC REFLECTION COEFFICEINTS OF MACROMOLECULES IN POROUS MEMBRANES

3.1 INTRODUCTION

It has been proposed that both size and charge effects can be captured by employing the potential energy change E associated with placing a solute molecule at a given radial position in a pore. In dilute solutions, and in pores long enough to allow the molecule to sample all radial positions, the relative probability of the molecule being at a given position is given by a Boltzmann factor, exp(*-E/kT)*. For a spherical macromolecule in a cylindrical pore, the expression for the osmotic reflection coefficient that has been proposed is

$$\sigma_0 = 1 - 4\int_0^{1-\lambda} e^{-E/kT}(1-\beta^2)\beta\, d\beta \tag{3.1}$$

where λ (= a/b) is relative solute radius and β (= r/b) is relative radial position (Anderson 1981, Deen 1987). Although results for E for charged spheres in charged cylindrical pores have been available for some time, corresponding results for σ_o have not been reported (Deen 1982).

The objective of the present work was to provide numerical results for σ_o for charged spheres in charged pores. As will be explained, one limitation of equation (3.1) is that it neglects streaming potentials, which retard the flow and may alter the shape of the velocity profile in small, charged pores. To examine whether or not this electrokinetic phenomenon influences σ_o, we developed a more general formulation. Another potential source of error is the Debye-Huckel approximation (linearization of the Poisson-Boltzmann equation), which was needed to obtain analytical results for E (Deen 1982). Numerical results for E were obtained for situations where that approximation should be inaccurate (high surface charge densities and/or large Debye lengths) and compared with the previous analytical results. Surprisingly, neither source of error proved to be significant in the calculation of σ_o, and equation (3.1) was found to be quite accurate.

3.2 THEORY

3.2.1 Assumptions

Dilute solutions of spherical macromolecules were assumed to be separated by a membrane having long cylindrical pores, the solutes and pores each having specified linear dimensions and surface charge densities. Also present were univalent anions and cations, each of negligible size relative to the macromolecule or pore. The bulk

electrolyte concentrations on the two sides were assumed to be equal, so that osmosis resulted only from an imbalance in macromolecule concentrations. Because filtration processes typically operate under open-circuit conditions, zero current was imposed as the macroscopic electrical constraint. No specific restrictions were placed on the Debye length or surface charge densities. However, to avoid situations where electrostatic interactions would promote macromolecule adsorption, results were obtained only for particles and pores of like charge.

3.2.2 Momentum equation

Although osmotic flow in a pore is not precisely unidirectional, the lubrication approximation is applicable, as detailed in Anderson and Malone (Anderson and Malone 1974). Accordingly, it was assumed that the axial (z) momentum balance is given by

$$\frac{\mu}{r}\frac{\partial}{\partial r}\left(r\frac{\partial v_z}{\partial r}\right)=\frac{\partial P}{\partial z}+\rho_e\frac{\partial \psi}{\partial z} \tag{3.2}$$

where $v_z(r, z)$ is the axial velocity component, μ is the viscosity, ρ_e is the volumetric charge density, and ψ is the electrical potential. At a fixed location in a pore, momentum transfer will be time-dependent, according to whether or not a particle (macromolecule) happens to be in the vicinity. Thus, each of the field variables (P, $\mathbf{v}$, ψ) is interpreted here as a time-averaged quantity.

The last term on the right side of equation (3.2) is the body force resulting from the streaming potential. Convection of counterions in a charged pore tends to generate a current, but in the absence of working electrodes, the net current must be zero. Accordingly, a potential gradient (streaming potential) must develop, such that the total

current due to ion migration balances that due to convection. In small, highly charged pores, the electrical body force might be significant, both in retarding the flow and in altering the shape of the velocity profile. Implicit in equation (3.1) is that the velocity profile is parabolic, as in an uncharged system.

In equation (3.2) it is assumed that the concentration of macromolecules is small enough that they do not influence the viscosity or otherwise affect the time-averaged axial momentum balance. In calculating ρ_e we assumed that the contribution of the macromolecule is negligible. In other words, the electrical body force was based on the concentrations only of the small ions. Likewise, it was assumed that the macromolecules have a negligible effect on the time-averaged concentrations of the small ions and the associated electric field. For a long pore, the electrical potential will then be of the form

$$\psi(r,z) = \psi_1(r) + \psi_2(z) \tag{3.3}$$

where $\psi_1(r)$ is the equilibrium double-layer potential and $\psi_2(z)$ arises from the streaming potential. The evaluation of these potentials will be discussed shortly.

3.2.3 Pressure distribution

Although osmotic flow in a pore is not precisely unidirectional, the lubrication approximation is applicable, as detailed in Anderson and Malone (Anderson and Malone 1974). Accordingly, it was assumed that the axial (z) momentum balance is given by

$$\frac{\mu}{r}\frac{\partial}{\partial r}\left(r\frac{\partial v_z}{\partial r}\right) = \frac{\partial P}{\partial z} + \rho_e \frac{\partial \psi}{\partial z} \tag{3.4}$$

where $v_z(r, z)$ is the axial velocity component, μ is the viscosity, ρ_e is the volumetric charge density, and ψ is the electrical potential. At a fixed location in a pore, momentum transfer will be time-dependent, according to whether or not a particle (macromolecule) happens to be in the vicinity. Thus, each of the field variables (P, $\mathbf{v}$, ψ) is interpreted here as a time-averaged quantity.

The last term on the right side of equation (3.4) is the body force resulting from the streaming potential. Convection of counterions in a charged pore tends to generate a current, but in the absence of working electrodes, the net current must be zero. Accordingly, a potential gradient (streaming potential) must develop, such that the total current due to ion migration balances that due to convection. In small, highly charged pores, the electrical body force might be significant, both in retarding the flow and in altering the shape of the velocity profile. Implicit in equation (3.1) is that the velocity profile is parabolic, as in an uncharged system.

In equation (3.4) it is assumed that the concentration of macromolecules is small enough that they do not influence the viscosity or otherwise affect the time-averaged axial momentum balance. In calculating ρ_e we assumed that the contribution of the macromolecule is negligible. In other words, the electrical body force was based on the concentrations only of the small ions. Likewise, it was assumed that the macromolecules have a negligible effect on the time-averaged concentrations of the small ions and the associated electric field. For a long pore, the electrical potential will then be of the form

$$\psi(r,z) = \psi_1(r) + \psi_2(z) \tag{3.5}$$

where $\psi_1(r)$ is the equilibrium double-layer potential and $\psi_2(z)$ arises from the streaming potential. The evaluation of these potentials will be discussed shortly.

3.2.4 Concentration of small ions

The concentrations of the monovalent cation and anion are related to the equilibrium double-layer potential by

$$c_{\pm}(\beta) = c_{\infty} \exp\left[\mp \Psi(\beta)\right] \tag{3.6}$$

where $\Psi = \psi_1 F / RT$ is the dimensionless potential and c_{∞} is the salt concentration in either bulk solution. Thus, the volumetric charge density is

$$\rho_e = F\left(c_+ - c_-\right) = -2Fc_{\infty} \sinh \Psi \tag{3.7}$$

where F is Faraday's constant. Combining this with Poisson's equation yields the cylindrical Poisson-Boltzmann equation,

$$\frac{1}{\beta}\frac{d}{d\beta}\left(\beta \frac{d\Psi}{d\beta}\right) = \tau^2 \sinh \Psi \quad . \tag{3.8}$$

The parameter τ, which is the pore radius divided by the Debye length, is given by

$$\tau = b\left(\frac{2F^2 c_{\infty}}{\varepsilon RT}\right)^{1/2} \tag{3.9}$$

for monovalent ions, where ε is the dielectric permittivity. The boundary conditions, corresponding to cylindrical symmetry at the pore centerline and constant charge density at the pore surface, were

$$\frac{\partial \Psi}{\partial \beta}(0) = 0 \tag{3.10}$$

$$\frac{\partial \Psi}{\partial \beta}(1) = q_c \tag{3.11}$$

where q_c is the dimensionless surface charge density at the cylindrical pore wall. It is related to the dimensional charge density Q_c (C/m^2) as

$$q_c = \frac{Q_c bF}{\varepsilon RT} . \tag{3.12}$$

The nonlinear boundary value problem for Ψ was solved numerically using COMSOL Multiphysics™ (COMSOL, Stockholm, Sweden), a finite element package.

3.2.5 Macromolecule concentration

As discussed in, for long pores the macromolecule concentration is a separable function, such that (Deen 1987)

$$C(\beta,z) = f(z)g(\beta) = f(z)\exp\left[-E(\beta)/kT\right] \tag{3.13}$$

Steric exclusion from the vicinity of the pore wall was modeled by setting $E = \infty$ there, so that $C = 0$ for $\beta > 1 - \lambda$. To calculate the osmotic reflection coefficient it is unnecessary to evaluate $f(z)$. As will be seen, it is sufficient to require that $f(0) - f(L) = C_1 - C_2 = \Delta C$, where C_1 and C_2 are the external concentrations at the two sides of the membrane.

3.2.6 Velocity profile

Because of the discontinuity in C at $\beta = 1 - \lambda$, equation (3.2) was integrated separately for $0 \le \beta < 1 - \lambda$ (the "core" region, where $v_z \equiv u$) and $1 - \lambda < \beta \le 1$ (the "periphery," where $v_z \equiv w$). With pressures and concentrations evaluated as just described, the differential equation for the core was

$$\frac{1}{\beta}\frac{\partial}{\partial\beta}\left(\beta\frac{\partial u}{\partial\beta}\right) = \frac{b^2}{\mu}\left[\frac{dP_0}{dz} + RT\frac{df}{dz}\left(g(\beta) - g(0)\right)\right] - \frac{2b^2RTc_\infty\Lambda}{\mu L}\sinh\Psi \tag{3.14}$$

where $\Lambda = (LF/RT)d\psi_2/dz$ is the dimensionless streaming potential. Integrating once, and applying the symmetry condition at $\beta = 0$, gave

$$\beta\frac{\partial u}{\partial \beta}=\frac{b^2}{2\mu}\left[\frac{dP_0}{dz}-RT\frac{df}{dz}g(0)\right]\beta^2+\frac{b^2RT}{\mu}\frac{df}{dz}\int_0^{\beta}xg(x)dx-\frac{2b^2RTc_{\infty}\Lambda}{\mu L}\int_0^{\beta}x\sinh\Psi dx\,. \tag{3.15}$$

The differential equation for the periphery was the same as equation (3.14), except without the g(β) term. A first integration there yielded

$$\beta\frac{\partial w}{\partial \beta}=\frac{b^2}{2\mu}\left[\frac{dP_0}{dz}-RT\frac{df}{dz}g(0)\right]\beta^2+\frac{b^2RT}{\mu}\frac{df}{dz}\int_0^{1-\lambda}xg(x)dx-\frac{2b^2RTc_{\infty}\Lambda}{\mu L}\int_0^{\beta}x\sinh\Psi dx \tag{3.16}$$

where equation (3.15) was used to ensure that the shear stress was continuous at $\beta = 1 - \lambda$.

A second integration for the periphery, and application of the no-slip condition at the wall, gave the final expression for the velocity in that region:

$$\begin{aligned}w(\beta,z)=&-\frac{b^2}{4\mu}\left[\frac{dP_0}{dz}-RT\frac{df}{dz}g(0)\right]\left(1-\beta^2\right)+\frac{b^2RT}{\mu}\frac{df}{dz}\ln\beta\int_0^{1-\lambda}xg(x)dx\\&+\frac{2b^2RTc_{\infty}\Lambda}{\mu L}\int_{\beta}^{1}\frac{dy}{y}\int_0^{y}x\sinh\Psi dx\end{aligned} \tag{3.17}$$

Another integration for the core, together with matching of the velocities at $\beta = 1 - \lambda$, completed the solution for the velocity profile:

$$\begin{aligned}u(\beta,z)=&-\frac{b^2}{4\mu}\left[\frac{dP_0}{dz}-RT\frac{df}{dz}g(0)\right]\left(1-\beta^2\right)+\frac{b^2RT}{\mu}\frac{df}{dz}\ln(1-\lambda)\int_0^{1-\lambda}xg(x)dx\\&-\frac{b^2RT}{\mu}\frac{df}{dz}\int_{\beta}^{1-\lambda}\frac{dy}{y}\int_0^{y}xg(x)dx+\frac{2b^2RTc_{\infty}\Lambda}{\mu L}\int_{\beta}^{1}\frac{dy}{y}\int_0^{y}x\sinh\Psi dx\end{aligned} \tag{3.18}$$

The first integral in both equations (3.17) and (3.18) is proportional to the equilibrium partition coefficent (Φ) for the macromolecule, which is the average intrapore concentration divided by that in bulk solution (at equilbrium). That is,

$$\Phi = 2\int_0^{1-\lambda} xg(x)dx \quad . \tag{3.19}$$

This and the other integrals were evaluated numerically, using a shape-preserving spline interpolation to approximate the integrands. After the integrands were tabulated, the Matlab function "Fit" was employed, using the "spline interpolant" option. The integration was done then using Simpson's Rule, typically with 100 intervals. The method was tested using polynomials which had functional shapes similar to those in either the single or double integrals of interest, and which could be integrated analytically. The numerical and analytical results agreed to within 1% for these test cases.

To calculate the osmotic reflection coefficient, the velocity was integrated piecewise over β to find the mean velocity (U), which is independent of z. This integration was done numerically, as just described. The result obtained for U was a linear function of the gradients dP_0/dz and df/dz. Integration over the pore length then produced a relationship of the same form as equation (1.1), permitting identification of σ_o. The changes in P_o and f over the pore length were related to the external pressure differences (ΔP and $\Delta\Pi$) by

$$P_0(0) - P_0(L) = \Delta P - \Delta\Pi\left[1 - g(0)\right] \tag{3.20}$$

$$RT\left[f(0) - f(L)\right] = \Delta\Pi \,. \tag{3.21}$$

Remaining to be discussed are the one unknown constant that appears in equations (3.17) and (3.18) (namely, Λ) and the one unknown function [$g(\beta)$].

3.2.7 Streaming potential

The streaming potential (Λ) was determined from the requirement that there be no net current. In the absence of axial variations in the concentrations of the small ions, and neglecting the current carried by the macromolecule, the axial component of the current density was given by

$$i_z = F\left[v_z \left(c_+ - c_-\right) - \left(D_+ c_+ + D_- c_-\right)\Lambda \right] \tag{3.22}$$

where $D_\pm$ are the cation and anion diffusivities. It is seen from equations (3.17) and (3.18) that the axial velocity is of the form $v_z = G\Lambda + H$, where the function H differs somewhat between the core and periphery but G is the same for both regions. Evaluating the concentrations using equation (3.6), and assuming (for simpeicity) that $D_+ = D_- = D$, it was found that

$$-\frac{i_z}{2Fc_\infty} = \left(G\sinh\Psi + \frac{D}{L}\cosh\Psi \right)\Lambda + H\sinh\Psi \quad . \tag{3.23}$$

Integrating Equation (23) over radial postion, zero current requires that

$$\Lambda = -\frac{\int_0^1 H\sinh\Psi \; \beta \, \mathrm{d}\beta}{\int_0^1 \left[G\sinh\Psi + \left(D/L\right)\cosh\Psi \right] \beta \, \mathrm{d}\beta} \quad . \tag{3.24}$$

Again, the integrals were evaluated numerically.

3.2.8 Electrostatic potential energy

The energy $E(\beta)$ was needed to compute the function $g(\beta)$ via equation (3.13). This is the electrostatic free energy associated with moving a charged sphere from bulk solution to a specified radial postion in a pore, and its evaluation required that the

equilibrium electrical potential Ψ be determined for three situations: (i) a sphere in an unbounded solution, (ii) a pore with no sphere, and (iii) a pore with sphere present. The desired potential energy change is the electrostatic energy for system (iii) minus the sum of those for (i) and (ii). In each case Ψ was assumed to be governed by the nonlinear form of the Poisson-Boltzmann equation,

$$\nabla^2\Psi = \tau^2 \sinh\Psi \tag{3.25}$$

where ∇^2 is the dimensionless Laplacian operator, spherical-radial for system (i), cylindrical-radial for (ii) [as in equation (3.8)], and three-dimensional for (iii). For (ii) and (iii) the parameter τ was given by equation (3.9); for (i), where the sphere radius was the only geometric length scale, τ was replaced by $\tau\lambda$. In (ii) and (iii) the surface charge density on the pore wall was specified by equation (3.11). For (i) and (iii) the surface charge density on the sphere was fixed. For the combined system, the dimensionless charge density for the sphere was expressed as

$$q_s = \frac{Q_s bF}{\varepsilon RT} \tag{3.26}$$

which is analogous to equation (3.12). For each of the three problems, Ψ was determined numerically using COMSOL, for various combinations of τ, λ, q_c, and q_s.

Following Sharp and Honig and Reiner and Radke, the electrostatic energy for each of the three systems was computed as

$$E_i = \int_{S_i} Q\psi dS - \int_{V_i} \left[\left(\varepsilon/2\right)\left|\nabla\psi\right|^2 + 2RTc_\infty\left(\cosh\Psi - 1\right)\right] dV \tag{3.27}$$

where i = s, c, and sc for the isolated sphere, isolated pore, and combined system, respectively (Sharp and Honig 1991, Reiner and Radke 1991). Recall that Q and ψ are

the dimensional charge density and potential, respectively, whereas Ψ is dimensionless. The surface integration encompasses all charged surfaces (sphere surface and/or pore wall) and the volume integration is over the entire solution volume. The energy change was calculated as

$$E = E_{sc} - E_s - E_c \tag{3.28}$$

Although the pore was assumed to be indefinitely long, making each of the integrals in E_{sc} and E_c divergent, the difference $E_{sc} - E_c$ was made finite by the fact that ψ is the same for both systems as $z \to \pm \infty$. For the isolated sphere, convergence was ensured by the fact that the integrand in the volume integral vanishes as $r \to \infty$.

If the potentials are small enough that $\sinh\Psi \cong \Psi$ (which is accurate to within 18% for $|\Psi| = 1$), then equation (3.25) takes the linear form,

$$\nabla^2\Psi = \tau^2\Psi \tag{3.29}$$

which has been solved analytically for the geometry and boundary conditions of interest here (Deen 1982). When this linearized form of the Poisson-Boltzmann equation is applicable, the electrostatic energy simplifies to

$$E_i = \frac{1}{2}\int_{S_i} Q\psi dS \tag{3.30}$$

as given in Verwey and Overbeek (Verwey and Overbeek 1948). The results for E calculated previously for the linear problem will be compared with those obtained from the nonlinear formulation. The analytical evaluation of E is detailed in the Appendix. Also discussed there are certain simplifications that occur in the calculation of σ_o when equation (3.29) is applicable.

3.2.9 Parameters

As seen in equations (3.17) and (3.18), the velocity profile for osmotic flow will depend on λ (sphere radius/pore radius) and the dimensionless parameters that influence the equilibrium potential (Ψ), which are τ [pore radius/Debye length, Equation (10)] and q_c [dimensionless pore charge, equation (3.13)]. Also involved, via the function $g(\beta)$, are the parameters that determine the dimensionless potential energy for the macromolecule, E/kT. In addition to λ, τ, and q_c, those are q_s [dimensionless sphere charge, equation (3.26)] and

$$\xi = \frac{(R_g T / F)^2 \varepsilon b}{kT} \tag{3.31}$$

which arises when E is made dimensionless using the thermal energy. Finally, there are the parameters that determine the streaming potential (Λ). From equation (3.24), it is found that the determinants of Λ are those for the potential energy (λ, τ, q_c, q_s, ξ) plus

$$\chi = \frac{\mu D}{b^2 R_g T c_\infty} \tag{3.32}$$

and two pressure ratios, $\Delta P/(R_g T c_\infty)$ and $\Delta \Pi/(R_g T c_\infty)$. However, substituting the expression for the streaming potential into the velocity profile reveals that these pressure ratios do not influence the reflection coefficient. In summary, we conclude from dimensional analysis that

$$\sigma_o = \sigma_o\left(\lambda, \tau, q_c, q_s, \xi, \chi\right) . \tag{3.33}$$

In computing reflection coefficients we viewed the sphere radius, sphere and pore surface charge densities, and bulk salt concentration as the primary variables. Unless otherwise noted, the results correspond to aqueous KCl solutions at 25°C ($D_+ = D_- = 2.0 \times$

10^{-9} m^2/s and $\mu = 8.9 \times 10^{-4}$ Pa·s) and a pore radius of $b = 10$ nm. The corresponding value of the energy-scale parameter is $\xi = 1.1$. For these reference conditions and $c_\infty = 1$ M, the diffusivity-viscosity parameter is $\chi = 7.2 \times 10^{-3}$. At the default pore radius of 10 nm, $\tau = 0.1$, 1, and 10 correspond to $c_\infty = 9 \times 10^{-6}$, 9×10^{-4}, and 9×10^{-2} M, respectively. At that pore radius, $q_c = q_s = 1$ corresponds to $Q_c = Q_s = 1.8 \times 10^{-3}$ C/m^2. For BSA, where $a = 3.6$ nm, $q_s = -11$ if $b = 10$ nm and the net charge is -20. At the default pore radius, $\lambda = 0.36$ for BSA.

3.3 RESULTS

3.3.1 Electrostatic potential energy

A key quantity both in equation (3.1) and in the more general formulation is the potential energy (E) for a sphere whose center is located at a given radial position within a pore. The corresponding Boltzmann factor [$\exp(-E/kT)$] is the probability that a given sphere will occupy that position. Because it determines the extent to which a particle will be excluded from a pore, the Boltzmann factor strongly influences the osmotic reflection coefficient. In preliminary calculations we addressed the issue of whether numerical solutions of the nonlinear Poisson-Boltzmann equation were necessary to obtain sufficiently accurate values of E at the high charge densities of interest, or whether previously reported analytical results based on the linearized Poisson-Boltzmann equation were adequate. As shown in Figure 3.1, Boltzmann factors obtained from the nonlinear and linear formulations were found to be nearly identical, even for maximum values of $|\Psi|$ exceeding unity. Evidently, the tendency of the linear formulation to overestimate the surface potential for a given system, and therefore overestimate E_i, was

largely offset by the fact that E is a difference between electrostatic energies [equation (3.28)]. We conclude that the analytical results for E, which are much easier to use, are sufficiently accurate for calculations of σ_o. All of the results to be presented for σ_o are based on the linear formulation for E.

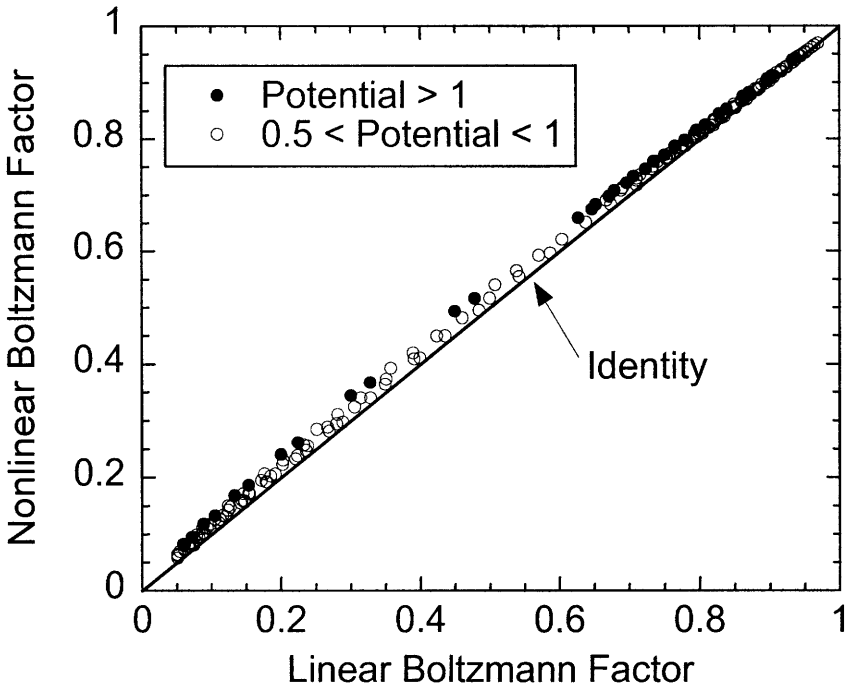

Figure 3.1 Comparison of Boltzmann factors [exp(-E/kT)] calculated using equations (3.25) and (3.27) ("Nonlinear") or equations (3.29) and (3.30) ("Linear"). The nonlinear results were obtained from finite element calculations for spheres positioned on the pore axis, and the linear results for this axisymmetric case were computed from a previous analytical solution (Smith and Deen 1982). A variety of combinations of λ, τ, q_s, and q_c were used, resulting in maximum equilibrium potentials ($|\Psi_{max}|$) in one of two ranges, $0.5 < |\Psi_{max}| < 1$ or $|\Psi_{max}| > 1$. For $|\Psi_{max}| < 0.5$ (not shown), there was no noticeable difference between the linear and nonlinear Boltzmann factors.

3.3.2 Streaming potential

The streaming potential, which retards transmembrane flow and which may also alter the shape of the velocity profile in a pore, is a linear function of the external pressure differences. This relationship was expressed as

$$\Lambda = A\frac{\Delta P}{RTc_\infty} - B\frac{\Delta \Pi}{RTc_\infty} \tag{3.34}$$

where A and B are dimensionless coefficients. The sign of each coefficient is opposite to that of the fixed charge (e.g., both are > 0 if $q_c < 0$), but the magnitudes of A and B are the same for positively or negatively charged pores. The dependence of $|A|$ and $|B|$ on τ (pore radius/Debye length) is shown in Figure 3.2. Under the conditions chosen both coefficients had peak magnitudes of about 1.7×10^{-3} at $\tau = 4$. Because charge effects are suppressed when double layers are thin relative to the pore radius, A and B each must vanish as $\tau \to \infty$, consistent with the plot. Both coefficients also must vanish for large Debye lengths, or $\tau \to 0$, although the magnitude of Λ reaches a maximum, constant value in that limit. Because c_∞ appears in the denominators in equation (3.34), and because $\tau \propto c_\infty^{1/2}$, constancy of Λ requires that A and B each vary as τ^2 for $\tau \to 0$, as shown in Figure 3.2.

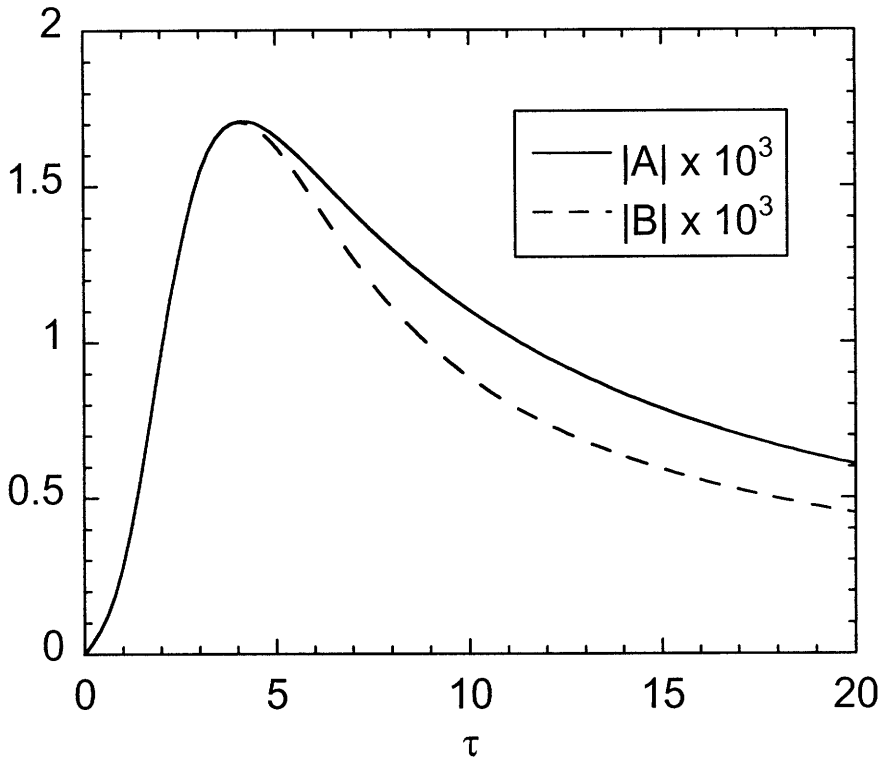

Figure 3.2 Effect of τ (pore radius/Debye length) on the streaming potential. The coefficients A and B, defined in equation (3.34), describe the effects of transmembrane mechanical and osmotic pressure differences, respectively. Note that all values have been multiplied by10^3. It was assumed here that $\lambda = 0.5$ and $q_s = q_c = 4$.

The retardation of transmembrane flow by the streaming potential is illlustrated in Figure 3.3, in which the apparent hydraulic permeability for charged pores, relative to that for uncharged pores of the same size, is shown as a function of τ for three values of q_c. The apparent hydraulic permeability was always reduced to some extent. This effect was minimal at small Debye lengths (large τ) and/or low membrane charge densities (q_c),

but was quite noticeable when the Debye length and/or charge density were large. For the parameter values in Figure 3.3, there was a 13% reduction in κ for $q_c = 4$ and $\tau \to 0$.

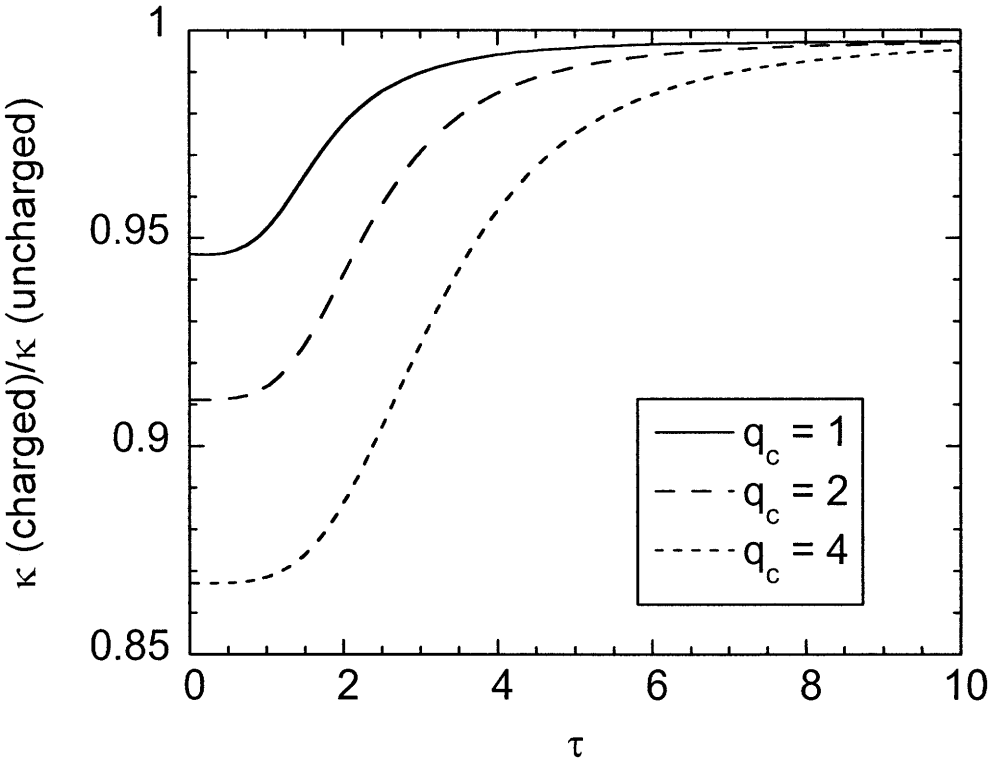

Figure 3.3 Effect of τ (pore radius/Debye length) and pore charge density (q_c) on the hydraulic permeability (κ) defined in equation (1.1). The hydraulic permeabilty for charged pores is compared with that for neutral pores of the same size.

3.3.3 Osmotic reflection coefficient

The effects of molecular size and charge on the osmotic reflection coefficient are shown in Figure 3.4, where σ_o is plotted as a function of λ (sphere radius/pore radius) for several charge densities. In this plot the sphere and pore were assumed to have equal charge densities ($q_c = q_s = q$) and the relative Debye length was fixed ($\tau = 5$). As

expected, higher charge densities increased σ_o. This is because they elevated E and therefore tended to exclude particles from the pore.

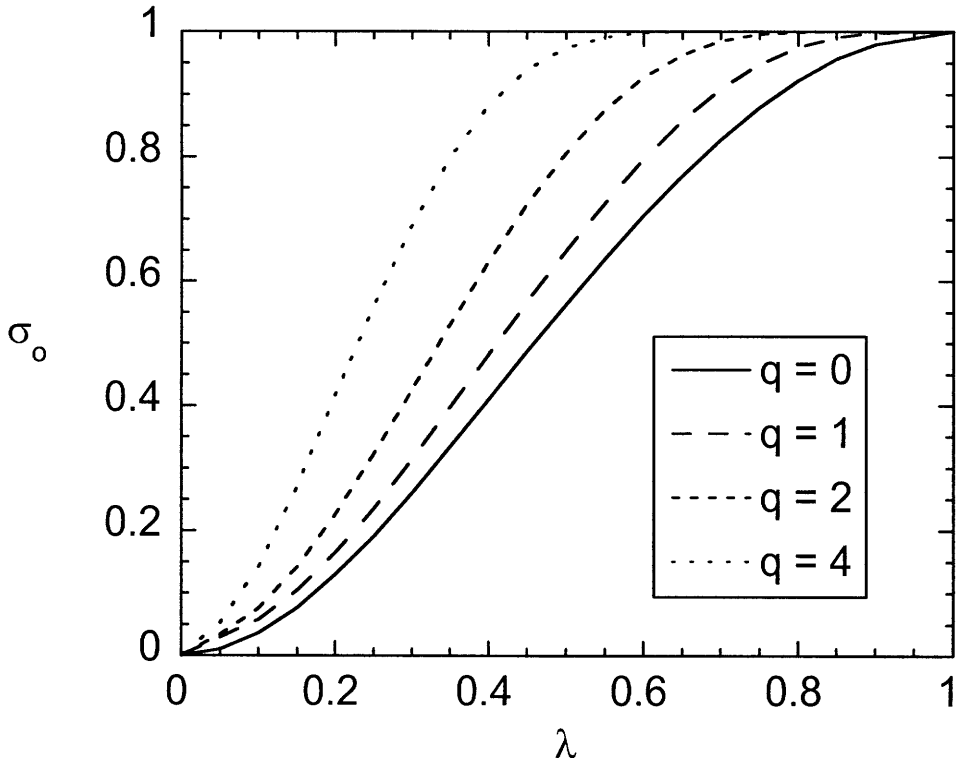

Figure 3.4 Effect of relative sphere size (λ = sphere radius/pore radius) and sphere and pore charge density ($q = q_s = q_c$) on the osmotic reflection coefficient (σ_o). It was assumed here that $\tau = 5$.

Figure 3.5 shows the osmotic reflection coefficient as a function of solute size for various Debye lengths, with charge densities fixed. The effects of decreasing the Debye length (increasing τ) were qualitatively similar to those of decreasing q. The curve labeled "$\tau = \infty$" is that for an uncharged sphere and pore (Anderson and Malone 1974).

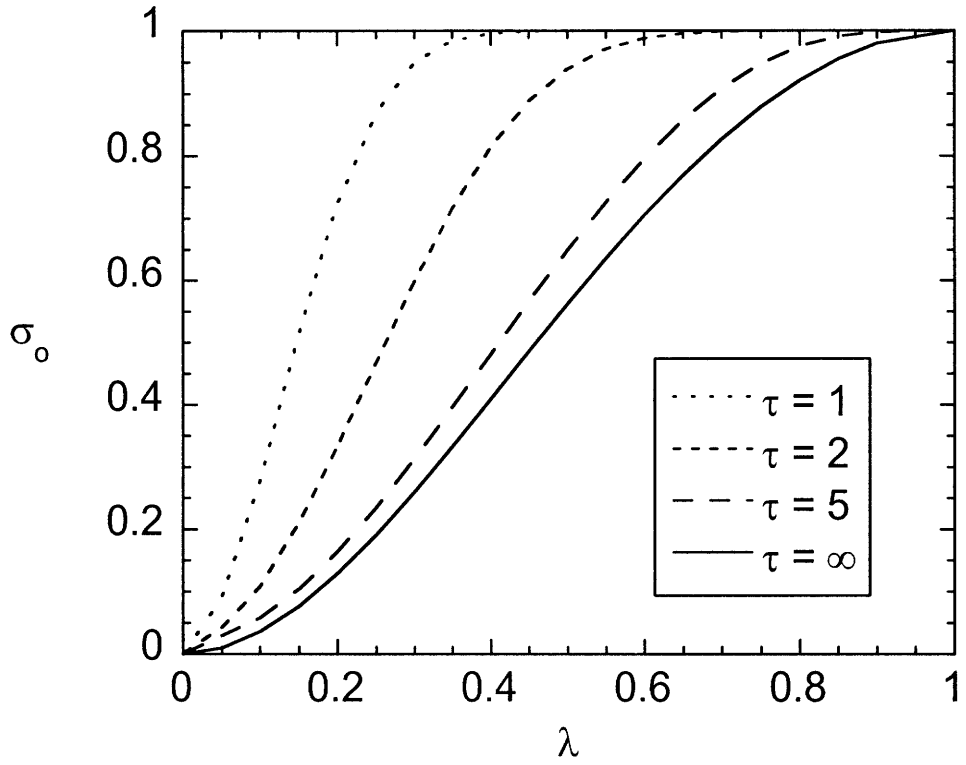

Figure 3.5 Effect of λ (sphere radius/pore radius) and τ (pore radius/Debye length) on the osmotic reflection coefficient (σ_o). It was assumed here that $q_s = q_c = 1$.

Figure 3.6 provides another view of the effects of charge on σ_o. Here the relative sphere size was fixed ($\lambda = 0.5$) and the Debye length and charge densities were varied. As with the two preceding plots, it was assumed that $q_s = q_c = q$. Once again, large τ and/or small q yielded reflection coefficients that approached those for an uncharged system ($\sigma_o = 0.56$). However, even for a modest charge density ($q = 0.5$), σ_o was increased to unity if the Debye length was large enough (τ small enough).

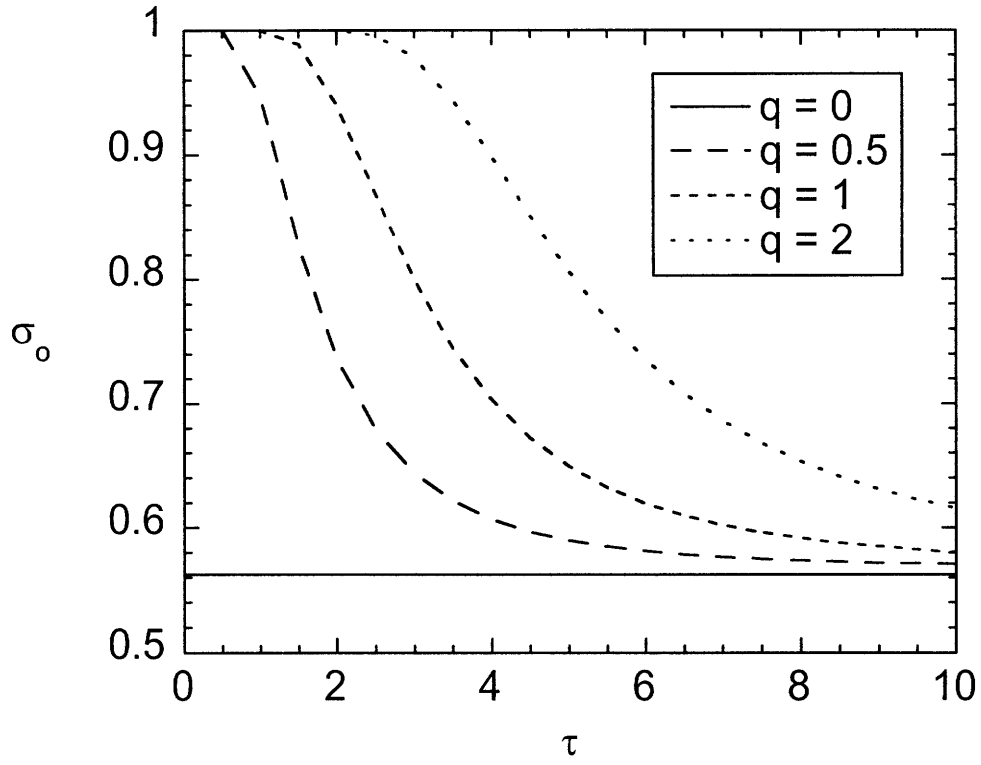

Figure 3.6 Effect of τ (pore radius/Debye length) and charge density ($q = q_s = q_c$) on the osmotic reflection coefficient (σ_o) for $\lambda = 0.5$.

Of course, solute and pore charge densities generally will be unequal. Figure 3.7 shows the effects of sphere charge density (q_s) on σ_o for several values of the pore charge density (q_c). In these calculations the relative sphere size and Debye length were each fixed ($\lambda = 0.5$ and $\tau = 5$). As expected for a system with like charges and repulsive electrostatic interactions, σ_o was elevated by increases in either charge density. It is

noteworthy that even for an uncharged sphere ($q_s = 0$), σ_o increased noticeably as the pore charge density was increased (from 0.56 at $q_c = 0$ to 0.64 at $q_c = 4$). Likewise, there were electrostatic effects for a charged sphere in an uncharged pore, as shown by the bottom curve in Figure 3.7. This occurs because placing an uncharged sphere in a pore distorts the equilibrium double layer in the pore, and therefore gives a nonzero electrostatic contribution to the potential energy ($E > 0$, irrespective of the sign of the pore charge) (Deen 1982). Similarly, confining a charged sphere in an uncharged pore distorts the sphere double layer.

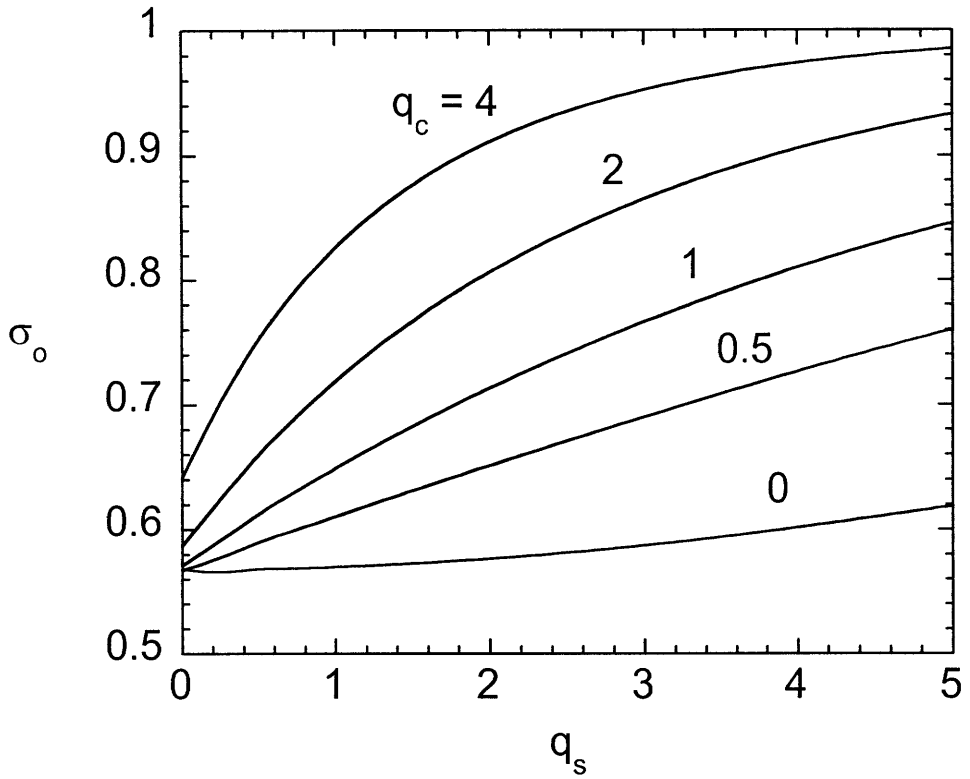

Figure 3.7 Effect of sphere charge (q_s) and pore charge (q_c) on the osmotic reflection coefficient (σ_o) for λ = 0.5 and τ = 5.

Surprisingly, given the ability of the streaming potential to influence the hydraulic permeability (Figure 3.3), the electrokinetic effect on σ_o was found to be negligible for all realistic combinations of parameters that we examined. That is, the results computed with the general formulation were never significantly different than those from equation (3.1). This finding is discussed further in the next section.

3.4 CONCLUSION

A model was developed to predict the effects of solute and pore charge on the osmotic reflection coefficients of spherical macromolecules, combining low Reynolds number hydrodynamics with a continuum description of the electrical double layers. As expected, for molecules and pores of like charge, σ_o always exceeded that for an uncharged system with the same solute and pore size. The effects of charge were found to stem almost entirely from electrostatic exclusion of the macromolecules from the pores. For like charges and constant surface charge densities, particle positions within a pore are energetically unfavorable, which decreases the equilibrium partition coefficient, Φ (Deen 1982). As recognized previously, decreases in Φ lead to increases in σ_o (Anderson and Malone 1974, Anderson 1981, Bhalla and Deen 2007). In terms of the ability to induce an osmotic flow, adding like charges to the macromolecules and pore walls is qualitatively similar to increasing the macromolecular radius. That is, it leads to behavior more closely resembling an ideal, semipermeable membrane, where σ_o = 1. However, one cannot account for charge by, say, simply adding a Debye length to the particle radius. This is because the strength of the electrostatic interactions depends on the surface charge densities, and not just the geometric dimensions and Debye length.

The relationship between osmosis and partitioning is examined more quantitatively in Figure 3.8, in which σ_o is plotted as a function of Φ. The discrete symbols are numerical results obtained for various combinations of λ, τ, q_s, and q_c. A strong correlation is evident, σ_o decreasing as Φ increases. The curve corresponds to

$$\sigma_o = (1-\Phi)^2 \tag{3.35}$$

which was derived originally for uncharged spheres in uncharged cylindrical pores and shown to be nearly exact also for uncharged spheroids (oblate or prolate) in such pores (Anderson and Malone 1974, Bhalla and Deen 2007). It is seen that equation (3.35) was accurate for charged spheres in many instances, but significantly underestimated σ_o in others. Overall, it appears that equation (3.35) is somewhat less reliable for charged than for uncharged systems. It should be mentioned also that it is restricted to cylindrical pores; for example, results obtained for neutral spheroids in slit pores followed a somewhat different relationship (Bhalla and Deen 2007).

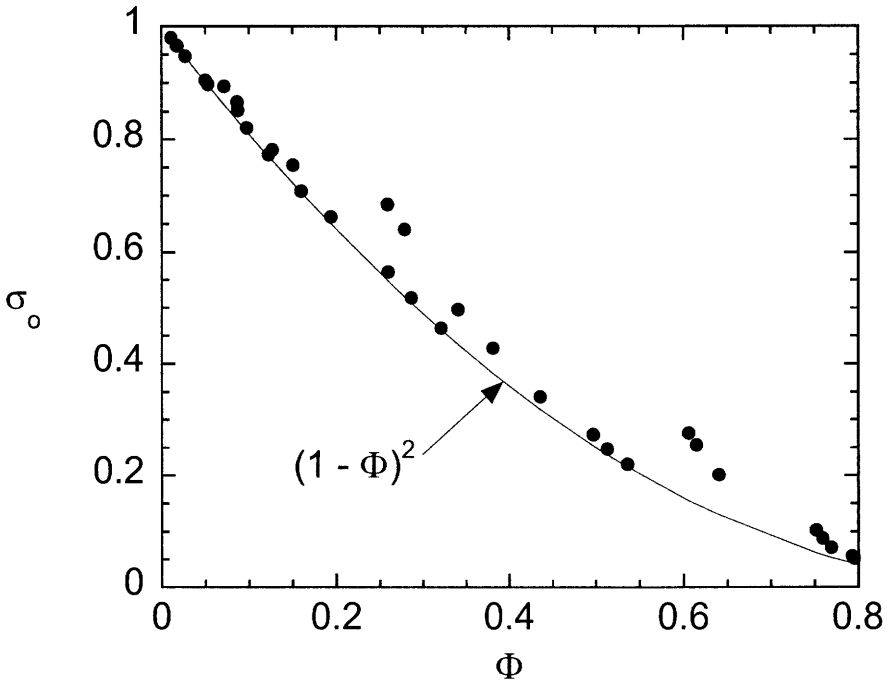

Fig. 3.8 Relationship between the osmotic reflection coefficient (σ_o) and equilibrium partition coefficient (Φ). The symbols represent numerical results obtained for various combinations of sphere size, Debye length, and sphere and pore charge densities. The curve, from equation (3.35), is a prediction for uncharged spheres in uncharged cylindrical pores.

In principle, the effects of charge on σ_o might be mediated in part by an electrokinetic effect. It is well known that pressure-driven flow through a small, charged pore, under open-circuit conditions, creates an axial variation in electrical potential (Newman 1973). This is termed the streaming potential, and it arises because the fluid in the pore is not electrically neutral. Due to an excess of counterions in the mobile fluid, any bulk flow tends to create a current, which (under open-circuit conditions) must be balanced by ion migration. The resulting electrical body force tends to retard the flow and might alter the shape of the velocity profile. If the profile is distorted sufficiently from the parabolic shape characteristic of Poiseuille flow, then the value of σ_o may be altered (Anderson 1981). As streaming potentials had not been explored previously in this context, we sought to assess their importance. However, we found this effect on σ_o to be negligible. This was true for a wide variety of parameter combinations, including situations where the streaming potential was large enough to cause a very significant reduction in the mean velocity.

To see if there are any conditions in which the streaming potential might influence σ_o, we mapped out combinations of parameters for which the velocity profile in a pore without macromolecules was either parabolic or non-parabolic. For Poiseuille flow in a cylindrical pore, the centerline velocity is exactly twice the mean value. The electrokinetic effect (when present) reduces the ratio of local to mean velocity near the pore wall and increases it near the centerline. We defined a "non-parabolic" velocity profile as one in which the centerline ratio was altered by >5% (velocity ratio >2.1). The results of that exploration are shown in Figure 3.9, in which the curve corresponds to combinations of dimensionless pore charge density ($|q_c|$) and ratio of pore radius to

Debye length (τ) at which the velocity profile changed from parabolic to non-parabolic. For a given τ, non-parabolic profiles resulted for values of $|q_c|$ above the curve and parabolic ones for values below it. (Without macromolecules, the shape of the velocity profile can be influenced by one additional parameter, χ. However, with μD and T fixed, as assumed here, $\chi \propto 1/\tau^2$, so that χ is not independent.)

The results in Figure 3.9 indicate that non-parabolic profiles might indeed occur, especially if τ is small (Debye length exceeding pore radius) and pore charge density large. As a benchmark for surface charge density, if that for the pore were similar to that of BSA under physiological conditions ($Q_c = Q_s = -2.0 \times 10^{-2}$ C/m^2), then $|q_c| = 5.5$, 11, and 22 for $b = 5$, 10, and 20 nm respectively. Based on Fig. 8, non-parabolic profiles will result for $\tau < 2$ if $|q_c| = 20$. However, σ_o computed for such high pore charge densities usually did not differ significantly from unity. Although for relatively small molecules ($\lambda = 0.1$) we sometimes found $\sigma_o < 1$ under non-parabolic conditions, electrokinetic effects on σ_o were still insignificant. Thus, under conditions where the streaming potential most affects the apparent hydraulic permeability (small τ and large $|q_c|$, Figure 3.3), and where it would be expected to most affect σ_o, there was not a significant difference between the full model and equation (3.1). This was largely because the ideal semipermeable limit was predicted by each. In summary, we were unable to identify any realistic conditions for which equation (3.1) was inaccurate.

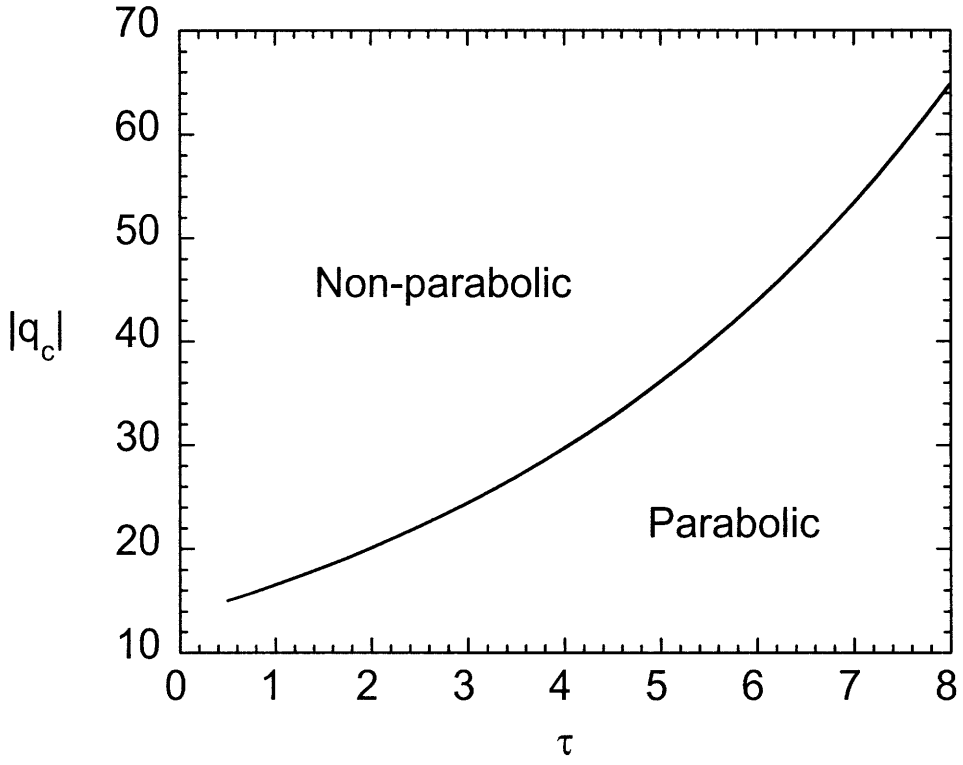

Figure 3.9 Combinations of dimensionless pore charge density (q_c) and ratio of pore radius to Debye length (τ) for which the velocity profile in a pore was predicted to be either parabolic or non-parabolic. A non-parabolic profile is defined here as one in which the ratio of centerline to mean velocity is >2.1.

Serum albumin is the predominant protein in blood plasma, and its loss from the circulation by permeation through capillary walls – especially in the kidney – is of considerable pathophysiological importance (Haraldsson and Nystrom 2008). In addition to being negatively charged, albumin is not precisely spherical, and it is often modeled as a prolate spheroid. Accordingly, one might ask whether the sieving of BSA through a

porous memberane is influenced more by its shape or its charge. A complete answer is not yet possible, but the present results concerning the effects of charge for spheres, together with previous predictions of the effects of shape for uncharged spheroids, permit some comparisons to be made. Because the reflection coefficient for filtration (σ_f) is nearly equal to that for osmotic flow (Anderson 1981, Bhalla and Deen 2007), it is permissible to draw conclusions about sieving from the results for σ_o. Figure 3.10 shows σ_o as a function of relative molecular size for three cases: an uncharged sphere and pore; a sphere and pore each with a charge density like that of BSA; and an uncharged prolate spheroid and uncharged pore. The abscissa (λ) in each case is the ratio of Stokes-Einstein radius to pore radius; with the Stokes-Einstein radius fixed at the value for BSA (3.6 nm), it is the pore radius (b) that was varied along each curve. Because the other dimensionless groups in the charge model (τ, q_c, q_s, ξ, χ) also contain b, they were varied along with λ in computing σ_o for that case. The axial ratio for the prolate spheroid was taken to be 3.4 (Vilker et al. 1981). Generally, σ_o for the charged sphere and uncharged prolate spheroid each exceeded that for the neutral sphere, by roughly similar amounts. There was an exception to this trend for very tightly fitting particles, where values of σ_o for prolate spheroids became slightly lower than those for uncharged spheres. This reflects the fact that the minor semiaxis of a prolate spheroid is less than its Stokes-Einstein radius (Bhalla and Deen 2007). Thus, if aligned properly, it will fit in a pore even if $\lambda > 1$. (For an axial ratio of 3.4, the theoretical cutoff for partitioning or sieving occurs at $\lambda = 1.7$.) The effects of charge depend, or course, on the charge density of the pore wall. Reducing Q_c to half the value for BSA gave a curve that overlapped with that for the prolate spheroid (results not shown). Overall, Figure 3.10 suggests that the effects

of molecular shape and charge on the sieving BSA are of roughly comparable importance.

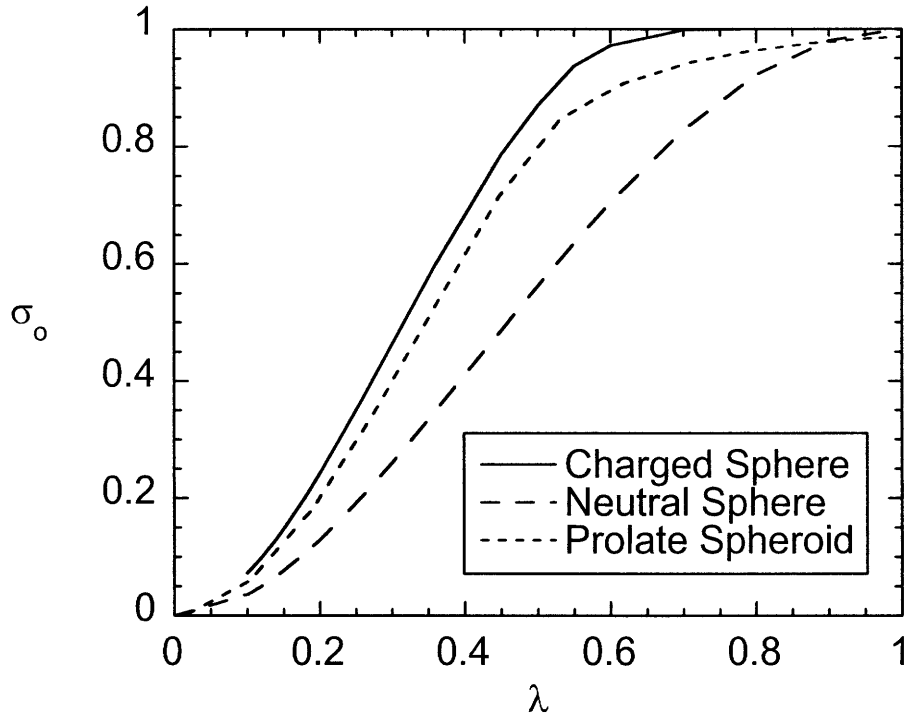

Figure 3.10 Predicted effects of molecular size, shape, and charge on the osmotic reflection coefficient (σ_o) for BSA. Results for an uncharged prolate spheroid in an uncharged pore and a charged sphere in a charged pore are compared with those for an uncharged sphere in an uncharged pore. In each case λ = Stokes-Einstein radius/pore radius. The calculations for the prolate spheroid were as described in Bhalla and Deen (Bhalla and Deen 2007). Based on data reviewed in Vilker et al. (Vilker et al. 1981), the major and minor semiaxes were taken to be 7.05 and 2.08 nm, respectively, corresponding to an axial ratio of 3.39 and a Stokes-Einstein radius of 3.56 nm. For the charged case, it was assumed that a = 3.6 nm, c_∞ = 0.15 M, and $Q_c = Q_s = -2.0 \times 10^{-2}$ C/m^2. The sphere charge density corresponds to 20 negative charges per molecule, which is representative of BSA under physiological conditions (Vilker et al. 1981).

A common measure of membrane selectivity in filtration processes is the sieving coefficient (Θ) for a given solute, which is its filtrate-to-retentate concentration ratio. If the Peclet number based on pore length is large and concentration polarization is negligible, then $\Theta = 1 - \sigma_f$. Because the hydrodynamic problem that must be solved to predict σ_o is much simpler than that needed to compute σ_f, osmotic flow calculations provide an attractive way to gain insight into filtration selectivity, provided that σ_o does not differ greatly from σ_f (Dechadilok and Deen 2006). A comparison of the two reflection coefficients for charged spheres and pores is shown in Figure 3.11. Results are shown for two charge densities, with those for the sphere and pore assumed to be equal in both cases ($q_s = q_c = q$). The values of σ_f were computed from

$$\sigma_f = 1 - 4\int_0^{1-\lambda} G e^{-E/kT}(1-\beta^2)\beta\, d\beta \tag{3.36}$$

which is the same as equation (3.1), but including now the lag coefficient (G) (Deen 1987). In the absence of values of G for charged particles in charged pores, results for uncharged systems were used (Dechadilok and Deen 2006). For both charge densities in Figure 3.11, σ_f slightly exceeded σ_o, the agreement improving somewhat as the charge density was increased from q = 1 to 4. We conclude that the approximate equality of σ_o and σ_f found previously for neutral spheres and pores continues to hold when electrostatic interactions are present (Anderson and Malone 1974, Bhalla and Deen 2007).

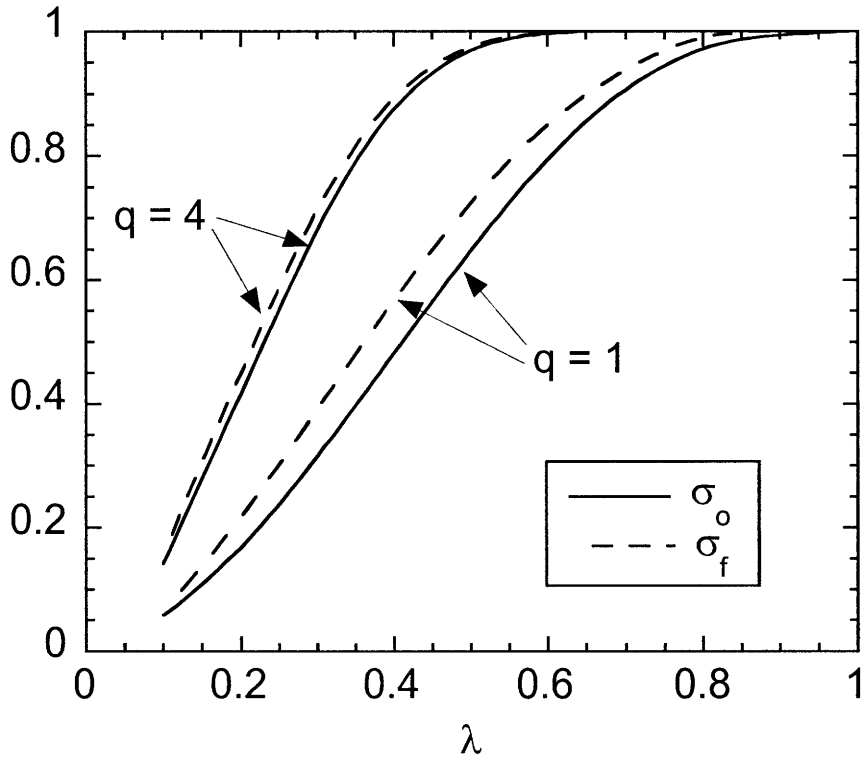

Figure 3.11 Reflection coefficients for osmosis (σ_o) and filtration (σ_f) as a function of relative sphere size (λ). Results are shown for two charge densities ($q = q_s = q_c = 1$ or 4), with $\tau = 5$ in each case.

The present approach could be used to analyze the effects of charge on σ_o in more complex geometries, such as a spherical macromolecule passing through an array of fibers. Because the hydrodynamic problem that must be solved to obtain σ_o is much simpler than that needed to compute σ_f (as reviewed in Dechadilok and Deen (Dechadilok and Deen 2006)), and because $\sigma_o \cong \sigma_f$, osmotic flow calculations provide an attractive way to gain insight into the selectivity of filtration processes. With the effects of the streaming potential on σ_o apparently negligible, efforts to extend the theory to

more complex geometries can focus largely on evaluating the corresponding electrostatic energies (E). Moreover, our finding that Boltzmann factors [$\exp(-E/kT)$] derived using the linear and nonlinear Poisson-Boltzmann equations were nearly identical suggests that linearization can be invoked to simplify the calculation of E for other systems. (This conclusion applies only to systems of like charge, where $E > 0$.) Electrostatic energies have been reported for a sphere interacting with a single cylindrical fiber (Johnson and Deen 1996); a task that remains for fiber arrays is to account for the simultaneous electrostatic interactions of a sphere with multiple fibers.

Once this is accomplished, the flow problem in such a geometry can be solved and the reflection coefficient determined. This is the topic of the next Chapter.

Chapter 4. EFFECTS OF CHARGE ON OSMOTIC REFLECTION COEFFICIENTS OF MARCOMOLECULES IN FIBROUS MEMBRANES

4.1 INTRODUCTION

Polymeric hydrogels containing networks of proteins, glycosaminoglycans (GAG), and other biopolymers, and consisting mostly of water, are present throughout the body. They may be viewed as arrays of fibers with fluid-filled interstices. The fibers may be single polymeric chains or multichain aggregates, and their arrangement may be highly ordered or relatively random. Examples of such fibrous materials include the glycocalyx coatings of cells, junctional complexes in endothelia and epithelia, basement membranes, and interstitial matrices. The resistances of fibrous materials to the transport of water and solutes impact numerous physiological functions, often controlling

microvascular and other permeability properties and generally affecting the extracellular movement of nutrients, cytokines, and therapeutic drugs. Often, the fibers have a net electrical charge. This Chapter deals with the physics of osmotic flow through such materials and, less directly, with the related subject of convective transport of macromolecules. In particular, we are interested in the effects of molecular charge, as well as molecular size, on osmosis and convection through thin barriers (membranes) consisting of fibrous hydrogels. Our focus is on macromolecular solutes (such as globular proteins) which are large enough and rigid enough to be viewed as hydrodynamic particles, with the objective being to provide numerical results of σ_o for charged spheres in membranes consisting of regular arrays of fibers of like charge. As in the analysis of Zhang et al. for neutral spheres and fibers, the flow was assumed to be parallel to the fiber axes (Zhang et al. 2006). An important subproblem that was confronted was how to estimate the change in electrostatic energy associated with placing a charged sphere inside an array of charged fibers of indefinite extent. This energy was evaluated using continuum double layer calculations for a sphere interacting with a single charged cylinder, together with a pairwise additivity approximation. Pairwise additivity of energies was tested using "exact" results generated for a sphere interacting with two cylinders, and found to work surprisingly well. The electrostatic energies were combined with a viscous flow model to compute σ_o as a function of the fiber volume fraction, fiber and sphere charge densities, and fiber and sphere size.

4.2 THEORY

4.2.1 Model geometry

Long fibers, aligned with the z axis, were assumed to be arranged on a periodic hexagonal lattice. Figure 4.1 shows a central fiber surrounded by an inner ring of six nearest neighbors and a second ring of twelve next-nearest neighbors. Certain symmetry planes are indicated by dashed lines. The hexagonal pattern was assumed to repeat indefinitely. Also shown (black circle) is a spherical macromolecule positioned within the inner ring. The flow was assumed to be normal to the plane of the figure (in the z direction).

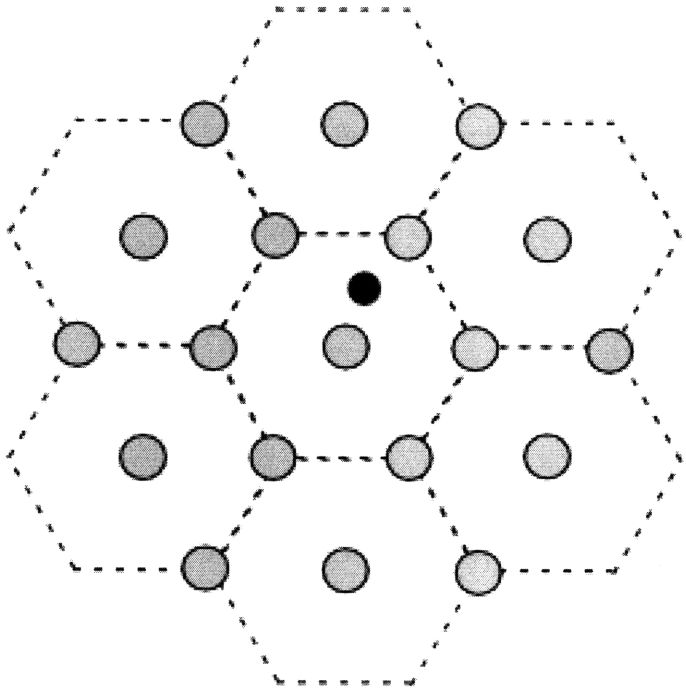

Figure 4.1 Parallel fibers arranged on a hexagonal lattice. The fibers are shaded in gray and certain symmetry planes are indicated by the dashed lines. A spherical macromolecule is shown in black near the central fiber.

Figure 4.2 is an enlargement of the region near the central fiber, with the key geometric parameters shown. The sphere radius is a, the fiber radius is b, and the surface-to-surface fiber separation is H. Cylindrical radial and angular coordinates, based on the central fiber, are r and θ. Because of the symmetry, it was sufficient to consider only $0 \leq \theta \leq \pi/6$. Following Happel and Zhang et al., the geometry was simplified to an annulus by replacing the hexagonal boundary by a circle of radius R (Happel 1959, Zhang et al. 2006). This "flow radius" was chosen to maintain the same open area per fiber. The relationship between R, b, and H is

$$R = \frac{3^{1/4}}{\sqrt{2\pi}}(2b + H) \tag{4.1}$$

The largest sphere that will fit anywhere within such an array has a radius

$$a_m = \frac{2b + H}{\sqrt{3}} - b \quad . \tag{4.2}$$

Thus, $\sigma_o = 1$ for $a \geq a_m$. A sphere with $H + b - R < a < a_m$ will fit at some positions, but will have its center limited to angular positions such that $0 \leq \theta \leq \theta_m$, where

$$\theta_m = \frac{\pi}{6} - \cos^{-1}\left[\frac{r^2 + (2b+H)^2 - (a+b)^2}{2r(2b+H)}\right] \tag{4.3}$$

This maximum angle is affected, of course, by the radial position of the sphere center (r). Smaller spheres ($a < H + b - R$) are restricted sterically only by the central fiber. To fit, their centers must be positioned at $r > a + b$.

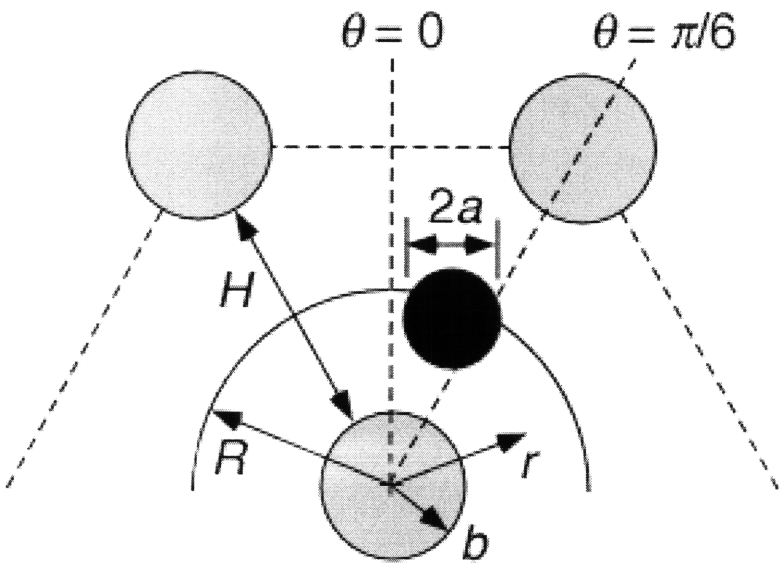

Figure 4.2 Enlargement of the hexagonal fiber lattice, showing a central fiber and two nearest neighbors (gray), a spherial macromolecule (black), local cylindrical coordinates, and key lengths. The surface $r = R$ is the outer boundary of the annular region used in the osmotic flow calculations, with R chosen to yield the same open area per fiber as in the hexagonal array.

4.2.2 Assumptions

The membrane thickness (L, also the fiber length) was assumed to greatly exceed R, which has two consequences. First, the resistances to water and solute transport across the interfaces at $z = 0$ and $z = L$ are negligible relative to those within the fiber matrix, allowing thermodynamic equilibrium to be assumed between the internal and external solutions at those boundaries. This is the usual assumption made in analyzing membrane transport processes. Second, the lubrication approximation can be applied to the equations of motion, as in the analogous problem involving long, cylindrical pores (Anderson and Malone 1974). This greatly simplifies the hydrodynamic problem, as will be seen.

The mobile macromolecules were modeled as spheres with a specified surface charge density; the surface charge density of the fibers was also constant. The electrolyte was assumed to consist of univalent anions and cations, each of negligible size relative to the macromolecule or fibers. The macromolecule solutions were assumed to be dilute enough to make solute-solute interactions negligible. The bulk electrolyte concentrations on the two sides of the membrane were assumed to be equal, so that osmosis results only from an imbalance in macromolecule concentrations. No restrictions were placed on the Debye length or surface charge densities, but to avoid situations where electrostatic interactions might cause macromolecule adsorption, results were obtained only for particles and fibers of like charge.

Following the approach in Anderson and Malone and subsequent hydrodynamic models of osmotic flow through "leaky" membranes (i.e., those that do not completely exclude solutes) (Anderson and Malone 1974, Anderson 1981, Zhang et al. 2006, Bhalla and Deen 2007, Bhalla and Deen 2009), the macromolecule was assumed to create (or influence) the flow only via its effect on the time-averaged pressure profile inside the membrane. As will be seen, steric or electrostatic exclusion of sphere centers from the vicinity of a fiber leads to pressure variations within the r-θ plane of Figure 4.2. The magnitude of those variations depends on the macromolecule concentration, and if an external concentration difference is maintained, the macromolecule concentration depends on z (as well as on r and θ). In that manner, solute-fiber interactions, combined with an imposed concentration difference, create the axial gradients in mechanical pressure that are responsible for the osmotic flow. Under the open-circuit conditions typical of membrane filtration, a streaming potential must develop to maintain zero net

current. As shown for osmosis in charged pores (Bhalla and Deen 2009), the body force associated with this potential gradient may reduce K significantly, but its effect on σ_o can be neglected. Thus, only the pressure gradients are important.

4.2.3 Momentum equation

Using the lubrication approximation and neglecting the electrical body force, the axial momentum balance is given by

$$\frac{\mu}{R^2}\left[\frac{1}{\rho}\frac{\partial}{\partial\rho}\left(\rho\frac{\partial v_z}{\partial\rho}\right)+\frac{1}{\rho^2}\frac{\partial^2 v_z}{\partial\theta^2}\right]=\frac{\partial P}{\partial z} \tag{4.4}$$

where ρ (= r/R) is the dimensionless radial coordinate, $v_z(\rho, \theta)$ is the axial velocity component, μ is the viscosity, and $P(\rho, \theta, z)$ is the pressure. At a fixed location in the fiber matrix, momentum transfer will be time-dependent, according to whether or not a particle (macromolecule) happens to be in the vicinity. Thus, v_z and P are interpreted as time-averaged quantities.

The advantage of adopting the annular geometry in Figure 4.2 is that it yields boundary conditions for v_z which are independent of θ. That is, $v_z = 0$ at $r = b$ (no slip at fiber) and $\partial v_z/\partial r = 0$ at $r = R$ (no shear stress at outer boundary). This suggests assuming that v_z is independent of θ, as in Zhang et al. (Zhang et al. 2006). However, interactions between the sphere and the surrounding fibers tend to make the macromolecule concentration, and therefore P and v_z, functions of θ. This is especially important when considering electrostatic interactions with the first ring of fibers. A less important contributor to the angular dependence is the maximum angle given by equation (4.3).

To obtain a more tractable problem, each term in equation (4.4) was averaged over the relevant range of angles ($0 \leq \theta \leq \pi/6$). This integration, together with symmetry, removes the θ-dependent viscous term. The result is

$$\frac{\mu}{R^2\rho}\frac{\partial}{\partial\rho}\left(\rho\frac{\partial\bar{v}_z}{\partial\rho}\right)=\frac{\partial\bar{P}}{\partial z} \tag{4.5}$$

where overbars denote averages over θ. For example,

$$\bar{P}(\rho,z)=\frac{6}{\pi}\int_0^{\pi/6}P(\rho,\theta,z)d\theta \quad . \tag{4.6}$$

The boundary conditions for $\bar{v}_z$ are those stated above for the θ-independent case.

4.2.4 Pressure distribution

Assuming osmotic equilibrium over the cross-section of the cylindrical channel, P - Π will be constant within any r-θ plane. Letting P_R and Π_R denote values at $r = R$, it follows that

$$\bar{P}(\rho,z)=\bar{P}_R(z)+\bar{\Pi}(\rho,z)-\bar{\Pi}_R(z). \tag{4.7}$$

The osmotic pressure includes contributions from the small ions as well as the macromolecule, and is given by

$$\bar{\Pi}(\rho,z)=R_gT\left[\bar{c}_+(\rho)+\bar{c}_-(\rho)+\bar{C}(\rho,z)\right] \tag{4.8}$$

where c_+, c_-, and C are the molar concentrations of the small cation, small anion, and macromolecule, respectively, and R_g is the gas constant. For macromolecules, the concentration at a particular point is defined as that of the sphere centers. Although equations (4.7) and (4.8) then imply an aphysical discontinuity in pressure at a distance a (one sphere radius) from any fiber surface, the corresponding error in the calculation of

σ_o appears to be negligible (Bhalla and Deen 2007). Implicit in equation (4.8) is that the solution is ideal.

4.2.5 Macromolecule concentration

Analogous to the situation for long pores, the time-averaged macromolecule concentration will be a separable function, such that

$$C(\rho,\theta,z) = f(z)g(\rho,\theta) = f(z)\exp\left[-E(\rho,\theta)/kT\right] \tag{4.9}$$

where E is the solute-fiber interaction energy per molecule and g is the corresponding Boltzmann factor (Deen 1987). Steric exclusion was modeled by setting $E = \infty$ within one sphere radius of a fiber, so that $C = 0$ for either $\rho < \alpha + \beta$ or $\theta > \theta_m$. The dimensionless sphere and fiber radii are $\alpha = a/R$ and $\beta = b/R$, respectively. For accessible sphere positions, E was evaluated by computing electrostatic free energies using a continuum double layer model, as described later. To calculate the osmotic reflection coefficient it is unnecessary to evaluate $f(z)$. As will be seen, it is sufficient to require that $f(0) - f(L) = C_1 - C_2 = \Delta C$, where C_1 and C_2 are the external concentrations at the two sides of the membrane.

4.2.6 Velocity profile

Because of the discontinuity in C at $\rho = \alpha + \beta$, equation (4.5) was integrated separately for $\beta < \rho < \alpha + \beta$ (the "core" region near the central fiber, where $\bar{v}_z \equiv w$) and $\alpha + \beta < \rho < 1$ (the "periphery," where $\bar{v}_z \equiv u$). With pressures and concentrations evaluated as just described, the differential equation for the periphery is

$$\frac{1}{\rho}\frac{\partial}{\partial\rho}\left(\rho\frac{\partial u}{\partial\rho}\right)=\frac{R^2}{\mu}\left[\frac{d\bar{P}_R}{dz}+R_gT\frac{df}{dz}\left(\bar{g}(\rho)-\bar{g}(1)\right)\right] \tag{4.10}$$

Integrating once, and applying the symmetry condition at $\rho = 1$, gives

$$\rho\frac{\partial u}{\partial\rho}=\frac{R^2}{2\mu}\left[\frac{d\bar{P}_R}{dz}-R_gT\frac{df}{dz}\bar{g}(1)\right](\rho^2-1)-\frac{R^2R_gT}{\mu}\frac{df}{dz}\int_\rho^1 x\bar{g}(x)dx \tag{4.11}$$

The differential equation for the core is the same as equation (4.10), except without the $\bar{g}(\rho)$ term. A first integration there yields

$$\rho\frac{\partial w}{\partial\rho}=\frac{R^2}{2\mu}\left[\frac{d\bar{P}_R}{dz}-R_gT\frac{df}{dz}\bar{g}(1)\right](\rho^2-1)-\frac{R^2R_gT}{\mu}\frac{df}{dz}\int_{\alpha+\beta}^1 x\bar{g}(x)dx \tag{4.12}$$

where equation (4.11) was used to ensure that the shear stress is continuous at $\rho = \alpha + \beta$.

A second integration for the core, and application of the no-slip condition at the fiber wall, gives the final expression for the velocity in that region:

$$\begin{aligned}w(\rho,z)=&-\frac{R^2}{4\mu}\left[\frac{d\bar{P}_R}{dz}-R_gT\frac{df}{dz}\bar{g}(1)\right]\left(\beta^2-\rho^2+2\ln(\rho/\beta)\right)\\&-\frac{R^2R_gT}{\mu}\frac{df}{dz}\ln(\rho/\beta)\int_{\alpha+\beta}^1 x\bar{g}(x)dx\end{aligned} \tag{4.13}$$

Another integration for the periphery, and matching the velocities at $\rho = \alpha + \beta$, completes the solution for the velocity profile:

$$\begin{aligned}u(\rho,z)=&-\frac{R^2}{4\mu}\left[\frac{d\bar{P}_R}{dz}-R_gT\frac{df}{dz}\bar{g}(1)\right]\left(\beta^2-\rho^2+2\ln(\rho/\beta)\right)\\&-\frac{R^2R_gT}{\mu}\frac{df}{dz}\int_{\alpha+\beta}^\rho\frac{dy}{y}\int_y^1 x\bar{g}(x)dx-\frac{R^2R_gT}{\mu}\frac{df}{dz}\ln\left(\frac{\alpha+\beta}{\beta}\right)\int_{\alpha+\beta}^1 x\bar{g}(x)dx\end{aligned} \tag{4.14}$$

Notice that the concentrations of the small ions do not appear in either velocity expression. However, the bulk electrolyte concentration and surface charge densities influence the electrostatic energy, and therefore affect the function $\bar{g}(\rho)$.

The integrals in equations (4.13) and (4.14) were evaluated numerically, using a shape-preserving spline interpolation to approximate the integrands. After the integrands were tabulated, the Matlab function "Fit" was employed, using the "spline interpolant" option. The integration was done then using Simpson's Rule, typically with 100 intervals.

To calculate σ_o, the velocity was integrated piecewise over ρ to find the mean velocity (U), which is independent of z. This integration was done numerically, as just described. The result for U was a linear function of the gradients $d\bar{P}_R / dz$ and df/dz. Integration over the fiber length then produced a relationship of the same form as Equation 1, permitting identification of σ_o. The changes in $\bar{P}_R$ and f over the pore length were related to the external pressure differences (ΔP and $\Delta \Pi$) by

$$\bar{P}_R(0) - \bar{P}_R(L) = \Delta P - \Delta \Pi\left[1 - \bar{g}(1)\right] \tag{4.15}$$

$$R_g T\left[f(0) - f(L)\right] = \Delta \Pi . \tag{4.16}$$

The one unknown function left to be discussed is $\bar{g}(\rho)$.

4.2.7 Electrostatic potential energy

The energy $E(\rho,\theta)$ was needed to compute the function $\bar{g}(\rho)$. This is the electrostatic free energy associated with moving a charged sphere from bulk solution to a specified position in the fiber matrix. Strictly speaking, in a continuum double layer model it should be obtained by solving the nonlinear Poisson Boltzmann equation.

However, for analogous calculations in cylindrical pores, the Boltzmann factors obtained from nonlinear and linearized formulations were found to be nearly identical (Bhalla and Deen 2009). This was true even for maximum values of $|\Psi|$ exceeding unity, where Ψ is the electrical potential scaled by the thermal voltage (R_gT/F, where F is Faraday's constant). Because the linearized (or Debye-Huckel) form of the Poisson-Boltzmann equation yields much simpler results, it was used in the present work. Energies were obtained for a system consisting of a sphere and a single fiber, and a pairwise additivity approximation was invoked to estimate the energy for the actual multifiber system. That approximation was tested by also computing "exact" results for a sphere interacting with two fibers, in either of two configurations.

In each of the energy calculations the dimensionless potential was assumed to be governed by the linearized Poisson Boltzmann equation,

$$\nabla^2\Psi = \tau^2\Psi \tag{4.17}$$

where ∇^2 is the dimensionless Laplacian operator and τ is the geometric length scale divided by the Debye length. If R is the geometric length scale, then

$$\tau = R\left(\frac{2F^2c_\infty}{\varepsilon R_gT}\right)^{1/2} = \kappa R \tag{4.18}$$

where ε is the permittivity of the solution and κ is the inverse of the Debye length. For a system consisting of a sphere and one or more fibers, each at constant surface charge density, the boundary conditions are

$$-\mathbf{n}\cdot\nabla\Psi = q_s = \frac{Q_sRF}{\varepsilon R_gT} \tag{4.19}$$

$$-\mathbf{n}\cdot\nabla\Psi = q_f = \frac{Q_f RF}{\varepsilon R_g T} \tag{4.20}$$

where **n** is a unit normal pointing into the solution, q_s and q_f are the dimensionless surface charge denisities of the sphere and fiber, respectively, and Q_s and Q_f are the corresponding dimensional values (in C/m^2). The permittivities of the sphere and fiber have been neglected and R has been chosen again as the geometric length scale. Of course, R is the length scale for the osmotic flow problem (Figure 4.2). In the various electrostatic problems to be described it was replaced by another length, as appropriate, depending on the particular geometry (isolated sphere, isolated fiber, sphere with one fiber, etc.).

Once the potential was computed, the electrostatic energy associated with a given object or collection of objects was calculated as

$$E_i = \frac{R_g T}{2F}\int_{S_i} Q_i \Psi dS \tag{4.21}$$

where the integration is over all surfaces (Verwey and Overbeek 1948). Then, E was computed as an energy difference. For example, for a sphere and a single fiber,

$$E = E_{sf} - E_s - E_f \tag{4.22}$$

where E_{sf}, E_s, and E_f are obtained by applying equation (4.21) to the two-body problem, an isolated sphere, and an isolated fiber, respectively. For a sphere and two fibers,

$$E = E_{sff} - E_s - E_{ff} \tag{4.23}$$

where E_{sff} is the energy for the three-body problem and E_{ff} is that for pair of fibers. In each case, E is the energy change associated with placing a sphere among a set of fibers.

Energies for a sphere and a single fiber were obtained previously using three-dimensional finite element solutions of equation 19, and the results summarized in a correlation (Johnson and Deen 1996). To obtain more accurate results for certain conditions, we computed additional sphere-fiber energies. This was done with COMSOL, using Lagrange quadratic basis functions and a stationary direct solver (UMFPACK). The adaptive mesh refinement feature was used, which automatically refines the mesh in regions where large gradients are detected. In the present work the half-length of the fiber was truncated at six Debye lengths. This yielded values of E for $\tau\alpha < 0.6$ which are significantly more accurate than those obtained previously, where the half-length was fixed at five sphere radii. The reason for the improvement is that, if the Debye length is large enough (τ small enough), five sphere radii will not include the entire length of fiber where the surface potential is perturbed noticeably by the sphere. For $\tau\alpha > 0.6$, the previous results for E were confirmed to be accurate. The point of transition ($\tau\alpha = 0.6$) corresponds to a cylinder half-length in the previous study equal to three Debye lengths; six Debye lengths were used in the present work only to be conservative.

For the multifiber osmotic flow geometry, the electrostatic interactions between the sphere and the fiber matrix were assumed to be pairwise additive. That is, E was approximated as the sum of the energies for individual sphere-fiber interactions. To test this assumption, "exact" values of E were computed for the two arrangements in Figure 4.3, each involving a sphere and two fibers. In one geometry (Figure 4.3A), the plane passing though the center of the sphere and the nearer fiber was perpendicular to that through the two fiber centers. The sphere-fiber separations are H_1 and H_2 and the fiber-

fiber separation is H. Results were obtained for various values of the dimensionless separations (κH_1, κH_2, and κH) and dimensionless sphere radius (a/b). The other geometry (Figure 4.3B) was a collinear arrangement, with the sphere equidistant from the two fibers. The fiber separation is denoted again as H, and results were obtained for various values of κH, κb and a/b. In each case, the computational domain was bounded by a cylinder of radius R_∞, at which the potential was set to zero. That radius was chosen so that the bounding surface was at least six Debye lengths from the surface of any object. Likewise, normal to the plane of Figure 4.3, the half-length of the domain was chosen as six Debye lengths. This yielded energies which were independent of the outer radius and half-length, to within 2%. The energies for the two geometries were obtained using COMSOL, as described above. Those "exact" results were compared with values of E calculated using pairwise additivity. As will be shown, the pairwise additivity approximation yielded reasonably good results.

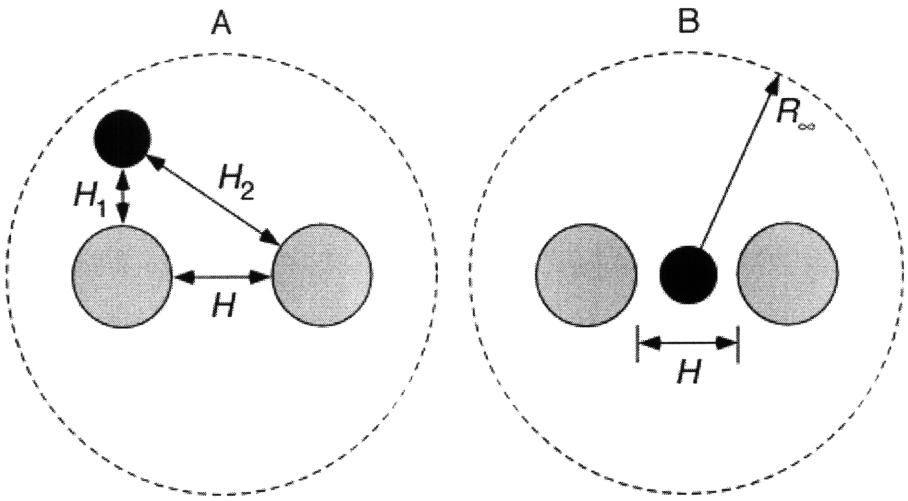

Figure 4.3 Sphere-fiber systems used to test pairwise additivity of energies: A, perpendicular configuration with one fiber nearer the sphere; B, collinear arrangement with the fibers equidistant from the sphere. The dashed circles represent the outer boundaries of the cylindrical domains used in the three-dimensional finite element calculations

When applying pairwise additivity to the periodic arrangement in Figure 4.1, it turned out to be sufficient to consider only seven fibers (the central one and the six nearest neighbors). It was found that including the second layer of twelve fibers altered the value of E by no more than 1%. Referring to the coordinates in Figure 4.2, the angular-average Boltzmann factor needed for the flow problem was calculated as

$$\bar{g}(\rho) = \frac{6}{\pi} \int_0^{\pi/6} \exp\left[-E(\rho,\theta)/kT\right] d\theta \quad . \tag{4.24}$$

4.2.8 Parameters

Whereas the hydraulic permeability (K in Equation 1) scales as $R^2/\mu L$, the reflection coefficient is determined by the shape of the velocity profile (i.e., the dimensionless functions that multiply either $d\bar{P}_R / dz$ or $R_g T df/dz$ in equations (4.13) and (4.14)). The form of the velocity profile depends on α (sphere radius/flow radius), β (fiber radius/flow radius), and the parameters that influence $\bar{g}(\rho)$. Those include τ (flow radius/Debye length, equation (4.18)), q_s (dimensionless sphere charge density, equation (4.19)), and q_f (dimensionless fiber charge density, equation (4.20)). Also involved is

$$\xi = \frac{(R_g T / F)^2 \varepsilon R}{kT} \tag{4.25}$$

which arises when E is made dimensionless using the thermal energy. Thus, the form of the velocity solution, together with dimensional analysis of E, indicates that

$$\sigma_o = \sigma_o \left(\alpha, \beta, \tau, q_s, q_f, \xi\right) . \tag{4.26}$$

In other words, σ_o depends on six dimensionless parameters. Because the fiber volume fraction (ϕ) is often known experimentally, it is desirable to adopt it as one of the parameters. In a plane of constant z (as in Figure 4.2), ϕ equals the area of one fiber divided by the total area per fiber. Thus,

$$\phi = \left(\frac{b}{R}\right)^2 = \beta^2 \quad . \tag{4.27}$$

Accordingly, we simply replace β in equation (4.26) by ϕ, and conclude that

$$\sigma_o = \sigma_o \left(\alpha, \phi, \tau, q_s, q_f, \xi\right) . \tag{4.28}$$

In contrast, for an uncharged system, $\sigma_o = \sigma_o(\alpha, \phi)$ only (Zhang et al. 2006).

With σ_o dependent on six dimensionless groups, a complete exploration of the model predictions was impractical. Accordingly, we focused on certain conditions which are likely to be of physiological interest. Two kinds of fiber matrices were considered. The first (Model 1) is a hypothetical array of GAG chains of varying ϕ. To represent a GAG chain as a charged fiber, it has been proposed that b = 0.5 nm and Q_f = -0.10 C/m^2 (Mattern et al. 2008). From equations (4.1), (4.2), and (4.27), a sphere the size of serum albumin (a = 3.6 nm) will be completely excluded by such an array if $\phi > 0.018$. Accordingly, with Model 1 we considered only $0 \leq \phi \leq 0.020$. The other fiber matrix (Model 2) is the endothelial glycocalyx structure of Zhang et al., which has fibers much thicker than GAG chains (Zhang et al. 2006). In this case the geometry is specified rather precisely (b = 6 nm, H = 8 nm, R = 10.5 nm, and ϕ = 0.33) but the surface charge density is unknown. Thus, with Model 2 we viewed Q_f as a variable. A range of solute sizes was considered with each model, with BSA used as a benchmark for charge density. Modeling BSA as a sphere with a = 3.6 nm and a net charge of -20 gives Q_s = -0.020 C/m^2 (Vilker et al. 1981). Except where noted otherwise, c_∞ = 0.15 M.

4.3 RESULTS

4.3.1 Sphere-fiber electrostatic energy

In using pairwise additivity to calculate E for the multifiber system it was necessary to have results for a sphere interacting with a single fiber. When equations (4.17) and (4.21) are valid, E is a quadratic function of the surface charge densities (Johnson and Deen 1996). This may be expressed as

$$\frac{E}{\xi kT} = A_1 q_s q_f + A_2 q_s^{\,2} + A_3 q_f^{\,2} \tag{4.29}$$

where the coefficients A_i are each functions of α, τ, and the surface-to-surface separation, but are independent of ξ and the charge densities. For this system, the characteristic length used in α, τ, q_s, q_f, and ξ is b (rather than R). The dimensional separation is denoted as h and the dimensionless separation is $\eta = \kappa h$. There are energies for a charged sphere interacting with an uncharged fiber ($A_2 > 0$) and for an uncharged sphere interacting with a charged fiber ($A_3 > 0$), because a nearby uncharged object of low dielectric constant will distort the diffuse double layer around a charged object. That will affect its surface potential at constant charge density. However the additional energy contribution when both objects are charged tends to be dominant ($A_1 > A_2$ or A_3).

It was shown previously that the results of some 900 three-dimensional finite element calculations for various combinations of inputs could be correlated as

$$A_i(\alpha, \tau, \eta) = a_i \alpha^{b_i} \tau^{-c_i} \exp(-\eta d_i) \tag{4.30}$$

where a_i, b_i, c_i, and d_i are constants obtained from a least squares fit (Johnson and Deen 1996). The constants reported before are accurate for $\tau\alpha > 0.6$, as already mentioned. To improve the results for $\tau\alpha < 0.6$, we computed energies for an additional 60 cases with $0.5 < \tau < 2$, $0.2 < \alpha < 0.6$, and $0.1 < \eta < 0.5$. A new set of constants for equation (4.30) was obtained by doing nonlinear least-squares fits using MATLAB. Those constants represented E well enough to give a root-mean-square error in the Boltzmann factor [exp(-E/kT)] of 10 % for $\tau\alpha < 0.6$. Both sets of constants are given in Table 4.1. The data used for the regression is shown in the Appendix C.

Table 4.1 Constants for Sphere-Fiber Energy Correlation.

Range of $\tau\alpha$	Index (i)	a_i	b_i	c_i	d_i
< 0.6	1	3.9006	0.7367	0.7814	1.2076
	2	0.276	0.8094	0.4518	2.7655
	3	0.5641	0.9322	0.1699	2.9824
> 0.6	1	2.3523	-0.0071	1.2472	1.0956
	2	0.357	0.5436	0.9512	3.7684
	3	0.4473	-0.0822	1.1512	2.4987

When used in equation 4.30, these constants give the electrostatic free energy for double-layer interactions between a sphere and a single fiber (cylinder of indefinite length), each with a constant surface charge density. The results for $\tau\alpha < 0.6$ are from the present work, whereas those for $\tau\alpha > 0.6$ were reported previously (Johnson and Deen, 1996).

4.3.2 Pairwise additivity

The assumption that the sphere-fiber energies are pairwise additive (or that the corresponding Boltzmann factors are multiplicative) was tested using the two geometries in Fig. 22. For the perpendicular arrangement, 60 cases were examined with $0.5 < \kappa b < 2$, $0.1 < a/b < 0.9$, $0.5 < \kappa H < 3$, $0.6 < \kappa H_1 < 3$, and $0.5 < \kappa H_2 < 15$; for the collinear geometry, 20 cases were tested with κb, a/b, and κH in the ranges just stated. In each case the "exact" Boltzmann factor obtained from the full finite element calculation was compared with that found using pairwise additivity. To avoid the effects of any errors

introduced by using equation (4.30), each two-body energy was generated using the same finite element procedure as with the three-body problem. As shown in Figure 4.4, for the perpendicular arrangement the agreement between the exact and pairwise Boltzmann factors was remarkably good. The agreement was usually good also for the collinear configuration, although there were large errors in a few cases. In the latter arrangement, when errors occurred the pairwise additivity assumption overestimated the Boltzmann factor. The values are tabulated in Table C.1 and C.2 in Appendix C. As shown in equation (4.25), a length scale arises when E is made dimensionless using the thermal energy. For the pairwise additivity calculations, the length scale was chosen to be 20nm.

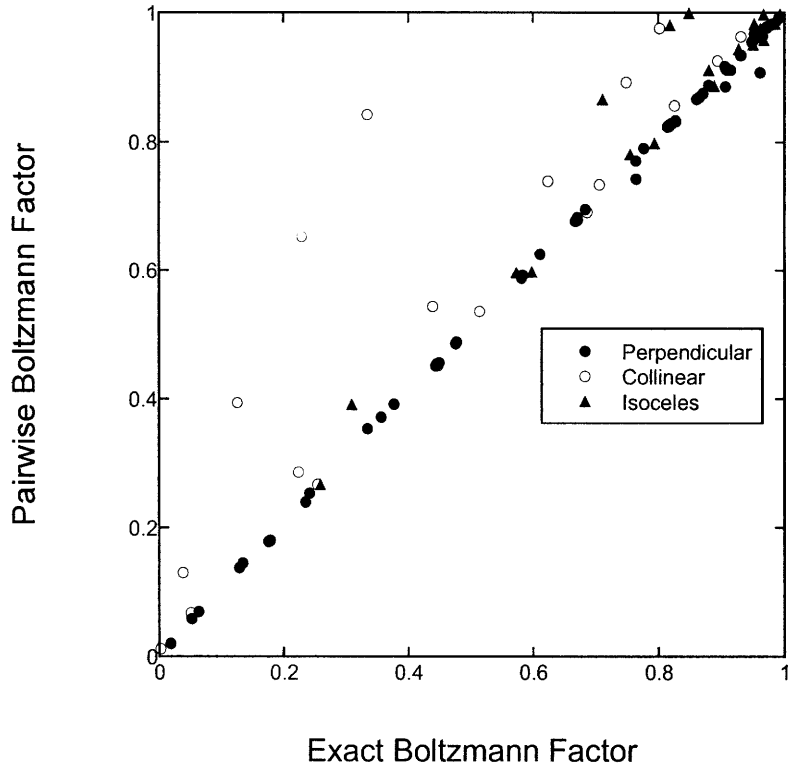

Figure 4.4 Comparison of exact and pairwise-additive Boltzmann factors [exp(-*E*/*kT*)] for a charged sphere interacting with two charged fibers. "Perpendicular" and "collinear" refer to the arangements in Figures 4.3A and 4.3B, respectively and the isosceles arrangement refers to a sphere placed on one vertex of an isosceles triangle with the two cylinders on the other two vertices.

These results suggest that if one fiber is nearest the sphere (which is always true for the perpendicular arrangement in Figure 4.3A), pairwise additivity is a reliable way to correct *E* for the effects of more distant fibers. Having two or more fibers equidistant from the sphere (as in Figure 4.3B) probably is a worst case, in that no single interaction

is most important. Because a sphere placed randomly within a hexagonal lattice is likely to have a single nearest-neighbor fiber, we conclude that pairwise additivity is a reasonable approximation, at least until a practical alternative can be developed. Incidentally, when the pairwise Boltzmann factors were computed using equation (4.30), the results were nearly identical to those in Figure 4.4. These results are shown in Figure 4.5. This indicates that the correlation itself does not introduce significant error in the energy calculations, and that the main concern is the pairwise additivity assumption.

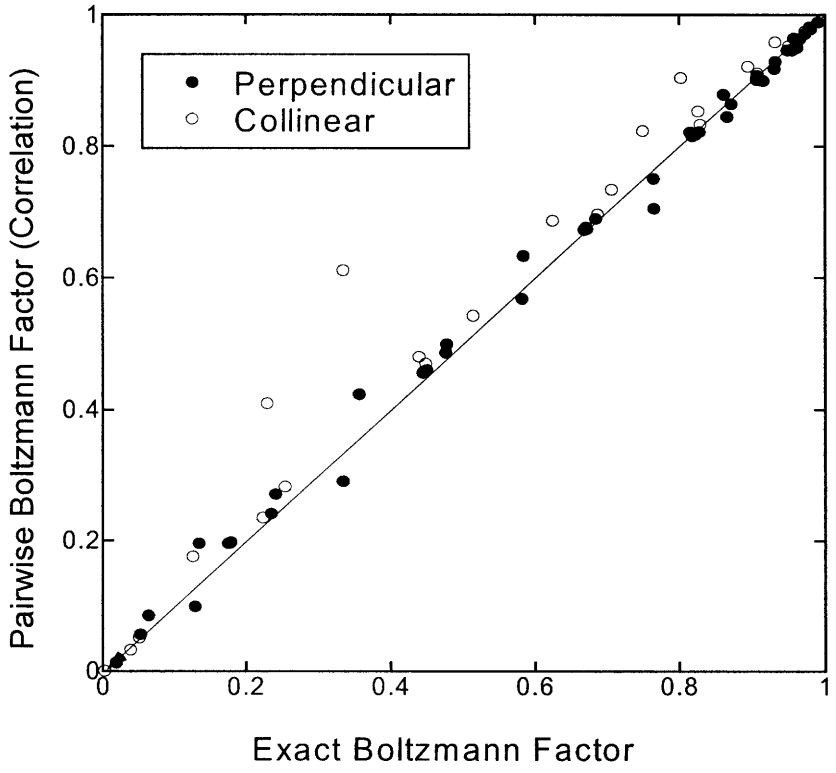

Figure 4.5 Comparison of exact and pairwise-additive Boltzmann factors using equation (4.30) [exp(-*E/kT*)] for a charged sphere interacting with two charged fibers. "Perpendicular" and "collinear" refer to the arangements in Figures 4.3A and 4.3B, respectively.

4.3.3 Osmotic reflection coefficient

Figure 4.6 shows the effect of streaming potential on hydraulic permeability similar to the Figure 3.3. The effects on hydraulic permeability for the fiber case for similar charge density are lower than that of the porous case. Hence the effects of streaming potential on fiber case are assumed to be negligible.

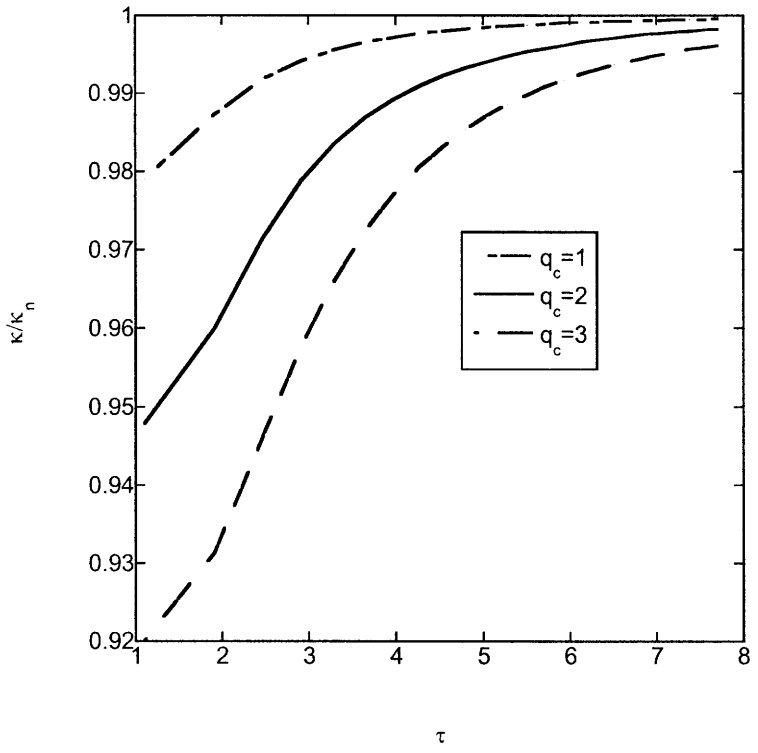

Figure 4.6 Effect of τ (pore radius/Debye length) and pore charge density (q_c) on the hydraulic permeability (κ) defined in equation (1.1). The hydraulic permeabilty for charged fiberss is compared with that for neutral fibers of the same size.

We begin with Model 1, which is based on GAG properties. Figure 4.7 shows σ_o for BSA as a function of fiber volume fraction (ϕ), for several salt concentrations (c_∞). Higher volume fractions correspond to smaller interfiber spaces, so that in each case σ_o increases with increasing ϕ. For the BSA and GAG radii, complete solute exclusion does not occur until $\phi = 0.018$, but $\sigma_o \to 1$ well before that, depending on the salt concentration. Decreasing the ionic strength (as might be done in vitro) increases the Debye length and therefore amplifies the repulsive sphere-fiber electrostatic interactions. Accordingly, at a given ϕ, decreases in c_∞ elevate σ_o. Also shown is a curve for uncharged spheres and fibers with the same radii as BSA and GAG, respectively. The increase in σ_o due to the charge of BSA and GAG is seen to be quite significant. For example, at a physiological salt concentration ($c_\infty = 0.15$ M) and $\phi = 0.005$, charge effects are predicted to increase σ_o from 0.30 to 0.85.

The effects of charge vanish as $\phi \to 0$, and the curves in Figure 4.7 all converge at $\sigma_o = 0$. With the fiber radius fixed, $\phi \to 0$ corresponds to a fiber-fiber separation increasing without bound. As the interfiber separation increases, so does the average sphere-fiber separation, and therefore $E \to 0$ for an increasing fraction of the possible sphere positions. Thus, electrostatic interactions become unimportant. Likewise, as the sphere centers are excluded from smaller and smaller fractions of the liquid volume, steric effects vanish. As shown by Zhang et al. (2006), for a neutral system $\sigma_o \to \alpha^2$ as $\phi \to 0$, and with the sphere radius constant, α vanishes along with ϕ.

Over most of the range of ϕ in Figure 4.7, our numerical results for the neutral case are within 1% of those obtained from the analytical expression of Zhang et al.

(2006) (not shown). Noticeable deviations occur only for $\phi > 0.014$, the most tightly fitting cases. The analytical expression predicts that $\sigma_o = 1$ at $\phi = 0.015$, and yields unrealistic values ($\sigma_o > 1$) if applied at larger volume fractions; the numerical results for σ_o approach unity asymptotically as $\phi \rightarrow 0.018$ (the absolute steric cutoff). Accounting for the limits on sphere angular position (equation (4.3)) is what enables the numerical results to be more realistic for the tightly fitting cases.

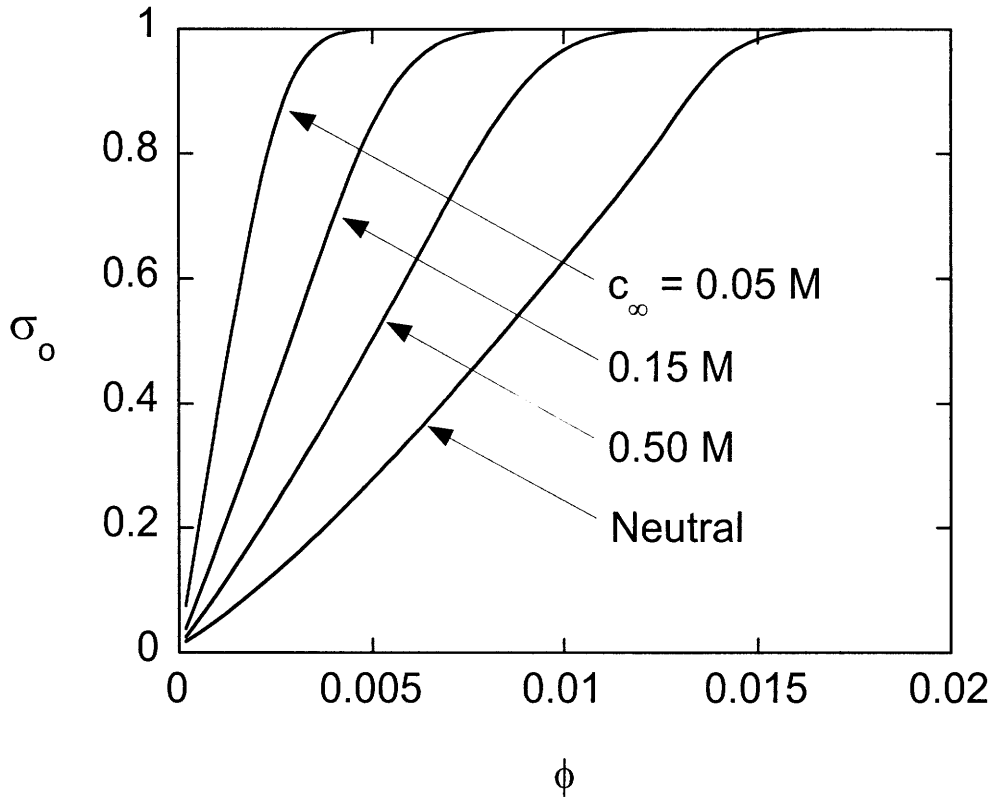

Figure 4.7 Osmotic reflection coefficient (σ_o) as a function of fiber volume fraction (ϕ) for Model 1 (GAG parameters) and BSA. Results are shown for BSA and GAG at three electrolyte concentrations, and for an uncharged system with the same solute and fiber radii.

Figure 4.8 shows the effects of solute radius, again for Model 1. Here σ_o is plotted as a function of a for several values of ϕ. In each case the sphere surface charge density is assumed to be that of BSA. As expected, for any constant fiber volume fraction, increasing the solute radius increases σ_o. For any fixed solute radius, increasing the fiber volume fraction increases σ_o. as shown already for BSA in Figure 4.7.

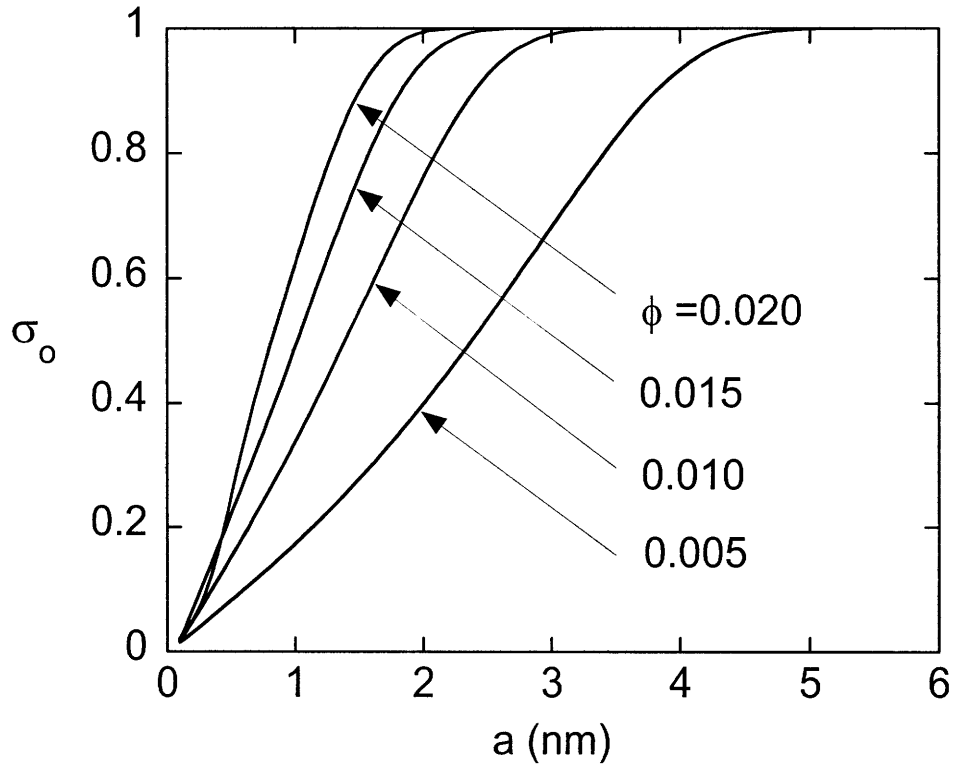

Figure 4.8 Osmotic reflection coefficient as a function of solute radius for Model 1 (GAG parameters). Curves are shown for four fiber volume fractions, with Q_s = 0.020 C/m^2 in each case.

The effects of solute radius are illustrated again in Figure 4.9, this time for Model 2, the endothelial glycocalyx structure of Zhang et al. (Zhang et al. 2006). In this plot the surface charge density is the second variable (rather than the fiber volume fraction), and for each curve it is assumed that $Q_s = Q_f = Q$. The upper bound chosen for $|Q|$ is that for a GAG fiber. (The absolute value is used here because the fibers and solutes are both assumd to be negatively charged throughout.) It is seen that σ_o increases with a when Q is fixed, and that it increases with $|Q|$ when a is held constant. The neutral curve in

Figure 4.9 differs from that in Figure 4.6 because b and ϕ are not the same in the two plots.

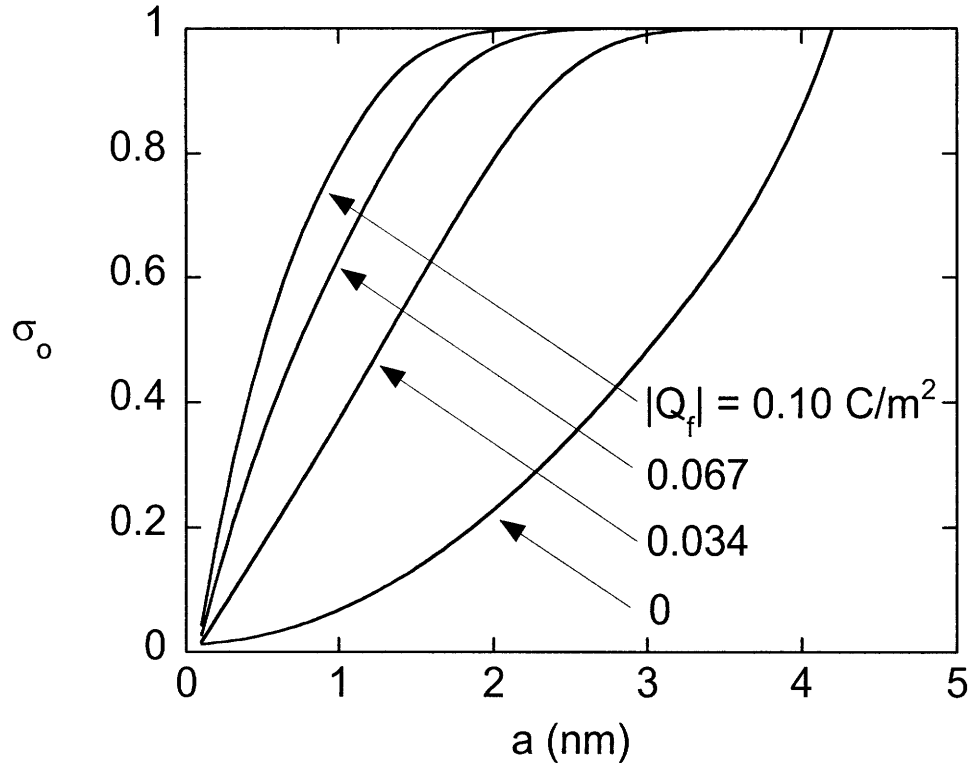

Figure 4.9 Osmotic reflection coefficient as a function of solute radius for Model 2 (endothelial glycocalyx parameters). Curves are shown for four sphere and fiber charge densities, with $Q_s = Q_f$

A feature of Model 2 mentioned earlier is that the fiber charge density is unknown. Figure 4.10 shows σ_o for this model as a function of $|Q_f|$ for several values of Q_s, with the solute size fixed at a = 3.6 nm (as for BSA). Whether $|Q_f|$ and $|Q_s|$ are elevated separately or in combination, σ_o is increased above its fully neutral value of 0.68. The different σ_o intercepts at $|Q_f| = 0$, and the increasing trend seen in the curve for

$|Q_s| = 0$, each reflect the fact that there are electrostatic interactions even if only one object is charged. (This was mentioned already in connection with equation (4.29).)

The largest solute charge density shown in Figure 4.10 corresponds to that of BSA. Serum albumins tend to be highly retained in the circulation, with $\sigma_o > 0.9$ typically. Such high selectivity is not predicted for BSA and neutral fibers, where $\sigma_o = 0.75$ in Figure 4.10 (somewhat above the fully neutral value of 0.68). It is seen that a fiber charge density of only -0.01 C/m^2 is required to make $\sigma_o > 0.9$. This is only one-half the charge density of BSA or one-tenth that of a GAG chain. This indicates that, with realistic fiber charge densities, the endothelial glycocalyx alone migtht be capable of retaining albumin with the efficiency typcally observed in normal capillaries.

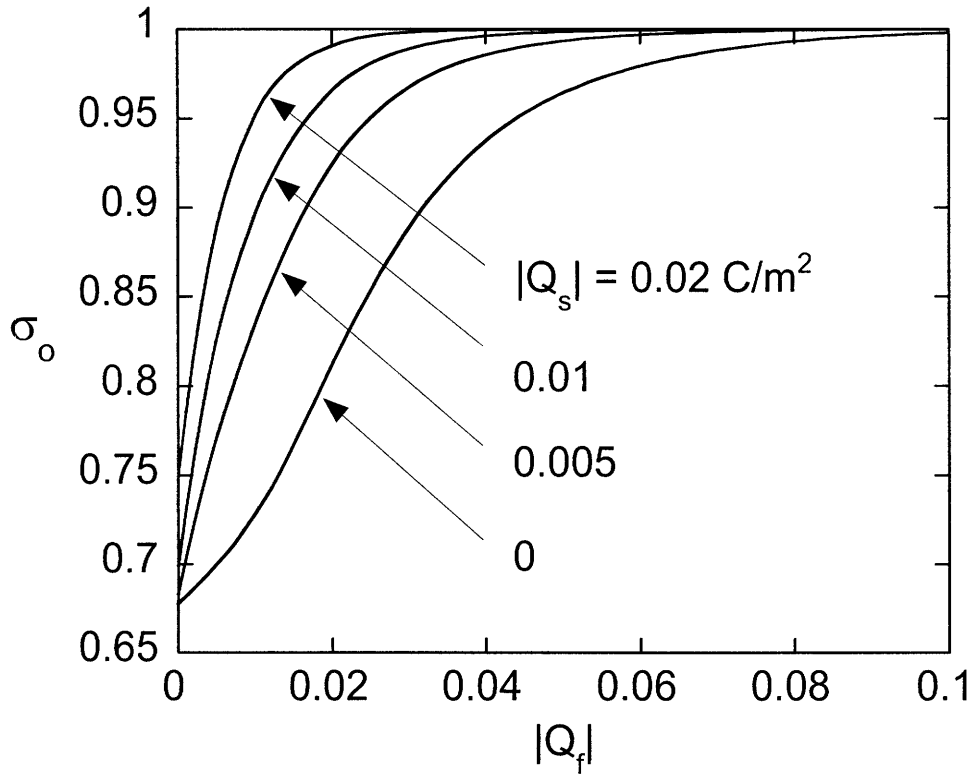

Figure 4.10 Osmotic reflection coefficient as a function of fiber charge density for Model 2 (endothelial glycocalyx parameters). Curves are shown for four sphere charge densities.

4.4 DISCUSSION

A computational model was developed to predict the osmotic reflection coefficient for charged, spherical, macromolecules in membranes consisting of regular arrays of charged fibers. To obtain a tractable problem, we assumed that the fibers are arranged on a hexagonal array and that flow is parallel to the fiber axes, as done by Zhang et al. in their analysis of osmosis in an uncharged system (Zhang et al. 2006). Whether charge is present or not, the underlying mechanism for osmotic flow in these models is that proposed by Anderson and Malone for porous membranes (Anderson and

Malone 1974). That is, steric and/or electrostatic exclusion of solute centers from the vicinity of fiber surfaces (or pore walls), combined with local osmotic equilibrium in the transverse direction, creates concentration-dependent variations in mechanical pressure in that direction. When there is a concentration difference imposed across the membrane, this leads to the axial gradients in mechanical pressure that are responsible for the osmotic flow. When solutes and fibers are of like charge and have constant surface charge densities, solute-fiber electrostatic interactions are strictly repulsive. The effect of solute and/or fiber charge is to create repulsive interactions which are longer range than purely steric ones. Hence, there is increased exclusion of macromolecular solutes from the membrane and σ_o with charge effects exceeds that for an otherwise identical, neutral system. The osmotic reflection coefficient becomes a function then not only of solute size, fiber size, and fiber volume fraction, but also solute charge density, fiber charge density, and electrolyte concentration. The factors that affect σ_o are stated more precisely in equation (4.26), which lists all the pertinent dimensionless groups.

Perfectly selective exclusion of solute molecules is the defining feature of an ideal, semipermeable membrane, where $\sigma_o = 1$; failure to discriminate between solute and solvent molecules precludes osmosis, in which case $\sigma_o = 0$. Accordingly, σ_o is related to the partition coefficient (Φ), which is the solute concentration in the membrane relative to that in bulk solution, at equiilbrium. For hydrogels or other fibrous media, it is conventional to base the intramembrane concentration on total volume (solid plus liquid). Accordingly, for the fiber array modeled here (Figure 4.2),

$$\Phi = \frac{12}{\pi} \int_0^{\pi/6} \int_{\alpha+\beta}^{1} \exp\left[-E(\rho,\theta)/kT\right] \rho \, d\rho \, d\theta \tag{4.31}$$

The relationship between σ_o and Φ is examined in Figure 4.11, where each point corresponds to a combination of parameter values considered in Figures 4.7-4.10 The abscissa, $\Phi/(1 - \phi)$, corresponds to a partition coefficient in which intramembrane concentrations are based on liquid volume, as in porous membranes. Even with this adjustment for fiber volume fraction, the results are seen to follow two different relationships, one corresponding to Model 1 ($\phi << 1$) and the other Model 2 ($\phi = 0.34$). This is in contrast to what has been found for porous membranes, where all results for a given pore shape tend to scatter about a single curve (Anderson and Malone 1974; Anderson 1981, Bhalla and Deen 2007, Bhalla and Deen 2009). (The relationships differ somewhat depending on pore shape, and the scatter for a given shape is reduced significantly if charge effects are absent.) If the abscissa had been Φ (partitioning based on total volume), the two sets of points in Figure 4.11 would have been separated much more. This is shown in Figure 4.12.

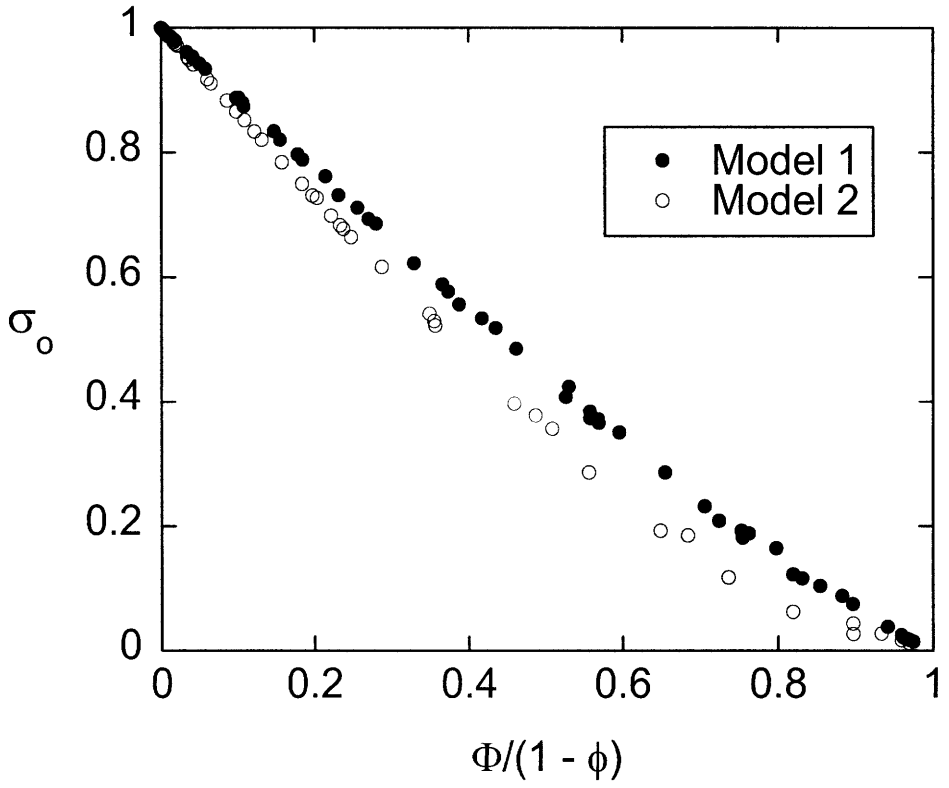

Figure 4.11 Relationship between osmotic reflection coefficient and equilibrium partition coefficient (Φ). The abscissa corresponds to a partition coefficient that has been adjusted using the fiber volume fraction (ϕ) to base intramembrane concentrations on liquid volume. Each point corresponds to a set of parameter values from Figures 4.7-4.10, with filled symbols from Model 1 and open symbols from Model 2.

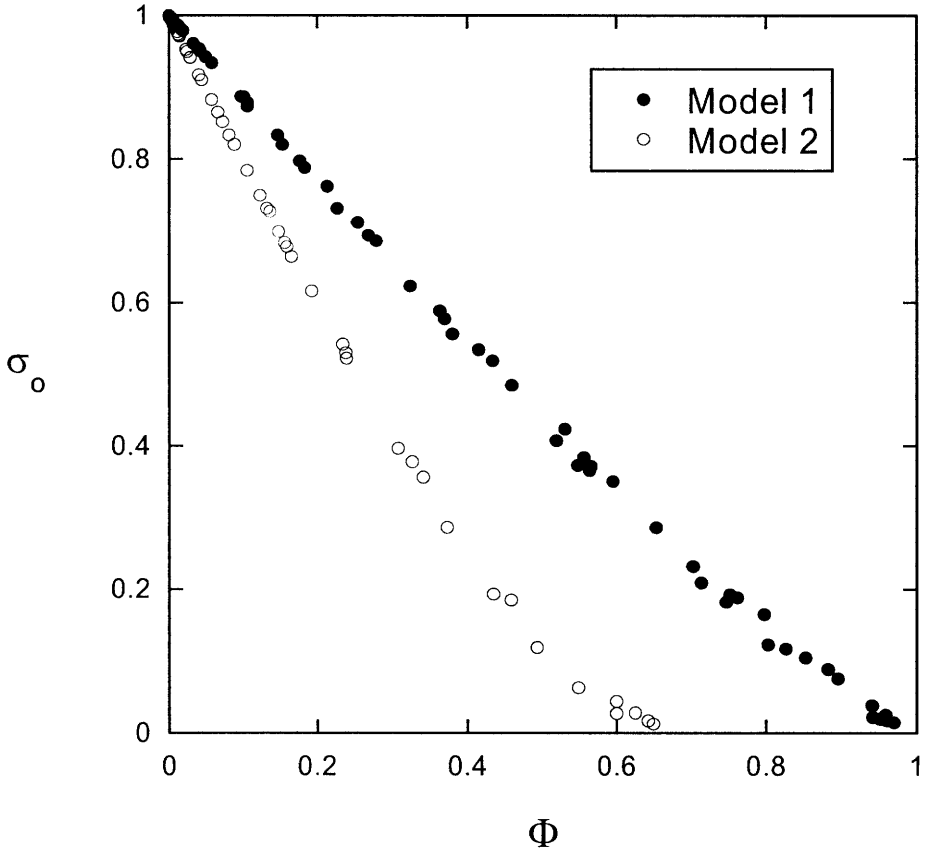

Figure 4.12 Relationship between osmotic reflection coefficient and equilibrium partition coefficient (Φ). Each point corresponds to a set of parameter values from Figures 4.7-4.10, with filled symbols from Model 1 and open symbols from Model 2.

We conclude from Figure 4.11 that, for charged solutes and charged fibrous membranes, there is no universal relationship between σ_o and Φ. The absence of such a relationship is evident also in the analytical results of Zhang et al. for neutral solutes and fibers, where $\Phi\,[= 1 - (\alpha + \beta)^2]$ depends only on $\alpha + \beta$, but σ_o is a complicated function of α and β separately (Zhang et al. 1996). (The neutral result for Φ follows from equation 4.31 by setting $E = 0$ and ignoring the restriction on sphere angular positions.)

The main difficulty we encountered was how to evaluate the electrostatic free energy (E) for a sphere interacting with a hexagonal array of fibers of indefinite extent. Because of the three-dimensional geometry and the need to resolve details of the potential over distances sometimes much smaller than the fiber-fiber separation, direct finite element solutions of equation (4.17) for a sphere interacting with many fibers were not feasible. In preliminary calculations we explored the singularity method of Phillips which in principle is well suited for solving equation (4.17) in settings where boundary conditions must be imposed on the surfaces of multiple objects (Phillips 1995). Although we found this method to work well for certain test cases (e.g., a pair of spheres), the ability to satisfy the constant charge density boundary conditions turned out to be very sensitive to the placement of the internal singularities and the selection of surface points. Because it was impractical to optimize the singularity method for each of the many asymmetrical sphere positions we had to consider, we abandoned it in favor of a pairwise additivity assumption for the energies.

Pairwise additivity, when combined with a correlation for the interaction energy between a sphere and a single fiber (equation (4.30)), was straightforward to implement. As shown in Figure 4.4, Boltzmann factors calculated using pairwise additivity, while

imperfect, were usually reliable in tests involving a sphere and two fibers. When significant errors occurred, there was a tendency to overestimate the Boltzmann factor, which in turn would overestimate Φ and underestimate σ_o. In that sense, the predicted increases in σ_o due to charge are conservative. Although the accuracy of the σ_o results would be improved if E could be computed more precisely, we think it unlikely that any of the plots would change significantly.

For both types of fiber arrays considered, one based on the properties of GAG chains and the other corresponding to the endothelial surface glycocalyx model of Zhang et al., σ_o for BSA was predicted to be much larger than that for a neutral system (Figures 4.7 and 4.10) (Zhang et al. 2006). Thus, whether one envisions capillary walls as having a barrier like the glycocalyx structure of Zhang et al., or one consisting simply of an array of GAG chains, this suggests that charge is important in minimizing albumin loss from the circulation (Zhang et al. 2006). This conclusion is based on the equality (or near equality) of σ_o and σ_f and the assumption that minimizing convective transport through capillary walls is crucial for retaining albumin. Of course, an array of GAG chains is unlikely to be as highly ordered as assumed in Figure 4.1, and even so, the flow may not be parallel to the fibers. It would be worthwhile to extend this type of model to flow perpendicular to an array of fibers. The results for the parallel and perpendicular problems might then be combined to predict σ_o for arrays of randomly oriented fibers, perhaps using "mixing rules" analogous to those used to estmate the hydraulic permeability of such arrays (Mattern et al. 2008).

Appendix A. PRESSURE PROFILES AND VOLUME FRACTION CALCULATION

Pressure profile derivation for surface locator for a sphere in a slit pore

For a surface locator at a given coordinate y (as shown in Figure A.1), the average Boltzmann factor is given by

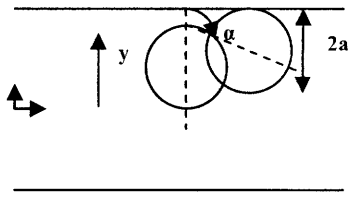

Figure A.1 Sphere with a surface locator at position y, α is the maximum angle allowable

$$\left\{\exp(-\psi)\right\} = \frac{\int_{\alpha}^{\pi} \sin\theta d\theta}{\int_{0}^{\pi} \sin\theta d\theta} = \frac{1+\cos(\alpha)}{2} = \frac{1-y}{2\lambda} \tag{A.1}$$

Therefore,

$$\left\{\exp(-\psi)\right\} = \begin{cases} 1 & \text{for } y/H < 1-2\lambda \\ \dfrac{1-y}{2\lambda} & \text{for } y/H > 1-2\lambda \end{cases} \tag{A.2}$$

Assuming Osmotic equilibrium of the solute in the transverse direction, we have for the pressure

$$P(x,y) = P_0(x) + kTf(y)\left\{\frac{1-y}{2\lambda} - \frac{1}{2\lambda}\right\} \tag{A.3}$$

For Figure 2.2, we have

$$\frac{P-P_1}{P_0-P_1}=1-y \tag{A.4}$$

Volume fraction for spheres in slit pores

Following is a derivation of the configuration-averaged particle volume fraction for spheres in slit pores, $\varphi(y)$. In this parallel-plate geometry the midplane corresponds to $y = 0$ and the walls are at $y = \pm H$. Considering first the effect of a single sphere of radius a centered at $(X,Y.Z)$, the solid volume fraction at point (x,y,z) will be either unity or zero, depending on whether the sphere does or does not engulf that point. This is expressed by the function

$$F(x,y,z,X,Y,Z)=\begin{cases}1 & (x-X)^2+(y-Y)^2+(z-Z)^2<a^2\\ 0 & (x-X)^2+(y-Y)^2+(z-Z)^2>a^2\end{cases} \tag{A.5}$$

The average volume fraction at a point is obtained by integrating over all possible sphere positions. If a sphere center can occupy all positions with equal probability, as in an unbounded solution, then

$$\varphi(x,y,z)=C_\infty\int_{-\infty}^{\infty}\int_{-\infty}^{\infty}\int_{-\infty}^{\infty}F\,dX\,dY\,dZ=C_\infty V=\varphi_\infty \tag{A.6}$$

where C_∞ is the number concentration of spheres, V ($=4\pi a^3/3$) is the sphere volume, and φ_∞ is the volume fraction based on C_∞. In this case, the integration yields exactly one sphere volume. The only spheres that can engulf the point in question, and thereby contribute to the average particle volume fraction there, are ones whose centers are within

that volume. In a pore, however, sphere centers are excluded from layers of thickness a next to the walls. If their concentration elsewhere is constant at C_∞, then

$$\varphi(x,y,z) = C_\infty \int_{-\infty}^{\infty} \int_{-H+a}^{H-a} \int_{-\infty}^{\infty} F\, dX\, dY\, dZ \tag{A.7}$$

The volume integral corresponds now to a sphere truncated at the top and/or bottom by the planes $y = H - a$ and $y = -H + a$. Where the truncation occurs depends on y and the relative sphere size, $\lambda = a/H$, as given below. The relative volume fraction φ/φ_∞ equals the truncated volume divided by the full sphere volume.

For spheres that span no more than half the pore ($\lambda \le 0.5$), the volume fraction at a given y is affected at most by one wall and

$$\frac{\varphi(\beta)}{\varphi_\infty} = \begin{cases} 1 & 0 \le \beta \le 1-2\lambda \\ \dfrac{(1-\beta)^2}{4\lambda^3}\left[3\lambda - (1-\beta)\right] & 1-2\lambda \le \beta \le 1 \end{cases} \tag{A.8}$$

where $\beta = y/H$. (Because of the symmetry, results are needed only for $y > 0$.) For larger spheres ($\lambda > 0.5$), both walls are influential and

$$\frac{\varphi(\beta)}{\varphi_\infty} = \begin{cases} \dfrac{(1-\lambda)}{2\lambda^3}\left[3\left(\lambda^2-\beta^2\right) - (1-\lambda)^2\right] & 0 \le \beta \le 2\lambda - 1 \\ \dfrac{(1-\beta)^2}{4\lambda^3}\left[3\lambda - (1-\beta)\right] & 2\lambda - 1 \le \beta \le 1 \end{cases} \tag{A.9}$$

Volume fraction for spheres in cylindrical pores

For a sphere of radius a in a cylindrical pore of radius R, the ratio φ/φ_∞ equals the volume of a sphere truncated by the cylindrical surface $r = R - a$, relative to the full sphere volume. In this geometry the truncated volumes were evaluated using a Monte Carlo method, as they could not be obtained analytically. Points inside a sampling volume centered on the sphere were chosen at random, and those within the sphere were

identified. The fraction of those which also satisfied $r < R - a$ provided the value of φ/φ_∞. For $\lambda = a/R < 0.5$, the sampling volume was a cube of edge length $2a$. For $\lambda > 0.5$, it was more efficient to employ a cuboid with edge lengths of $2(R - a)$ in the cross-sectional directions and $2a$ in the axial direction. The volume fraction results for spheres in slit and cylindrical pores are compared in Figure A.2. For small λ, the effects of wall curvature are negligible and the results for the two pore geometries are nearly the same. For larger λ, the more severely constrained space in a cylindrical pore causes the volume fractions there to be smaller than for slit pores.

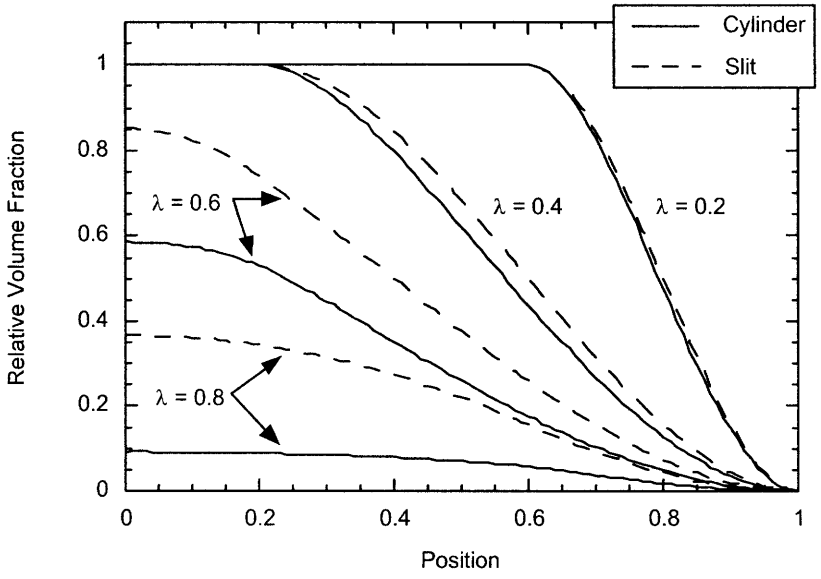

Figure A.2 Configuration-averaged volume fractions of spheres in cylindrical and slit pores. The volume fraction relative to bulk solution (φ/φ_∞) is plotted as a function of transverse position ($\beta = r/R$ or y/H) for various sphere sizes ($\lambda = a/R$ or a/H). The cylindrical results are based on Monte Carlo calculations and the slit results are from equations A.8 and A.9.

Volume fraction for spheroids in slit pores

The calculations for spheroids in slit pores were analogous to using equation A.3, except that it was necessary also to integrate over all particle orientations. The major axis of the particle was chosen as a reference, and the polar angle (θ) was defined as the tilt of that reference relative to the y axis. Because of the flat walls, there was no dependence on the azimuthal angle (rotations about the y axis), so that only one angle was needed to define orientations. Another consequence of the azimuthal symmetry is that the results for prolate and oblate spheroids were the same, provided that the major and minor axes were each equal (the situation shown in Figure 1.3). The quadruple integral was evaluated using a Monte Carlo method similar to that just described, with $\sin\theta$ as a weighting factor in the integration over θ. When applied to spheres, the Monte Carlo algorithm gave results that were in excellent agreement with equations A.4 and A.5.

Appendix B. SIMPLIFICATION FOR SMALL POTENTIALS AND ANALYTICAL EVALUTAITON OF ELECTROSTATIC POTENTIAL ENERGIES

Simplification for small potentials

If the pore radius, pore surface charge density, and Debye length are such that the equilibrium double layer potential is small, certain simplifications can be made. If $|\Psi| \ll 1$, then $\sinh\Psi \cong \Psi$ and equation (3.8) becomes

$$\frac{1}{\beta}\frac{d}{d\beta}\left(\beta\frac{d\Psi}{d\beta}\right) = \tau^2\Psi \tag{B.1}$$

which is a modified Bessel equation. The solution that satisfies equations (3.10) and (3.11) is

$$\Psi(\beta) = \frac{q_c}{\tau}\frac{\mathrm{I}_0(\tau\beta)}{\mathrm{I}_1(\tau)} \quad . \tag{B.2}$$

Thus, equation (B.2) may be used in place of the numerical solution of Eq. (9), provided that $|\Psi| \ll 1$. In addition, the integral in the streaming potential contribution to the fluid velocity [equations. (3.17) and (3.18)] may be evaluated analytically:

$$\int_\beta^1 \frac{dy}{y}\int_0^y \sinh\Psi\, x\, dx \cong \int_\beta^1 \frac{dy}{y}\int_0^y \Psi\, x\, dx = \frac{q_c}{\tau^3}\frac{\mathrm{I}_0(\tau) - \mathrm{I}_0(\tau\beta)}{\mathrm{I}_1(\tau)} \quad . \tag{B.3}$$

Aside from being able to make the substitutions $\sinh\Psi = \Psi$ and $\cosh\Psi = 1$ in equation (3.22), there was no particular simplification in evaluating the streaming potential. Computing Λ, local values of v_z, and σ_o each still required numerical integration. Accordingly, the code written to evaluate σ_o did not use the approximations embodied in equations (B.1)-(B.3). If macromolecules are absent ($f = 0$ in the velocity expressions), the linearization for small potentials permits the analytical evaluation of Λ and $v_z(\beta)$

(Newman 1973). This was helpful for checking those parts of our code, but did not simplify the calculation of σ_o.

Analytical evaluation of electrostatic potential energies

A major computational saving was achieved by using previous analytical results for the particle potential energy, $E(\beta)$. Those results were based on eigenfunction solutions of the linearized Poisson-Boltzmann equation for the three-dimensional geometry corresponding to a sphere positioned eccentrically within a cylindrical pore (Smith and Deen 1983). As discussed in connection with Fig. 1, accurate values of the Boltzmann factor were obtained in that manner even if $|\Psi|$ was not small. As shown previously (Smith and Deen 1983), when the surface charge densities are constant, E is a quadratic function of the charge densities. Thus,

$$\frac{E}{\xi kT} = \alpha_s q_s^{\,2} + \alpha_{sc} q_s q_c + \alpha_c q_c^{\,2} \tag{B.4}$$

where the coefficients α_s, α_{sc}, and α_c each depend on β, λ, and τ but are independent of q_s and q_c. The energy scale factor ξ is that defined in equation (3.32). To good approximation, the coefficients may be calculated as

$$\alpha_s = \frac{8\pi\tau\lambda^4 e^{\tau\lambda}}{(1+\tau\lambda)^2}\frac{\Omega(\tau,\beta)}{\delta(\tau,\lambda)} \tag{B.5}$$

$$\alpha_{sc} = \frac{4\pi^2\lambda^2 I_0(\tau\beta)}{(1+\tau\lambda)I_1(\tau)\delta(\tau,\lambda)} \tag{B.6}$$

$$\alpha_c = \left[\frac{\pi I_0(\tau\beta)}{\tau I_1(\tau)}\right]^2 \frac{(e^{\tau\lambda}-e^{-\tau\lambda})\tau\lambda L(\tau\lambda)}{(1+\tau\lambda)\delta(\tau,\lambda)} \tag{B.7}$$

The functions δ, L, and Ω are defined as

$$\delta(\tau,\lambda) = \pi\tau e^{-\tau\lambda} - \frac{2(e^{\tau\lambda} - e^{-\tau\lambda})\tau\lambda L(\tau\lambda)\Omega(\tau,\beta)}{1+\tau\lambda}. \tag{B.8}$$

$$L(\tau\lambda) = \coth(\tau\lambda) - \frac{1}{\tau\lambda} \tag{B.9}$$

$$\Omega(\tau,\beta) = \frac{I_0(\tau\beta)}{2}\sum_{t=0}^{\infty}\frac{\beta^t}{2^t t!}\frac{I_t(\tau\beta)}{\tau^t}\int_{\varsigma=0}^{\infty}\varsigma^{2t}\left[\frac{K_1\left(\left[\tau^2+\varsigma^2\right]^{1/2}\right)}{I_1\left(\left[\tau^2+\varsigma^2\right]^{1/2}\right)}\right]d\varsigma \tag{B.10}$$

where I_n and K_n are modified Bessel functions of the first and second kinds, respectively, of order n. Truncating the series in equation (B.10) after 20 terms is usually sufficient for 1% accuracy. This expression, which is from equation (2.121) in Smith, can be simplified further if the Debye length is relatively small (Smith 1981). If $\tau \geq 3$, Ω is well-represented by equation (3.29) in Smith and Deen (Smith and Deen 1983).

Appendix C. PHILLIPS ALGORITHM

For a series of solids interacting with each other electrostatically, the method entails distributing a set of singularities, or point charges, in these solids according to a predefined algorithm. The electrostatic potential in the liquid phase is then written as a sum of the contributions from the point charges located in the solid phase. Mathematically, the contribution from a single point charge is given by the fundamental solution to the linearized Poisson Boltzmann equation or the green function given as,

$$\psi = q\frac{e^{-\tau\beta}}{\beta} \tag{C.1}$$

where q, is the unknown charge density of that specific point charge. Also are distributed points on the surface of each solid, according to a predefined algorithm. The potential or charge density is then calculated at each of these surface points in terms of the unknown charge densities, the predicted surface conditions. Since the governing equation is linear, one is guaranteed that the sum of the solutions is itself a solution. The unknown point charges are then determined by obtaining the best possible fit between the predicted values of the surface conditions and the actual boundary conditions (potential or charge).

The unit cell in our problem comprised of a central fiber and six surrounding fibers and a sphere in the vicinity of the central fiber. For the spherical macromolecule the singularities are located in two layers, with fourteen singularities per layer. Six of the singularities are a distance 0.5α from the sphere center (i.e half way between the center and the sphere surface) and fall on the coordinate axes. The other eight are also 0.5α form the sphere center and fall in the center of each of the eight quadrants defined by the coordinate axes. The second layer is identical to the first, except for the fact that the singularities are distributed at a distance of 0.25α from the sphere center. This

configuration of singularities is used with 1986 surface points per sphere located at regular intervals of $\pi/32$ radians in the theta and the phi directions. For each of the cylindrical fibers, the singularities were placed in circular "rings", with six singularities per ring. In half of the rings, the singularities are a distance of 0.5β from the cylinder axes (i.e half the distance from the axes to the cylinder surface), and in the other half they are a distance $0.25\ \beta$. The rings were separated by an axial distance of 4/10 of a Debye length and extend over an axial distance of 10 Debye lengths or 5 Debye lengths on either side of the point of closes approach of the sphere (Phillps 1995). Using this set up, for each of the surface points we have the equation

$$\psi_{bdry}(\vec{r}) = \sum_{i=1}^{n} \psi_{cyl}(\vec{r}) + \psi_{c,sph}(\vec{r}) + \sum_{i=1}^{nN_c} \psi_{oc,cyl}(\vec{r}) + \sum_{i=1}^{N_s} \psi_{oc,sph}(\vec{r}) \tag{C.2}$$

Here the subscript "bdry", denotes the boundary point, N_s and N_c denote the singularities in the sphere and the cylinder respectively, n denotes the number of cylinders, seven in this case and ψ_{cyl} denotes the Bessel function solution for the electrostatic potential around an isolated cylindrical rod.

Thus this results in an over determined linear system of the form

$$\begin{aligned} &AX=B \\ &A=N_{bdry}\ X\ (nN_c+N_s) \\ &X=(nN_c+N_s)\ X\ 1 \\ &B=(nN_c+N_s)\ X\ 1 \end{aligned} \tag{C.3}$$

Here X is the unknown matrix of singularity strengths, A and B are known matrices. For our case the total number of boundary points using 7 fibers was 13186 and the total number of singularities was 1078. The condition number of the matrix A was found to be pretty high ($O\sim10^8$). Therefore, in order to solve the system the matrix A was QR

decomposed (qr in Matlab) and then inverted. This step preserves the accuracy of the resulting solution despite the high condition number. Also it was found that the interaction energy of the sphere-fiber system was wholly determined by the inner layer of the seven fiber system, the outer layer contributing minimally to the interaction energy.

As pointed out above, the ability of the method to satisfy the constant charge density boundary conditions turned out to be very sensitive to the placement of the internal singularities and the selection of surface points. In practical for the two sphere case, the differences between the analytical and the numerical Boltzmann factors increases as the objects are rotated with respect to each other as shown in Figure C.1. Here θ denotes the relative angle between the two spheres. As seen in the plot, the difference between the analytical and the numerical values increases as θ increases. This shows that the method is suited for two-object geometries wherein the objects are placed symmetrically across each other. In our application of interest the objects are placed at angular orientations with respect to each other making the method unapplicable.

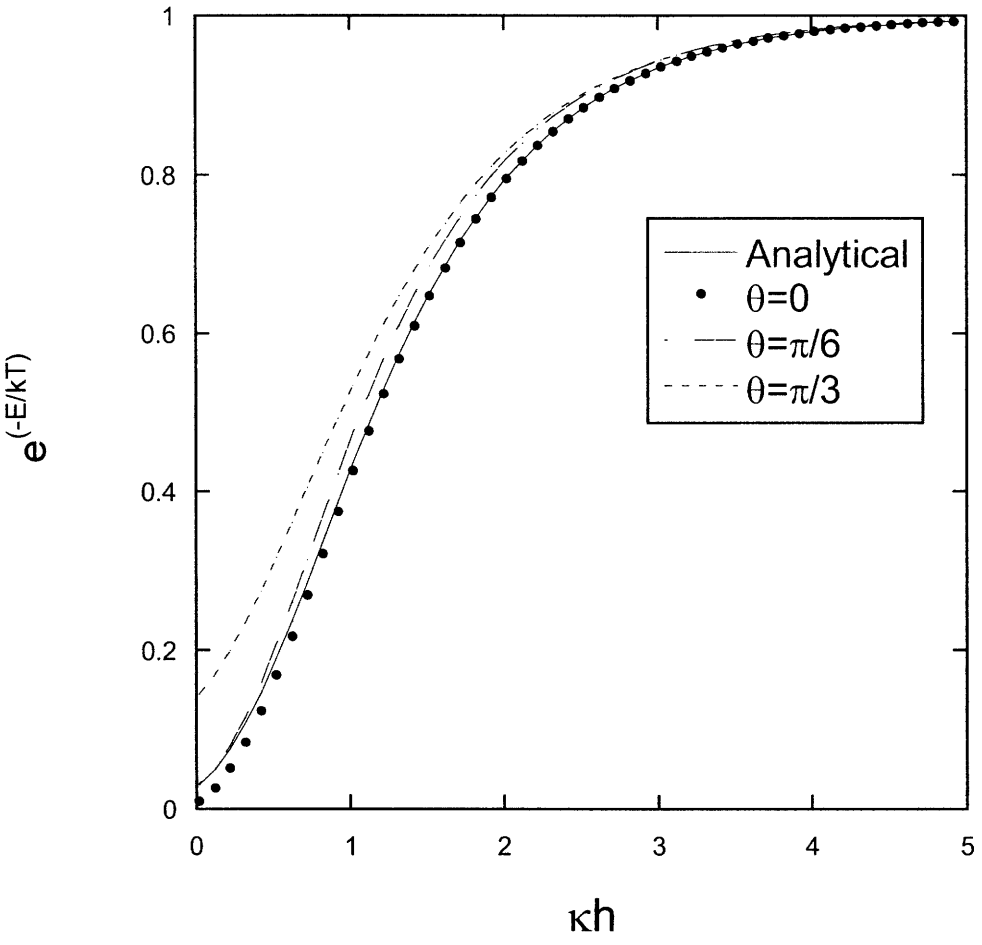

Figure C.1 Boltzmann factors for two spheres each of radius 20nm and each at a unit dimensionless charge density (made dimensionless using the same scheme as in Chapter 3) placed in vicinity of each other. h denotes the dimensional distance, κ is the Debye length set equal to 20nm.

Appendix D. TESTS FOR PAIRWISE ADDITIVITY AND IMPROVED CORRELATIONS

Table D.1 Pairwise additivity tests for the perpendicular arrangement.

τ	q_s	q_c	α	η	η_1	$e^{(-E/kT)}$ (COMSOL)	$e^{(-E/kT)}$ (COMSOL Pair Wise)
2.00000	2.00000	2.00000	0.75000	3.00000	0.60000	0.17850	0.18050
2.00000	2.00000	2.00000	0.75000	3.00000	1.20000	0.44920	0.45550
2.00000	2.00000	2.00000	0.75000	3.00000	1.80000	0.67120	0.68230
2.00000	2.00000	2.00000	0.75000	3.00000	2.40000	0.82160	0.82910
2.00000	2.00000	2.00000	0.75000	3.00000	3.00000	0.90540	0.91730
2.00000	2.00000	2.00000	0.75000	3.00000	3.60000	0.95660	0.97060
2.00000	2.00000	2.00000	0.75000	1.50000	0.60000	0.17720	0.17930
2.00000	2.00000	2.00000	0.75000	1.50000	1.20000	0.44610	0.45440
2.00000	2.00000	2.00000	0.75000	1.50000	1.80000	0.67150	0.67850
2.00000	2.00000	2.00000	0.75000	1.50000	2.40000	0.81780	0.82730
2.00000	2.00000	2.00000	0.75000	1.50000	3.00000	0.90870	0.91170
2.00000	2.00000	2.00000	0.75000	1.50000	3.60000	0.95180	0.96760
2.00000	2.00000	2.00000	0.75000	1.00000	0.60000	0.17510	0.17880
2.00000	2.00000	2.00000	0.75000	1.00000	1.20000	0.44350	0.45060
2.00000	2.00000	2.00000	0.75000	1.00000	1.80000	0.66820	0.67660
2.00000	2.00000	2.00000	0.75000	1.00000	2.40000	0.81730	0.82490
2.00000	2.00000	2.00000	0.75000	1.00000	3.00000	0.91460	0.91230
2.00000	2.00000	2.00000	0.75000	1.00000	3.60000	0.95420	0.96630
2.00000	2.00000	2.00000	0.75000	0.50000	0.60000	0.17510	0.17880
2.00000	2.00000	2.00000	0.75000	0.50000	1.20000	0.44350	0.45060
2.00000	2.00000	2.00000	0.75000	0.50000	1.80000	0.66820	0.67660
2.00000	2.00000	2.00000	0.75000	0.50000	2.40000	0.81730	0.82490
2.00000	2.00000	2.00000	0.75000	0.50000	3.00000	0.91460	0.91230
2.00000	2.00000	2.00000	0.75000	0.50000	3.60000	0.95420	0.96630
0.50000	1.00000	1.00000	0.90000	1.00000	1.20000	0.01800	0.02050
0.50000	1.00000	1.00000	0.90000	1.00000	1.80000	0.12830	0.13740
0.50000	1.00000	1.00000	0.90000	1.00000	2.40000	0.33430	0.35340
0.50000	1.00000	1.00000	0.90000	1.00000	3.60000	0.76470	0.74290
0.50000	1.00000	1.00000	0.90000	1.00000	4.80000	0.90670	0.88630
0.50000	1.00000	1.00000	0.90000	1.00000	5.40000	0.96100	0.90780
0.75000	1.00000	1.00000	0.90000	1.00000	1.20000	0.06290	0.06970
0.75000	1.00000	1.00000	0.90000	1.00000	1.80000	0.24140	0.25390
0.75000	1.00000	1.00000	0.90000	1.00000	2.40000	0.47690	0.48790
0.75000	1.00000	1.00000	0.90000	1.00000	3.60000	0.81440	0.82370
0.75000	1.00000	1.00000	0.90000	1.00000	4.80000	0.94840	0.95500
0.75000	1.00000	1.00000	0.90000	1.00000	5.40000	0.97250	0.97750
1.00000	1.00000	1.00000	0.90000	1.00000	1.20000	0.13430	0.14510
1.00000	1.00000	1.00000	0.90000	1.00000	1.80000	0.35610	0.37190
1.00000	1.00000	1.00000	0.90000	1.00000	2.40000	0.58310	0.59270

1.00000	1.00000	1.00000	0.90000	1.00000	3.60000	0.86060	0.86680
1.00000	1.00000	1.00000	0.90000	1.00000	4.80000	0.95720	0.96260
1.00000	1.00000	1.00000	0.90000	1.00000	5.40000	0.97810	0.98120
0.50000	1.00000	1.00000	0.40000	1.00000	1.20000	0.37700	0.39160
0.50000	1.00000	1.00000	0.40000	1.00000	1.80000	0.61090	0.62500
0.50000	1.00000	1.00000	0.40000	1.00000	2.40000	0.77650	0.79040
0.50000	1.00000	1.00000	0.40000	1.00000	3.00000	0.88010	0.88850
0.50000	1.00000	1.00000	0.20000	1.00000	0.60000	0.58110	0.58750
0.50000	1.00000	1.00000	0.20000	1.00000	1.20000	0.76380	0.77120
0.50000	1.00000	1.00000	0.20000	1.00000	1.80000	0.87090	0.87600
0.50000	1.00000	1.00000	0.20000	1.00000	2.40000	0.93130	0.93460
0.50000	1.00000	1.00000	0.20000	1.00000	3.00000	0.96520	0.96500
0.50000	1.00000	1.00000	0.50000	1.00000	0.60000	0.05230	0.05870
0.50000	1.00000	1.00000	0.50000	1.00000	1.20000	0.23480	0.23980
0.50000	1.00000	1.00000	0.50000	1.00000	1.80000	0.47590	0.48560
0.50000	1.00000	1.00000	0.50000	1.00000	2.40000	0.68430	0.69500
0.50000	1.00000	1.00000	0.50000	1.00000	3.00000	0.82680	0.83350
0.50000	1.00000	1.00000	0.10000	1.00000	0.60000	0.86550	0.87060
0.50000	1.00000	1.00000	0.10000	1.00000	1.20000	0.93020	0.93460
0.50000	1.00000	1.00000	0.10000	1.00000	1.80000	0.96140	0.96610
0.50000	1.00000	1.00000	0.10000	1.00000	2.40000	0.98030	0.98300
0.50000	1.00000	1.00000	0.10000	1.00000	3.00000	0.99030	0.99180

Table D.2 Pairwise additivity tests for the collinear arrangement.

η_1 is the surface – to – surface separation between the sphere and either fiber.

τ	q_s	q_c	α	η_1	$e^{(-E/kT)}$ (COMSOL)	$e^{(-E/kT)}$ (COMSOL Pair Wise)
4.00000	1.00000	1.00000	0.70000	0.60000	0.44830	0.45150
4.00000	1.00000	1.00000	0.70000	1.20000	0.68700	0.69030
4.00000	1.00000	1.00000	0.70000	1.80000	0.82840	0.83220
4.00000	1.00000	1.00000	0.70000	2.40000	0.90710	0.91290
4.00000	1.00000	1.00000	0.70000	3.00000	0.95010	0.95640
4.00000	1.00000	1.00000	0.70000	3.60000	0.97210	0.97900
2.00000	1.00000	1.00000	0.50000	0.60000	0.25420	0.26680
2.00000	1.00000	1.00000	0.50000	1.20000	0.51430	0.53520
2.00000	1.00000	1.00000	0.50000	1.80000	0.70610	0.73380
2.00000	1.00000	1.00000	0.50000	2.40000	0.82610	0.85660
2.00000	1.00000	1.00000	0.50000	3.00000	0.89410	0.92580
2.00000	1.00000	1.00000	0.50000	3.60000	0.93140	0.96290
1.00000	1.00000	1.00000	0.50000	0.60000	0.05080	0.06730
1.00000	1.00000	1.00000	0.50000	1.20000	0.22370	0.28600
1.00000	1.00000	1.00000	0.50000	1.80000	0.43930	0.54340
1.00000	1.00000	1.00000	0.50000	2.40000	0.62410	0.73900
1.00000	1.00000	1.00000	0.50000	3.00000	0.74950	0.89230
1.00000	1.00000	1.00000	0.50000	3.60000	0.80220	0.97560
0.50000	1.00000	1.00000	0.50000	0.60000	0.00244	0.01230
0.50000	1.00000	1.00000	0.50000	1.20000	0.03846	0.13020
0.50000	1.00000	1.00000	0.50000	1.80000	0.12573	0.39392
0.50000	1.00000	1.00000	0.50000	2.40000	0.22945	0.65224
0.50000	1.00000	1.00000	0.50000	3.00000	0.33455	0.84283

Table D.3 Pairwise additivity tests for the isoceles arrangement.

τ	q_s	q_c	α	η	η_1	$e^{(-E/kT)}$ (COMSOL)	$e^{(-E/kT)}$ (COMSOL Pair Wise)
1.00000	1.00000	1.00000	0.5000	2.40000	1.20000	0.30930	0.39130
1.00000	1.00000	1.00000	0.5000	4.80000	2.40000	0.71090	0.86630
1.00000	1.00000	1.00000	0.5000	7.20000	3.60000	0.81830	0.98060
1.00000	1.00000	1.00000	0.5000	9.60000	4.80000	0.84360	0.99970
2.00000	1.00000	1.00000	0.5000	2.40000	1.20000	0.57330	0.59600
2.00000	1.00000	1.00000	0.5000	4.80000	2.40000	0.95660	0.97060
2.00000	1.00000	1.00000	0.5000	7.20000	3.60000	0.88020	0.91130
2.00000	1.00000	1.00000	0.5000	9.60000	4.80000	0.95210	0.98340
4.00000	1.00000	1.00000	0.5000	2.40000	1.20000	0.96750	0.99750
4.00000	1.00000	1.00000	0.5000	4.80000	2.40000	0.79480	0.79830
4.00000	1.00000	1.00000	0.5000	7.20000	3.60000	0.95870	0.95170
4.00000	1.00000	1.00000	0.5000	9.60000	4.80000	0.98550	0.99760
2.00000	1.00000	1.00000	1.0000	2.40000	1.20000	0.99310	0.99880
2.00000	1.00000	1.00000	1.0000	4.80000	2.40000	0.25870	0.26710
2.00000	1.00000	1.00000	1.0000	7.20000	3.60000	0.75520	0.78070
2.00000	1.00000	1.00000	1.0000	9.60000	4.80000	0.92730	0.94360
4.00000	1.00000	1.00000	1.0000	2.40000	1.20000	0.59780	0.59730
4.00000	1.00000	1.00000	1.0000	4.80000	2.40000	0.88870	0.88630
4.00000	1.00000	1.00000	1.0000	7.20000	3.60000	0.96720	0.95740
4.00000	1.00000	1.00000	1.0000	9.60000	4.80000	0.98530	0.98290

Table D.4 Data set used in fitting new sphere-fiber energy correlation

$E/\xi kT$	τ	η	α	Q_s	Q_f
0.971	0.500	0.100	0.200	1	1
0.205	0.500	0.300	0.200	1	1
0.044	0.500	0.500	0.200	1	1
0.501	1.333	0.100	0.200	1	1
0.120	1.333	0.300	0.200	1	1
0.031	1.333	0.500	0.200	1	1
0.322	2.167	0.100	0.200	1	1
0.076	2.167	0.300	0.200	1	1
0.018	2.167	0.500	0.200	1	1
0.233	3.000	0.100	0.200	1	1
0.057	3.000	0.300	0.200	1	1
0.014	3.000	0.500	0.200	1	1
1.741	0.500	0.100	0.400	1	1
0.375	0.500	0.300	0.400	1	1
0.087	0.500	0.500	0.400	1	1
1.235	0.833	0.100	0.400	1	1

0.277	0.833	0.300	0.400	1	1
0.070	0.833	0.500	0.400	1	1
0.934	1.167	0.100	0.400	1	1
0.216	1.167	0.300	0.400	1	1
0.053	1.167	0.500	0.400	1	1
0.738	1.500	0.100	0.400	1	1
0.173	1.500	0.300	0.400	1	1
0.044	1.500	0.500	0.400	1	1
2.379	0.500	0.100	0.600	1	1
0.521	0.500	0.300	0.600	1	1
0.117	0.500	0.500	0.600	1	1
1.940	0.667	0.100	0.600	1	1
0.433	0.667	0.300	0.600	1	1
0.101	0.667	0.500	0.600	1	1
1.621	0.833	0.100	0.600	1	1
0.367	0.833	0.300	0.600	1	1
0.090	0.833	0.500	0.600	1	1
1.375	1.000	0.100	0.600	1	1
0.316	1.000	0.300	0.600	1	1
0.078	1.000	0.500	0.600	1	1
2.890	0.500	0.100	0.800	1	1
0.633	0.500	0.300	0.800	1	1
0.166	0.500	0.500	0.800	1	1
2.574	0.583	0.100	0.800	1	1
0.575	0.583	0.300	0.800	1	1
0.139	0.583	0.500	0.800	1	1
2.317	0.667	0.100	0.800	1	1
0.519	0.667	0.300	0.800	1	1
0.130	0.667	0.500	0.800	1	1
2.090	0.750	0.100	0.800	1	1
0.474	0.750	0.300	0.800	1	1
0.120	0.750	0.500	0.800	1	1
0.125	1.000	0.050	0.500	0	1
0.056	1.000	0.100	0.500	0	1
0.170	1.000	0.050	0.700	0	1
0.076	1.000	0.100	0.700	0	1
0.105	1.000	0.050	0.700	1	0
0.043	1.000	0.100	0.700	1	0
0.065	1.000	0.050	0.500	1	0
0.022	1.000	0.100	0.500	1	0
0.188	0.500	0.050	0.700	0	1
0.076	0.500	0.100	0.700	0	1
0.124	0.500	0.050	0.500	0	1
0.048	0.500	0.100	0.500	0	1
0.115	0.500	0.050	0.700	1	0
0.058	0.500	0.100	0.700	1	0

BIBLIOGRAPHY

Anderson J.L., D.M. Malone, Mechanism of osmotic flow in porous membranes, *Biophys. J.* 14, 957-982 (1974).

Anderson J.L., R.P. Adamski, Solute concentration effects of the osmotic reflection coefficient, *Biophys. J.* 44, 79-90 (1983).

Anderson J.L., Configurational effects of the reflection coefficient for rigid solutes in capillary pores, *J. theor. Biol.* 90, 405-426 (1981).

Anderson J.L., J. A. Quinn, Restricted transport in small pores. A model for steric exclusion and hindered particle motion, *Biophys. J.* 14, 130-150 (1974).

Brenner H., Rheology of a dilute suspension of axisymmetric Brownian particles, *Int. J. Multiphase Flow* 1, 195-341 (1974).

Brinkman H.C, A calculation of the viscous force exerted by a flowing fluid on a dense swarm of particles, *Appl. Sci. Res.* A1, 27-34 (1947).

Bean C.P., The physics of porous membranes-neutral pores, *Membranes* vol.1, 1-54 (1972).

Bhalla G. and W.M. Deen, Effects of molecular shape on osmotic reflection coefficients, *J. Memb. Sci.* 306 , 116-124 (2007) .

Bhalla G. and W.M. Deen, Effects of charge on osmotic reflection coefficients of macromolecules in porous membranes, *J. Colloid Interface Sci.* 333, 363-372 (2009).

Bhalla G. and W.M. Deen, Effects of charge on osmotic reflection coefficients of macromolecules in fibrous membranes, (2009).

Curry F.E., A hydrodynamic description of the osmotic reflection coefficient with application to the pore theory of transcapillary exchange, *Microvasc. Res.* 8, 236-252 (1974).

Curry F.E., C.C. Michel, A fiber matrix model for capillary permeability, *Microvasc. Res.* 20, 96-99 (1980).

Curry F.E., Mechanics and thermodynamics of transcapillary exchange, In: *Handbook of Physiology, Section 2, The Cardiovascular System*, 309-374 (1984).

Dainty J., B.Z. Ginzburg, Irreversible thermodynamics and frictional models of membrane processes, with particular application to the cell membrane, *J. theor. Biol.* 5, 256-265 (1963).

Dechadilok P. and W. M. Deen, Hindrance factors for diffusion and convection in pores, *Ind. Eng. Chem.* Res. 45, 6953-6959 (2006).

Deen W.M., Hindered transport of large molecules in liquid-filled pores, *AIChE J.* 33, 1409-1425 (1987).

Smith F.G. and W.M. Deen, Electrostatic double layer interactions for spherical colloids in cylindrical pores, *J. Colloid Interface Sci.*78, 444-465 (1980).

Smith F.G. and W.M. Deen, Electrostatic effects on the partitioning of spherical colloids between dilute bulk solutions and cylindrical pores, *J. Colloid Interface Sci.* 91, 571-589 (1983).

BIBLIOGRAPHY

Johnson E.M. and W.M. Deen, Electrostatic effects on the equilibrium partitioning of spherical colloids in random fibrous media, *J. Colloid Interface Sci.* 178, 749-756 (1996).

Durbin R.P., Osmotic flow of water across cellulose membranes, *J. Gen. Physiol.* 44, 315-326 (1960).

Ferry J.D., Statistical evaluation of sieve constants in ultrafiltration, *J. Gen. Physiol.* 20, 95-104 (1936).

Friedman M.H., R.A. Meyer, Transport across homoporous and heteroporous membranes in non-ideal, non-dilute solutions, *Biophys. J.* 34, 535-544 (1981).

Happel J., Viscous flow relative to arrays of cylinders, *AIChE J.* 5 174-177 (1959).

Happel J., H. Brenner, *Low Reynolds Number Hydrodynamics* Netherlands, (1973).

Haraldsson B., J. Nystrom, W.M. Deen., Properties of the Glomerular Barrier and Mechanisms of Proteinuria, *Physiol. Rev.* 88, 451-487 (2008) .

Hill A.E., Osmotic flow in membrane pores, *Int. Rev. of Cytology* 163,1-41 (1995).

Hill A.E., Osmosis in leaky pores: The role of pressure, *Proc. R. Soc. London Ser. B* 237, 363-367 (1989).

Katchalsky A., P.F. Curran, *Non-Equilibrium Thermodynamics in Biophysics, Harvard University Press*, Cambridge, Mass (1965).

Kedem O., A. Katchalsky, A physical interpretation of the phenomenological coefficients of membrane permeability, *J. Gen. Physiol.* 45, 143-179 (1961).

Kellen M., A model for microcirculatory fluid and solute exchange in the heart, *PhD Thesis*, University of Washington (1999).

Keijzer Th. J.S., P.J. Kleingeld, , J.P.G Loch, Chemical osmosis in compacted clayey material and the prediction of water transport, *Engineering Geol.* 53, 151-159 (1999).

Kobatake Y., Flows through charged membranes. I. Flip-Flop current vs. voltage relation, *J. Chem. Phys.* 40, 2212-2218 (1963).

Levitt D.G., General continuum analysis of transport through pores. I. Proof of Onsager's reciprocity postulate for uniform pore, *Biophys. J.* 15, 533-551 (1975).

Lightfoot E.N., J.B. Bassingthwaighte, E.F Grabowski, Hydrodynamic models for diffusion in microporous membranes, *Ann Biomed. Eng.* 4, 78-90 (1976).

Mauro A., Nature of solvent transfer in osmosis, *Science* 126, 252-253 (1957).

Marshall E.A., The osmotic flow of an electrolyte through a charged porous membrane, *J. theor. Biol.* 66, 107-135 (1977).

Martys N., D. P. Bentz, E.J. Garboczi, Computer simulation study of the effective viscosity in Brinkman's equation, *Phys. Fluids* 6, 1434-1439 (1993).

Mattern K.J., C. Nakornchai and W.M. Deen, Darcy permeability of agarose-glycosaminoglycan gels analyzed using fiber mixture and Donnan models, *Biophys. J.* 95, 648-656 (2008).

Michel C. C., Fluid movements through capillary walls, *Handbook of Physiology, Section 2, The Cardiovascular System*, 375-409 (1984).

BIBLIOGRAPHY

Newman J.S., *Electrochemical Systems*, Prentice-Hall, Inc., *Englewood Cliffs*, N.J. (*1973*).

Ogston A.G., The spaces in a uniform random suspension of fibers, *Trans. Faraday Soc.* 54, 1745-1757 (1958).

Ogston A.G., B.N. Preston, J. D. Wells, On the transport of compact particles through solutions of chain polymers, *Proc. R. Soc. London Ser. A* 333, 297-316 (1973).

Ogston A.G., C. C. Michel, General descriptions of passive transport of neutral solute and solvent through membranes, *Prog. Biophys. Mol. Biol.* 34, 197-217 (1978).

Onsager L., Reciprocal relations in irreversible processes, *Phys. Rev.* 38, 2255-2279 (1931).

Opong W.S., A.L. Zydney, Effect of membrane structure and protein concentration on the osmotic reflection coefficient, *J. Membrane Sci.* 72, 277-292 (1992).

Osterle J.F., J.C. Fair, Reverse electrodialysis in charged capillary membranes, *J. Chem. Phys.* 54, 3307-3316 (1970).

Patlak C.S., D.A. Goldstein, J.F Hoffman, The flow of solute and solvent across a two membrane system, *J. Theor. Biol.* 5, 426-442 (1963).

Pappenheimer J.R., E.M. Renkin, L.M. Borrero, Filtration, diffusion and molecular sieving through peripheral capillary membranes. A contribution to the pore theory of capillary permeability, *Am. J. Physiol* 167, 13-46 (1951).

Perl W., A friction coefficient, series-parallel channel model for transcapillary flux of nonelectrolytes and water, *Microvasc. Res.* 6, 169-193 (1973).

Phillips R.J., Calculation of multisphere linearized Poisson-Boltzmann interactions near cylindrical fibers and planar surfaces, *J. Colloid Interface Sci.* 175, 386-399 (1995).

Reed C.C., Mathematical concepts in the transport of interacting particles, *PhD Thesis*, Cornell University (1978).

Reiner E.S., C.J. *Radke,*, Electrostatic Interactions in Colloidal Suspensions: Tests of Pairwise Additivity, *AIChE J* 37(6), (1991) 805.

Renkin E.M., Filtration, diffusion and molecular sieving through porous cellulose membranes, *J. Gen. Physiol.* 38, 225-248 (1954).

Ruckenstein E., P. Neogi, Viscoelectric effects in reverse osmosis, *J. Colloid Interface Sci.* 79, 159-169 (1980).

Ruckenstein E., S. Varanasi, Electrolyte osmosis through capillaries, *J. Colloid Interface Sci.* 82, 439-457 (1981).

Schlogl R., The theory of anomalous osmosis, *Z. Phsik. Chem.* 3, 73-102 (1955).

Schultz J.S., R. Valentine, C.Y. Choi, Reflection coefficients of homopore membranes: Effect of molecular size and configuration, *J. Gen. Physiol.* 73, 49-60 (1979).

Sharp K.A., B. Honig, Calculating Total Electrostatic Energies with the Nonlinear Poisson-Boltzmann Equation, *J. Phys. Chem.* 94, 7684-7692 (1991).

BIBLIOGRAPHY

Spiegler K.S., Transport processes in ionic membranes, *Trans. Faraday Soc.* 54, 1408-1428 (1958).

Starling E.H., On the adsorbtion of fluid from interstitial spaces, *J Physiol. London* 19, 312-326 (1896).

Staverman A., The theory of measurement of osmotic pressure, *J. Rec. Trav. Chim.* 70, 344-352 (1951).

Tanford C., Physical Chemistry of Macromolecules, Wiley, New York, 1961.

Vargas F., J. A. Johnson, An estimate of reflection coefficients for rabbit heart capillaries, *J. Gen. Physiol.* 47, 667-677 (1964).

Verwey E. J. W., J. T. G. Overbeek, Theory of the stability of lyophobic colloids, *Elsevier, Amsterdam* (1948).

Vilker V.L., C.K. Colton, K.A. Smith, The osmotic-pressure of concentrated protein solutions - effect of concentration and pH in saline solutions of bovine serum albumin, *J. Colloid Interface Sci.* **79, 548-566**(1981) 548.

Yan Z.Y., S.Weinbaum and R. Pfeffer, On the fine structure of osmosis including three-dimensional pore entrance and exit behaviour, *J. Fluid Mech* 162, 415-438 (1986).

Zhang X., F.-R. Curry and S.Weinbaum, Mechanism of osmotic flow in a periodic fiber array, *Am. J. Physiol.* 290, H844-852 (2006).